3063199693

Theory and Applications of Ultracold Atoms in Optical Superlattices



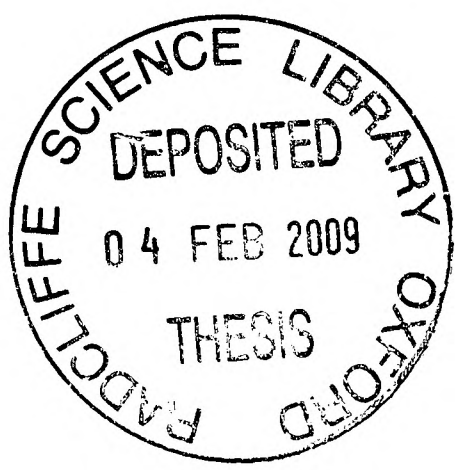
Benoît Vaucher

Merton College, Oxford

A thesis submitted to the Mathematical and Physical Sciences Division for the degree of Doctor of Philosophy in the University of Oxford

Trinity Term, 2008

Atomic and Laser Physics,
University of Oxford



To Jessica.

Theory and Applications of Ultracold Atoms in Optical Superlattices

Benoit Vaucher, Merton College, Oxford

Michaelmas Term 2008

Abstract

Optical lattices make it possible to trap and coherently control large ensembles of ultracold atoms. They provide the possibility to create lattice potentials that mimic the structure of solid-state systems, and to control these potentials dynamically. In this thesis, we study how dynamical manipulations of the lattice geometry can be used to perform different tasks, ranging from quantum information processing to the creation of diatomic molecules.

We first examine the dynamical properties of ultracold atoms trapped in a lattice whose periodicity is dynamically doubled. We derive a model describing the dynamics of the atoms during this process, and compute the different interaction parameters of this model. We investigate different ways of using this lattice manipulation to optimise the initialisation time of a Mott-insulating state with one atom per site, and provide a scaling law related to the interaction parameters of the system.

We go on to show that entangling operations between the spin of adjacent atoms are realisable with optical lattices forming arrays of double-well potentials. We study the creation of a lattice containing a spin-encoded Bell-pair in each double-well, and show that resilient, highly-entangled many-body states are realisable using lattice manipulations. We show that the creation of cluster-like states encoded on Bell-pairs can be achieved using these systems, and we provide measurement networks that allow the execution of quantum algorithms while maintaining intact the resilience

of the system.

Finally, we investigate the possibility to create a diatomic molecular state and simulate Fermi systems via the excitation to Rydberg levels of ground-state atoms trapped in optical lattices. We develop a method based on symbolical manipulations to compute the interaction parameters between highly-excited electrons, and evaluate them for different electronic configurations. We use these parameters to investigate the existence of diatomic molecular states with equilibrium distances comparable to typical lattice spacings. Considering the possibility to excite atoms trapped in an optical lattice to Rydberg levels such that the electronic cloud of neighbouring atoms overlap, we propose a model describing their interactions and compute its parameters. If such systems were realised, they would allow the simulation of Fermi systems at a temperature much below the Fermi temperature, thus enabling the observation of quantum phenomena hitherto inaccessible with current technology.

Acknowledgements

I would like use these lines to thank all the people who made this thesis possible.

First, I would like to thank Dieter Jaksch for giving me the opportunity to study in his group. Dieter is very generous of his time, and spent large amount of it discussing my projects and ideas, for which I am very grateful. His uncompromising approach to research and attention to details is inspiring, and has always prevented complacency. I wish him every success in the future.

It has been a great pleasure to work surrounded by so many brilliant people. I was very lucky to share office space with Martin Bruderer, Alexander Klein, Karl Surmacz and Stephen Clark. Their enthusiasm, and broad knowledge of physics has been a great source of motivation over the years, and created a very stimulating environment to work in. An extra mention goes to Stephen for his encyclopedic knowledge and endless patience answering my questions, from the very first to the very last day of my stay in the group. I also acknowledge very enjoyable and fruitful collaborations with Andreas Nunnenkamp and Simon Thwaite.

On a more personal note, I owe a lot of gratitude to Nicolas, Ben, Patrick, Artemis and Georgios for being such wonderful friends, and without whom this time in Oxford would have never been so enjoyable. Extra thanks go to Ben for his careful proof-reading of many of the chapters presented in this thesis. Also, I would like to thank all of those long-time friends who kept on visiting us over the years. I feel immensely gifted to know so extraordinary people.

I also would like to thank my parents for their infallible support. They always helped and encouraged me in everyone of my endeavours, something for which I am very grateful. I also have to thank my younger brother Gabriel, for being an impeccable uncle, and also for his quasi-artistic insouciance (or is it really?) and lust for life which I have always found strangely inspiring.

Finally, I am missing the words to express my gratitude to Jessica. We came together to live in England, and without her love and support, the completion of this work would have never been possible. Our beautiful daughter Lucie was born in Oxford, and ever since she has filled our lives with the most indescribable joy.

Contents

Abstract i

Acknowledgements iii

Table of Contents v

Chapter 1. Introduction 1

Chapter 2. The tools of the trade. 9

2.1 Bose-Einstein condensation 9

2.2 Interactions between atoms in a dilute gas 12

2.3 Optical lattices 16

2.3.1 The physics of dipole traps 16

2.3.2 Lattice geometries 20

2.4 Single particle in optical (super-)lattices 23

2.5 Wannier functions 26

2.5.1 Simple Wannier functions 27

2.5.2 Approximations of Wannier functions 29

2.5.3 Comment on the nearsightedness of particles evolving in a lattice 30

2.5.4 Generalised Wannier functions 31

2.5.5 Optimisation of Wannier functions 32

Chapter 3. *Publication:* **Fast initialisation of a high-fidelity quantum register** **39**

3.1 Introduction 40

3.2 Model 42

3.2.1 Single-particle Hamiltonian 44

3.2.2 Interaction Hamiltonian 47

3.2.3 Limiting cases 48

3.3 Time-scale for the preparation of the quantum register 49

3.3.1 Numerical results 49

3.3.2 Analytical results 59

3.4 Conclusion 64

3.A Definition and localisation properties of GWFs 66

3.B Parameters of the single-particle Hamiltonian 68

3.C Dynamical and ground state calculations using the TEBD algorithm 70

3.D The ramp s_{gap} 72

Chapter 4. *Publication:* **Robust entangled states and MBQC using optical superlattices** **73**

4.1 Introduction 74

4.2 Model 76

4.3 Creation of a Bell state on every lattice site 79

4.4 Implementation of an entangling gate 84

4.5 Creation and detection of a state with a tunable amount of entanglement 88

4.6 Creation of maximally entangled states 91

4.7 Creation of a resource for MBQC 94

4.8 Summary 100
4.A The full Hamiltonian 101
4.B Measurement-based quantum computations and MPSs 104
4.B.1 General idea 104
4.B.2 Graphical notation 105
4.B.3 Read-out scheme 106

Chapter 5. Long-range molecular potentials **109**
5.1 Introduction 109
5.2 General framework 112
5.3 The ion-molecule 112
5.4 Homonuclear diatomic molecules 114
5.4.1 The molecular-orbital method 115
5.4.2 Valence bond approach 116
5.5 Long-range interactions 118
5.6 Long-range molecular potentials 121
5.7 Below the LeRoy radius? 123

Chapter 6. *Publication:* **Ultra-large Rydberg dimers in optical lattices 125**
6.1 Introduction 126
6.2 Molecular potentials of ultra-large Rydberg dimers 129
6.2.1 Model 129
6.2.2 Results 134
6.3 Interactions between highly excited electrons in a lattice 141
6.3.1 Model 142
6.4 Conclusion 145
6.A Replacement rules for the evaluation of two-centre molecular integrals with $m = 0$. 147

Chapter 7. Conclusion 151

Bibliography 155

Chapter 1

Introduction

The first experiments involving atoms trapped in optical lattices were conducted in 1993 by Grynberg *et al.*, followed by Hemmerich *et al.* at temperatures in the micro-kelvin range [1, 2]. The realisation of Bose-Einstein condensates in 1995 allowed experimentalists to dramatically lower the temperatures of these systems, which led to a series of groundbreaking experiments that continues to this date.

It was first discovered by Jaksch *et al.* that the motion of ultracold atoms in optical lattices is described by a Bose-Hubbard model, and that the interaction parameters of this model can be engineered by adjusting the parameters of the lasers used to create the lattice potential [3]. The experimental confirmation of these findings was realised by Greiner *et al.* in a seminal experiment, where a phase transition between the superfluid and Mott-insulating regimes—predicted by M. A. Fisher for systems described by the Bose-Hubbard model—was observed [4, 5]. Shortly after this first experiment, Greiner *et al.* also demonstrated the coherent nature of the dynamics of atoms trapped in such a setup [6]. Combined with measurement techniques (mainly via the measurement of the atomic cloud after ballistic expansion) that allow the state of the system to be probed, optical lattices loaded with ultracold atoms offer the very unique possibility to engineer, manipulate and observe the

many-body state of strongly interacting ensembles of atoms in an almost fully customisable lattice structure with low decoherence, a situation that atomic physicists could only dream of a couple of years ago.

The most remarkable feature of ultracold atoms trapped in optical lattices is their very long lifetime compared to the timescale of lattice manipulations. This characteristic renders these setups particularly attractive in the context of quantum information processing. Notably, Mott-insulating states where each site of the lattice is occupied by a fixed number of particles constitute a perfect quantum register, where information can be encoded on the long-lived, well-localised atoms (see e.g. Ref. [7]). A scheme aimed at accelerating the initialisation of such registers will be the subject of Chap. 3.

An obstacle towards the use of optical lattice setups to process quantum information is created by the difficulty in manipulating and moving atoms individually. This impairs the implementation of quantum computations via the circuit model, a model being based on the application of sequences of unitary operation on or between the qubits of a register, regardless of their relative location. Many different schemes have been proposed to circumvent this problem by using e.g. marker atoms, combining focused laser beams with microwave radiation to apply local operations, or by using auxiliary 1D lattices acting as quantum buses between registers [8–10]. However, optical lattice setups largely compensate this shortcoming by offering the possibility to perform (massively) parallel operations via global lattice manipulations. This enables the creation of easily scalable resource states which are useful for the implementation of quantum algorithms using the measurement-based quantum computation (MBQC) scheme [11–13]. In this scheme, computations are performed through a sequence of adaptive measurements on a highly-entangled initial resource state. The measurements are used to both imprint the input of the calculation on the resource state, and process it using a teleportation-inspired technique [14]. The

ability to produce resource states for MBQC using cold atoms trapped in an optical lattice was demonstrated in an experiment by Mandel *et al.*, where a spin-dependent lattice was exploited to perform controlled collisions between neighbouring atoms that resulted in the creation of a highly-entangled one-dimensional state reminiscent of a cluster state [15, 16]. Although systems of ultracold atoms trapped in optical lattices are very good candidates for the implementation of measurement-based quantum computers, the realisation of the latter requires two crucial conditions, that are only partially met in optical lattice setups. First, the ability to perform highly-efficient single-site measurements. Second, the possibility to isolate the system from external sources of noise that may affect the coherence of the resource state. We will address this issue in Chap. 4, where we study the creation resource state and provide measurement networks that reduce the sensitivity of the system to certain types of external noise during the computation process.

In recent years, systems of ultracold atoms trapped in optical lattices have found applications in the context of the creation and manipulation of ultracold molecules. Even simple diatomic molecules are difficult to cool—the lowest temperatures attained using direct methods are of the order of 1 μK—and so it is often more advantageous to form molecules from the already ultracold atoms present in a BEC [17]. Molecules have a rich energy structure as a result of their vibrational and rotational degrees of freedom; they can interact more strongly than atoms at large distances, and they are generally very sensitive to their electromagnetic environment. Hence, ultracold molecules lend themselves particularly well to applications such as interferometry, precision measurements, the coherent control of molecule formation using electromagnetic fields, or even quantum computation (see e.g. Refs. [18–20]). Optical lattices constitute a tool of choice for enhancing the formation rate of diatomic molecules in ultracold quantum gases, as they allow pairs of atoms to be isolated and shielded from the detrimental collisions that usually occur in a gas. So far, the

main approach towards the creation of such molecules has consisted of initialising an optical lattice in a Mott-insulating state with two fermionic atoms per site, and turning these two atoms into a bosonic diatomic molecule using either Feshbach resonances, or photo-association (see e.g. Refs. [21, 22]). The resulting molecules have a lifetime of the order of a few tens of ms, a binding energy of the order of $\sim 30\,\mathrm{kHz}$ and they remain trapped in the lattice potential [23]. These techniques have been applied e.g. to the measurement of the lattice occupancy, and thermometry [24]. Another class of ultracold diatomic molecules, whose existence has only recently been predicted, are made out of atoms excited to Rydberg levels. The most famous of this new family of ultracold molecules, the trilobite molecule, is composed of a highly-excited atom and a ground-state atom that acts as a perturber. It possesses a large permanent dipole moment that could potentially facilitate its manipulation in applications, and very large spatial dimensions—of the order of a few thousands of Bohr radii [25, 26]. Another example of such molecules is formed from two distant Rydberg atoms that interact via dipole-dipole interactions [27]. The spatial dimensions of these molecules are even larger, of the order of 10^4 Bohr radii, and their exaggerated properties could be potentially useful for applications such as the high-precision measurement of weak electromagnetic fields, or vacuum fluctuations. However, their very weak binding energy makes them experimentally difficult to produce and observe in a gas. Although the use of an optical lattice to fix the distances between the atoms and isolate them from collisions would be desirable in this context, it is difficult since the equilibrium distance of such molecules is much larger than the typical lattice spacings. Overcoming this difficulty constitutes the motivation of the research presented in Chap. 6, where we propose a setup that allows the creation of ultra-large molecules composed of Rydberg atoms with overlapping charge distributions. These molecules have an equilibrium distance comparable to the typical lattice spacing, and comparatively greater binding energies.

By exploiting e.g. Feshbach resonances, spin-dependent lattice potentials or Raman transitions, it was shown that the dynamics of ultracold atoms trapped in optical lattices could be used to simulate a wide range of translationally-invariant Hamiltonians. Notably, theoretical proposals have shown that systems governed by Hamiltonians used to describe e.g. high-T_c superconductivity, spin-spin interactions, or the fractional Hall effect can be realised using ultracold atoms trapped in optical lattices (see e.g. Refs. [28–30]). Rotating optical lattices even make it possible to simulate the effect of strong magnetic fields in a regime that is inaccessible in condensed-matter systems [31]. However, on the experimental side, the application of optical lattices for the quantum simulation of e.g. superconducting phases at high-temperature, is very challenging, due to the difficulty in cooling fermionic atoms below the Fermi temperature, which prevents the observation of such effects [32]. In the second part of Chap. 6, we will use some of the tools developed in the context of the evaluation of molecular potentials to compute the parameters of a Hubbard model describing the interactions between Rydberg atoms excited from ground-state atoms trapped in optical lattices. We will argue that these systems, if they were realised, would offer the possibility to observe exotic metallic phases or superconductivity at temperatures potentially much lower than the Fermi temperature.

Thesis overview

In this thesis, we will present three schemes that aim to overcome some of the shortcomings of optical lattices for initialising quantum registers, creating and using resilient resources for one-way quantum computation, and creating ultracold molecules with large spatial dimensions. These three schemes have in common that they involve the use of superlattices, a laser arrangement that allows the transformation of each lattice site into a double-well potential, and also the manipulation

of the potential barrier between sites.

- In Chap. 2 we present the main physical concepts behind the utilisation of laser light to trap and manipulate ultracold atoms in optical lattices. We present the superlattice setup, and explain why the dynamics of ultracold atoms trapped in such lattices is well described by a tight-binding model. We discuss some of the properties of Wannier functions, introduce a generalises definition of the latter, and present an algorithm aimed at maximising the localisation of Wannier functions in lattices of arbitrary geometry.

- In Chap. 3, we present a scheme to accelerate the initialisation time of a quantum register using a superlattice setup. We propose to initialise a lattice with a filling factor of a half, and to dynamically merge every second site of the lattice with its neighbour, which results in the creation of a Mott-insulating state—the quantum register—with a filling factor of one atom per site. We study this dynamical process numerically and analytically using a time-evolving block decimation algorithm and the Kibble-Zurek theory, respectively. We provide a relation between the interaction parameters of the system and the density of defects in the final state.

- In Chap. 4, we study the dynamics of a spinor-condensate trapped in an optical lattice. We show how to realise a lattice containing in each site a Bell state encoded on the spin-state of the atoms, and examine the possibility to perform exchange gates between spin-encoded qubits using superlattice manipulations. We propose use such manipulations to create many-body states containing a customised amount of entanglement. In the second part, we assume the possibility to perform single-qubit operations, and propose a scheme for creating a two-dimensional entangled state similar to an encoded cluster state that has the advantage of being resilient to collective dephasing noise.

We use a new formalism based on the use of a graphical notation to show that this state constitutes a resource for one-way quantum computations, and show that the resilience of this state to collective dephasing noise is not affected by the application of the measurements required to execute quantum algorithms.

- Chap. 5 is an introduction to the different concepts related to the calculation of diatomic molecular potentials. We also motivate the approach taken in the next chapter to compute the equilibrium position and bonding strength of spatially large diatomic molecules.

- In Chap. 6, we present a superlattice setup aimed at facilitating the creation of diatomic molecules with equilibrium distances comparable to typical lattice spacings. We introduce a method that allows the evaluation of diatomic molecular integrals involving the overlapping charge-density distributions of electrons in Rydberg states. We use a simple ansatz to approximate the wavefunction of molecular states expected to have an equilibrium distance of the order of typical lattice spacings, and evaluate their binding energies. We compute the interaction parameters of an ensemble of Rydberg atoms separated by distances comparable to the typical optical lattice spacing that have overlapping charge-density distributions. We argue that if such a system could be realised by e.g. exciting ground state atoms trapped in an optical lattice to highly-excited states, it would allow the simulation of Fermi-Hubbard Hamiltonians in a defect-less crystal, at temperatures much below the Fermi temperature. These systems would mimic the behaviour of electrons in metallic compounds, and hence facilitate the exploration of the requisite conditions for the emergence of e.g. exotic phase transitions or superconductivity.

- We summarise and conclude in Chap. 7.

Chapter 2

The tools of the trade.

In this chapter, we briefly explain the ideas and the physics behind the utilisation of laser light to trap large numbers of ultracold atoms in arrays of microscopic dipole traps, known as optical lattices. We present a laser configuration called a superlattice that we will use throughout this thesis, and explain how the single-particle dynamics of atoms trapped in such a lattice can be effectively described by a tight-binding model. We then introduce a generalised definition of Wannier functions that we use in the next chapter, and also present an algorithm that allows the optimisation of the localisation of Wannier functions for arbitrary lattice structures.

2.1 Bose-Einstein condensation

The first ingredient necessary to realise a system of ultracold atoms trapped in an optical lattice is a Bose-Einstein condensate (BEC). Unlike fermions, many identical bosonic particles can occupy the lowest single-particle state, in which case these particles are said to "condense" in the ground state. Einstein, in 1924, was the first to predict that below a critical temperature T_c, a finite fraction of the particles contained in an ideal Bose-gas will occupy the lowest energy state. The experimental effort aimed at creating a BEC in dilute gases dates back to 1980, but it was not until 1995 that advances in laser cooling techniques (see e.g. Ref. [33]) made it

possible to reduce the temperature of an ensemble of ^{87}Rb atoms below the critical temperature [34, 35]. The first realisations of a BEC were reported in Refs. [35, 36].

The mechanism of Bose-Einstein condensation can be understood from basic principles of quantum statistics. Here, we will briefly present the theory underlying the formation of BEC, and derive the definition of the critical temperature.

The number of bosonic particles occupying a single-particle state with energy ε is $n(\varepsilon) = (\xi^{-1}\mathrm{e}^{\beta\varepsilon} - 1)^{-1}$, where $\xi = \mathrm{e}^{\beta\mu}$ is the fugacity with μ the chemical potential, $\beta = (k_B T)^{-1}$, k_B is the Boltzmann constant, and T is the temperature of the system. In a homogeneous, non-interacting (ideal) Bose-gas, the energy of a particle corresponds to its kinetic energy $\varepsilon_k = \hbar^2|k|^2/(2m)$, where $\hbar$ is the Planck constant, m is the mass of the particle and k its wave-number. The density of particles inside a volume V is given by

$$\frac{N}{V} = \frac{1}{V}\sum_k (\xi^{-1}\mathrm{e}^{\beta\varepsilon_k} - 1)^{-1} \tag{2.1}$$

$$= \rho_0 + \rho_{\mathrm{ex}}, \tag{2.2}$$

where $\rho_0 = (1/V)[\xi/(1-\xi)]$ is the density of particle in the $k = 0$ state (so $\mu \leq 0$), and $\rho_{\mathrm{ex}} = (1/V)\sum_{k\neq 0}(\xi^{-1}\mathrm{e}^{\beta\varepsilon_k} - 1)^{-1}$ the density of particles in excited states. Using the fact that $(\xi^{-1}\mathrm{e}^{\beta\varepsilon_k} - 1)^{-1} = \xi\mathrm{e}^{\beta\varepsilon_k}/(1 - \xi\mathrm{e}^{\beta\varepsilon_k})$, the density of particles with $k \neq 0$ can be recast into a geometrical series, which yields

$$\rho_{\mathrm{ex}} = \frac{1}{\lambda_T^3} g_{3/2}(\xi), \tag{2.3}$$

where $g_\alpha(\xi) = \sum_{i=1}^{\infty} \xi^i i^\alpha$ and $\lambda_T = [2\pi\hbar^2/(mk_B T)]^{1/2}$. The function $g_{3/2}(\xi)$ reaches its maximum value at $\xi = 1$ ($\mu = 0$) with $g_{3/2}(1) = 2.612$, which corresponds to the value for which the density of particles in the ground state diverges. Also, the maximum density of excited states for a given temperature T is given by $\rho_{ex}^{\max} =$

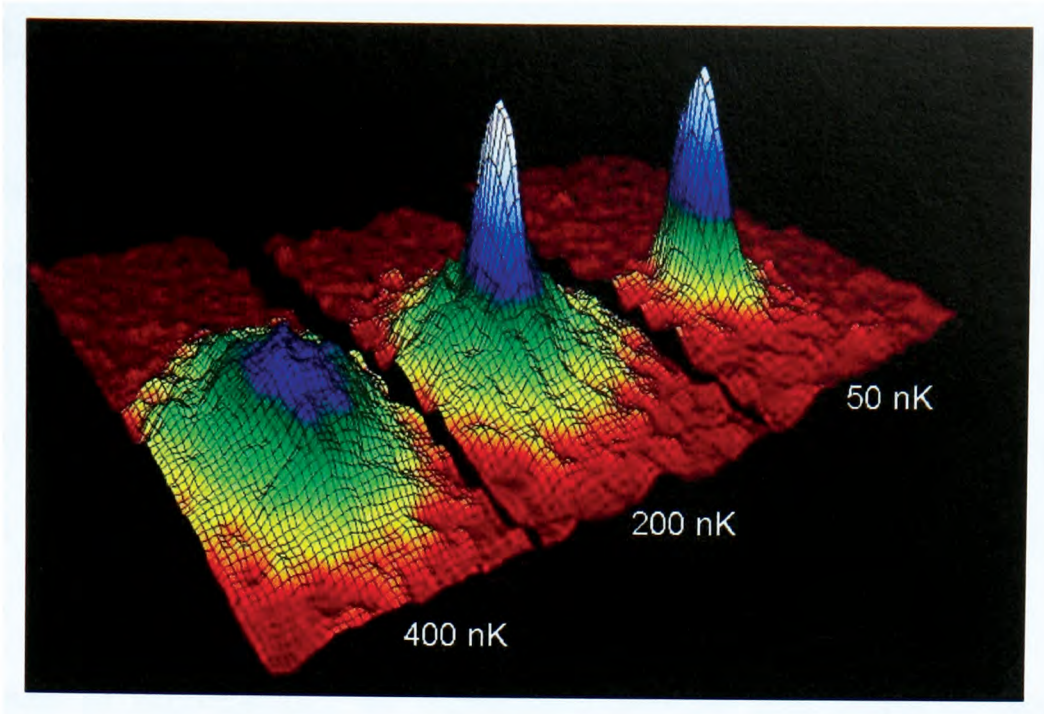


Figure 2.1. Velocity distribution of an ensemble of atoms trapped in a MOT at different temperatures, from hot (left) to cold (right). As the atoms start to condense in their ground state, the velocity distribution of the ensemble exhibits a peak at zero velocity (image from NIST/JILA/CU-Boulder).

$2.612 \times [mk_B T/(2\pi\hbar^2)]^{3/2}$. As a consequence, when the density of particles is fixed to ρ_{fix}, there exists a critical temperature T_c given by

$$T_c = (\rho_{\text{fix}}/2.61)^{2/3} \left(\frac{2\pi\hbar^2}{mk_B}\right), \tag{2.4}$$

below which the single-particle ground state becomes macroscopically occupied.

The presence of a BEC is indicated by a peak in the velocity distribution of the atoms around $k = 0$ (see Fig. 2.1). The typical critical temperature for a BEC of alkali atoms to occur in a dilute gas trapped in a (purely) magnetic trap is $T_c \sim 100\,\text{nK}$. In the first experiment reporting the realisation of a BEC of ^{87}Rb atoms, the condensation started at 170 nK for a density of 2.5×10^{12} atoms per cubic centimetre [35], and the lifetime of the BEC was about *fifteen seconds*. Nowadays, the typical temperature achieved in experiments is of the order of a 10–100 nanokelvins.

2.2 Interactions between atoms in a dilute gas

A striking feature of dilute atomic vapours is that the distances between the atoms are very large compared to the range of their interactions. This observation makes it possible to consider that the dominant form of interactions in such gases is two-body encounters. This allows, along with the fact that collisions happen at very low energy, a drastic simplification of the form of the interaction operator between particles in a BEC.

For the sake of illustration, we consider here the scattering of two particles of mass m_1 and m_2, and assume that they are distinguishable and have no internal degrees of freedom. The wavefunction describing their relative motion satisfies a Schrödinger equation in relative coordinates with the mass equal to the reduced mass $m_r = m_1 m_2/(m_1 + m_2)$. It has the form $\psi_S(\mathbf{r}) \approx \mathrm{e}^{\mathrm{i}\mathbf{kr}} + \psi_{\mathrm{sc}}(\mathbf{r})$, which corresponds to the sum of an incoming plane wave with wavevector $\mathbf{k}$ and a scattered wave, where $\mathbf{r} = \mathbf{r_1} - \mathbf{r_2}$ corresponds to the relative coordinate of the two atoms. At a large distance $\mathbf{r}$ from the scattering centre, the outgoing wave has the form of a spherical wave, that is $\psi_{\mathrm{sc}}(\mathbf{r}) = \mathrm{e}^{ikr} f(\mathbf{k}, \mathbf{k}')/r$, where $f(\mathbf{k}, \mathbf{k}')$ is the scattering amplitude, and $\mathbf{k}'$ with $|\mathbf{k}| = |\mathbf{k}'| = k$ is the wavevector of the scattered wave.

Because the interaction potential is spherically symmetric, the solutions of the Schrödinger equation have an axial symmetry with respect to the direction of the incident particles [37]. This allows the expansion of $\psi_S(\mathbf{r})$ in terms of Legendre polynomials $P_\ell(\cos\theta)$

$$\psi_S(\mathbf{r}) = \sum_{\ell=0}^{\infty} A_\ell P_\ell(\cos\theta) R_{k,\ell}(r), \tag{2.5}$$

where θ is the scattering angle, i.e. the angle between $\mathbf{k}$ and $\mathbf{k}'$. The function $R_{k,l}(\mathbf{r})$ satisfies the radial equation

$$\left[\frac{\mathrm{d}^2}{\mathrm{d}x^2} + \frac{2}{r}\frac{\mathrm{d}}{\mathrm{d}x} + k^2 - \frac{\ell(\ell+1)}{r^2} - \frac{2m_r}{\hbar^2}V(r)\right] R_{k,\ell}(r) = 0, \tag{2.6}$$

where $V(r)$ is the interaction potential [37]. For large inter-atomic separations, that is, far from the scattering centre, the radial functions become $R_{k,\ell}(r \to \infty) = (1/kr)\sin(kr - \frac{\pi}{2}\ell + \delta_\ell)$, where δ_ℓ is a phase shift. The value of δ_ℓ corresponds to the phase shift between an incoming wave and a scattered wave with a relative angular momentum ℓ, and thus represents the effect of the potential on the scattered pair (see e.g. [38]). By expanding the plane wave e^{ikr} in terms of Legendre polynomials, one finds that setting $A_\ell = i^\ell(2\ell+1)e^{i\delta_\ell}$ allows the identification of $f(\mathbf{k},\mathbf{k}')$ with $f_k(\theta) = \frac{1}{k}\sum_{\ell=0}^{\infty}(2\ell+1)e^{i\delta_\ell}\sin\delta_\ell P_\ell(\cos\theta)$ [38].

The number of terms to take into account in the sum of Eq. (2.5) to accurately represent the wavefunction $\psi_S(\mathbf{r})$ corresponds to the relative angular momentum ℓ of the colliding atoms. It can be approximated using the relation $\hbar\ell \simeq m_r v r_{\text{impact}}$ where v is the relative velocity and r_{impact} the impact parameter of the collision, that corresponds to the closest distance between the particles reached during the scattering process [33]. For a collision to happen, the impact parameter must be less than the range r_{int} of the interaction, and so $\hbar\ell \leq m_r v r_{\text{int}} = h r_{\text{int}}/\lambda_{\text{dB}}$ using the De Broglie relation. Since the temperature in a BEC is extremely low, the De Broglie wavelength of the atoms is quite large, normally of the order of $\lambda_{\text{dB}}/(2\pi) \sim 100$ nm [33]. Therefore, we can restrict the definition of ψ_S to its lowest-energy term ($\ell = 0$), which yields $f_k(\theta) = e^{i\delta_0}\sin\delta_0/k$. In this case, the scattering process is said to be purely *s-wave*. Using the relation $\sigma = 4\pi|f_k(\theta)|^2$, the cross section σ of the collision is given by $\sigma = 4\pi(\sin\delta_0/k)^2$ [38]. For low-energy collisions, one can show that in general $\delta_0 = -ka_{sc} + \mathcal{O}(k^2)$, where a_{sc} is called the scattering length. For small velocities $k \to 0$ and the cross section becomes $\sigma = 4\pi a_{sc}^2$ and $|f_k(\theta)| = a_{sc}$.

Using the Green function $G(\mathbf{r})$ defined as $(\nabla + k^2)G(\mathbf{r}) = \delta(\mathbf{r})$, the function $\psi_S(\mathbf{r})$, which is a solution of the Schrödinger equation, can be written in a recursive

form as

$$\psi_S(\mathbf{r}) = \mathrm{e}^{\mathrm{i}\mathbf{kr}} + [2m_r/(\hbar^2)] \int \mathrm{d}\mathbf{r}' V(\mathbf{r}') G(\mathbf{r}-\mathbf{r}') \psi_S(\mathbf{r}'). \tag{2.7}$$

The Green function for this problem is given by $G(\mathbf{r}-\mathbf{r}') = -\mathrm{e}^{\mathrm{i}k|\mathbf{r}-\mathbf{r}'|}/(4\pi|\mathbf{r}-\mathbf{r}'|)$, and it reduces to $G(\mathbf{r}-\mathbf{r}') \simeq -\mathrm{e}^{\mathrm{i}kr}\mathrm{e}^{-\mathrm{i}\mathbf{k}'\mathbf{r}'}/(4\pi r)$ in the limit where the particles are already far from the scattering centre [39]. Applying the Born approximation, we replace $\psi_S(\mathbf{r}')$ in Eq. (2.7) with the zero-th order term $\mathrm{e}^{\mathrm{i}\mathbf{kr}}$, which yields $\psi_S(\mathbf{r}) = \mathrm{e}^{\mathrm{i}\mathbf{kr}} - \frac{m_r}{2\pi\hbar^2}\frac{\mathrm{e}^{\mathrm{i}kr}}{r}\int \mathrm{d}\mathbf{r}'\mathrm{e}^{-\mathrm{i}\mathbf{K}\mathbf{r}'}V(\mathbf{r}')$, where $\mathbf{K} = (\mathbf{k}'-\mathbf{k})$ is sometimes called the transfer vector. By identification, the scattering amplitude is given by $f_{\mathrm{Born}}(\theta) = \frac{m_r}{2\pi\hbar^2}\int \mathrm{d}\mathbf{r}'\mathrm{e}^{-\mathrm{i}\mathbf{K}\mathbf{r}'}V(\mathbf{r}')$, and so we get

$$a_{sc} = \frac{m_r}{2\pi\hbar^2}\left|\int \mathrm{d}\mathbf{r}'\mathrm{e}^{-\mathrm{i}\mathbf{K}\mathbf{r}'}V(\mathbf{r}')\right|. \tag{2.8}$$

The effective form of the interaction potential in real space is obtained by applying an inverse Fourier transform on both sides of Eq. (2.8). This eventually yields the very simple formula

$$V(\mathbf{r_1}-\mathbf{r_2}) = \left(\frac{2\pi a_{sc}\hbar^2}{m_r}\right)\delta(\mathbf{r_1}-\mathbf{r_2}), \tag{2.9}$$

where $\delta(r)$ is the Kronecker delta function. Thus, the action of the interaction operator between particles in an ultracold, dilute gas is entirely specified by the scattering length. The scattering length is usually deduced from experimental data, and is of the order of $a_{sc} \sim 100\, a_0$.

When considering the nuclear and electronic spin degrees of freedom of the particles, two-body scattering processes turn into a multichannel problem. In this case, the scattering length associated with a given collisional process depends on the initial and final internal states of the scattered particles. Collisions conserve the total spin of the pair, and as we will see in Chap. 4, interaction operators involving spinor

particles have the form of projection operators, and are characterised by different scattering lengths.

One remarkable feature of Eq. (2.9) is that the scattering length can be controlled, to a certain extent, using *Feshbach resonances* [37, 39–41]. The idea behind the utilisation of Feshbach resonances is based on the observation that when the energy of a scattered state is close to that of a bound state whose channel is closed, the phase shift—and thus the scattering length—between the incoming and outgoing wave of the scattered state is increased/reduced by an amount proportional to the inverse of the energy difference between the bound and scattered states [39]. This phenomenon is known as a Feshbach resonance, and it can be exploited to control the value of the scattering length by shifting the energy of a bound state close to that of a scattered state using a magnetic field B. One can show that the scattering length of a particle near a Feshbach resonance is given by

$$a_{sc}(B) = a_{bg}\left(1 + \frac{\Delta B}{B - B_0}\right) \tag{2.10}$$

where a_{bg} is the value of the scattering length away from the resonance, ΔB is the width of the resonance, and B_0 is the magnetic field strength at the resonance. Feshbach resonances allow experimentalists to tune the strength of the interactions within a range that varies between atomic species. In some cases interactions can even be turned off, or their signs inverted, which allows, e.g. the formation of molecular condensates [42, 43].

2.3 Optical lattices

2.3.1 The physics of dipole traps

Consider a two level atom of mass m, with an internal ground state $|\,g\rangle$ and a first excited state $|\,e\rangle$ associated with the energies $\hbar\omega_g$ and $\hbar\omega_e$, respectively, located in a loss-less cavity of volume V. Its atomic Hamiltonian is given by

$$\hat{H}_{\text{at}} = \frac{\hat{\mathbf{p}}^2}{2m} + \frac{\hbar}{2}(\omega_e + \omega_g)\hat{\mathbb{1}} + \frac{\hbar}{2}(\omega_e - \omega_g)\hat{\sigma}_z \tag{2.11}$$

where $\hat{\mathbf{p}}$ is the momentum of the atom, $\hat{\mathbb{1}} = |g\rangle\langle g| + |e\rangle\langle e|$ is the unity operator associated with the internal degrees of freedom of the atom and $\hat{\sigma}_z = |e\rangle\langle e| - |g\rangle\langle g|$. When a monochromatic electromagnetic field with a frequency $\omega = 2\pi\nu$, and thus a wavelength of $\lambda = 2\pi c/\omega$ and a wavevector $k = 2\pi/\lambda$, is introduced into the cavity, its energy is described by the simple harmonic oscillator $\hat{H}_{\text{f}} = \hbar\omega[\hat{a}^\dagger\hat{a} + (1/2)]$, where $\hat{a}^\dagger$ is the creation operator of a photon. For convenience, let us define the ladder operators $\hat{\sigma}_+ = |e\rangle\langle g|$ and $\hat{\sigma}_- = |g\rangle\langle e|$. The interaction operator between the atom and the light field is given by $\hat{H}_{\text{af}} = -\hat{\mathbf{d}} \cdot \hat{\mathbf{E}}(\mathbf{r})$, where $\hat{\mathbf{d}}$ is the dipole operator of the atom, and $\hat{\mathbf{E}}(\mathbf{r})$ is the operator of the electromagnetic field. This interaction operator is valid in the limit where the field does not vary very much over the size of the atom, that is, approximately in a region proportional to the size of the Bohr radius $a_B \sim 52 \times 10^{-3}\,\text{nm}$. Since the typical wavelength used in experiments is of the order of a few hundreds of nanometres, then $a_B/\lambda \ll 1$, and atom-light interactions can safely be described by $\hat{H}_{\text{af}}$. In quantised form, the operator describing the electromagnetic field is given by

$$\hat{\mathbf{E}}(\hat{\mathbf{r}}) = \mathrm{i}\mathcal{E}\mathbf{e}\,[\hat{a}W(\mathbf{r}) - \hat{a}^\dagger W^*(\mathbf{r})], \tag{2.12}$$

where $\mathcal{E} = [\hbar\omega/(2\epsilon_0 V)]^{1/2}$ with ϵ_0 the permittivity of free space, $W(\mathbf{r})$ is a mode function (e.g. for plane waves $W(\mathbf{r}) = \mathrm{e}^{-\mathrm{i}\mathbf{kr}}$ and for standing waves $W(\mathbf{r}) = \sin \mathbf{kr}$) and $\mathbf{e}$ is a real field polarisation vector [44]. The dipole operator reads $\hat{\mathbf{d}} = \sum_{i,j=e,g} \mathbf{d}_{ij}|i\rangle\langle j|$, where $\mathbf{d}_{ii} = 0$ and $\mathbf{d}_{eg} = \mathbf{d}_{ge} = -q\langle g|\mathbf{r}|e\rangle$ with q the charge of the electron. The atom-field Hamiltonian becomes

$$\hat{H}_{\mathrm{at-f}} = \hat{H}_{\mathrm{at}} + \hat{H}_{\mathrm{f}} - \mathrm{i}\hbar\kappa(\hat{\sigma}_+ + \hat{\sigma}_-)[\hat{a}W(\mathbf{r}) - \hat{a}^\dagger W^*(\mathbf{r})], \tag{2.13}$$

where $\kappa = \mathcal{E}(\mathbf{d}_{eg} \cdot \mathbf{e}/\hbar)$. Using the operator

$$\hat{U}(t) = \exp\left\{\mathrm{i}[\frac{(\omega_e + \omega_g)}{2}\hat{\mathbb{1}} + (\omega/2)\hat{\sigma}_z + (\hat{a}^\dagger\hat{a} + \frac{1}{2})\omega]t\right\}, \tag{2.14}$$

the corresponding interaction picture Hamiltonian $\hat{H}_I = \hat{U}\hat{H}\hat{U}^\dagger + \mathrm{i}\hbar\dot{\hat{U}}\hat{U}^\dagger$ is given by

$$\hat{H}_I = \frac{\hat{\mathbf{p}}^2}{2m} + \frac{\hbar}{2}\Delta\hat{\sigma}_z - \mathrm{i}\hbar\kappa(\hat{\sigma}_+\mathrm{e}^{\mathrm{i}\omega t} + \hat{\sigma}_-\mathrm{e}^{-\mathrm{i}\omega t})[\hat{a}W(\mathbf{r})\mathrm{e}^{-\mathrm{i}\omega t} - \hat{a}^\dagger W^*(\mathbf{r})\mathrm{e}^{\mathrm{i}\omega t}]. \tag{2.15}$$

The transformation (2.14) removes the time-dependence of the operator products $\hat{a}^\dagger\hat{\sigma}_-$ and $\hat{a}\hat{\sigma}_+$ [44], whilst making the last two non-energy conserving terms $\hat{a}^\dagger\hat{\sigma}_+$ and $\hat{a}\hat{\sigma}_-$ vary much more rapidly. The application of the rotating-wave approximation cancels the two non-conserving terms [44, 45], which yields the Hamiltonian

$$\hat{H}_I = \frac{\hat{\mathbf{p}}^2}{2m} + \frac{\hbar}{2}\Delta\hat{\sigma}_z - \mathrm{i}\hbar\kappa[\hat{\sigma}_+\hat{a}W(\mathbf{r}) - \hat{a}^\dagger\hat{\sigma}_-W^*(\mathbf{r})], \tag{2.16}$$

where the detuning $\Delta = \omega_e - \omega_g - \omega$ [44]. The Hamiltonian (2.16) couples the bare states $|g, n\rangle = |g\rangle|n+1\rangle$ to the states $|e, n\rangle = |e\rangle|n\rangle$, where $|n\rangle$ is an n photon Fock state, thus conserving the number of excitations in the system.

If the detuning $\hbar|\Delta| \gg \hbar\kappa|W(\mathbf{r})|$, then the effect of interactions on the energy of the states $|g, n\rangle$ and $|e, n\rangle$ can be calculated using perturbation theory. In the first

order, the atomic ground state $|\, g, n+1\rangle^{(1)} = |\, g, n+1\rangle - (\kappa\sqrt{n+1}W(\mathbf{r})/\Delta)\,|\, e, n\rangle$, and hence the probability of finding the atom in its ground state is given by $P_g = \Delta^2/[\Delta^2 + (\kappa\sqrt{n+1}W(\mathbf{r})/\Delta)]^2 \approx 1$. Consequently, using projection methods, we can safely derive an effective Hamiltonian by adiabatically eliminating the excited state [46]. The projection of the Hamiltonian onto the manifold of the state $|\, g, n\rangle$ yields, up to the second order, the effective Hamiltonian

$$\hat{H}_g^{\text{eff}} = \frac{\hat{\mathbf{p}}^2}{2m} + \hbar\frac{|\Omega(\mathbf{r})|^2}{\Delta}\hat{a}^\dagger\hat{a}, \tag{2.17}$$

where $\Omega(\mathbf{r}) = \kappa W(\mathbf{r})$ is the Rabi-frequency [46]. The effective Hamiltonian reveals that the presence of the light field shifts the energy levels of the atom, thus creating an energy potential proportional in strength to the field mode function $|W(\mathbf{r})|^2$. This is the very principle behind the realisation of optical lattices.

An electromagnetic field in the form of a standing wave is obtained by the superposition of two counter-propagating laser beams aligned on the same axis. Let us consider a standing-wave along the x–axis with a field mode function $W(\mathbf{r}) = \sin kx$ whose state is described by a coherent state

$$|\, \alpha\rangle = \exp(-|\alpha|^2/2)\sum_{n=0}^{\infty}\frac{\alpha^n}{\sqrt{n!}}\,|\, n\rangle\,, \tag{2.18}$$

with average photon number $\langle\alpha\,|\hat{a}^\dagger\hat{a}|\,\alpha\rangle = |\alpha|^2$. In such a field, the Hamiltonian $\hat{H}_{\text{OL}}$ describing the motion of a ground state atom is given by

$$\langle\alpha\,|\,\langle g\,|\,\hat{H}_g^{\text{eff}}\,|\, g\rangle\,|\,\alpha\rangle = \frac{\hat{\mathbf{p}}^2}{2m} + \hbar\frac{|\tilde{\Omega}(\mathbf{r})|^2}{\Delta} \tag{2.19}$$

$$= \frac{\hat{\mathbf{p}}^2}{2m} + V_{\text{OL}}(\mathbf{r}) \tag{2.20}$$

$$= \hat{H}_{\text{OL}}, \tag{2.21}$$

where $\tilde{\Omega}(\mathbf{r}) = \sqrt{\langle n \rangle}\Omega(\mathbf{r})$ and $V_{\mathrm{OL}}(\mathbf{r}) = V_0 \sin^2 kx$ with $V_0 = \sqrt{\langle n \rangle}\hbar\kappa^2/\Delta$. It is customary (and convenient) to express the energy of the Hamiltonian $\hat{H}_{\mathrm{OL}}$ in units of the *recoil energy* $E_R = \hbar^2 k^2/(2m)$. We consider that there is a large number of photons, and thus, since $\Delta n \simeq n - 1$, we neglect the variations of the potential strength due to the variation of the photon number. If the detuning $\Delta > 0$ (blue detuned), the energy minima are located at the minima of the light intensity, whereas if $\Delta < 0$ (red detuning), the potential is attractive and the positions of the energy minima correspond to the places of maximum intensity.

In practice the atoms have many more than two levels, and thus the simplified picture presented above to describe the interactions of the atoms with a laser field may seem obsolete, as the actual potential felt by the ground state atoms should actually be proportional to the sum of the contributions from all their internal states. However, for alkali atoms in the limit of a far-detuned laser field, the main contribution to the potential typically comes from a single excited state, and so the two-level picture is quite appropriate.

For the atoms to be trapped in such a potential, their kinetic energy must be much smaller than the typical potential depth ($\sim 30\,\mathrm{kHz}$), which requires very low temperatures such as those found in BECs. In order to trap ultracold atoms in an optical lattice, the atoms are first cooled down until they form a BEC, and then loaded into the optical potential by adiabatically switching on the laser field. Once the atoms are trapped in the lattice, their lifetime is proportional to the intensity of the laser, and the colour of the detuning. If we introduce a finite lifetime $1/\Gamma_e$ for the excited state[1], the energy of ground state atoms becomes a complex quantity whose imaginary part is proportional to the rate of loss of ground state atoms [47]. This loss rate is $\propto \hbar\Gamma_e|\tilde{\Omega}(\mathbf{r})|^2/\Delta^2$. Hence, it increases with the light intensity $I \propto \mathcal{E}^2$,

[1]The quantity $1/\Gamma_e$ corresponds to the time for occupation of the excited state to be reduced by a factor of e

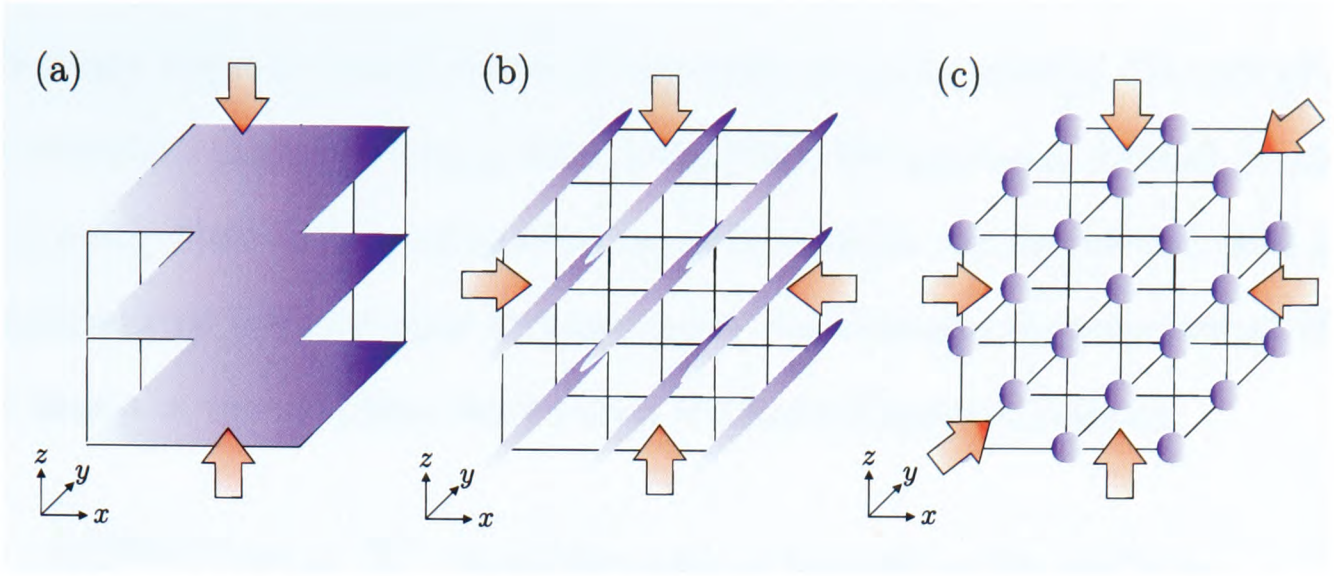


Figure 2.2. The superposition of several counter-propagating laser beams in different spatial directions creates intensity fields with a crystal-like structure. [image courtesy of Stephen Clark]

and decreases as $1/\Delta^2$, which allows the atoms to have a long lifetime even in deep optical lattices. Also, spontaneous emissions are larger in a red detuned lattice than in a blue detuned one [48]. Using typical parameters in experiments [49], one finds that the rate of loss of ground-state atoms is slow, e.g. of the order of minutes for a blue detuned lattice with $V_0 = 25E_R$.

2.3.2 Lattice geometries

The superposition of several pairs of counter-propagating laser beams in different directions creates lattice potentials in two and three dimensions (see Fig. 2.2). In the simplest 3D case, three pairs of orthogonal linearly polarised counter-propagating laser beams form the square potential

$$V_{\mathrm{OL}}^{(\mathrm{square})}(\mathbf{r}) = V_{0,x}\sin^2 k_x x + V_{0,y}\sin^2 k_y y + V_{0,z}\sin^2 k_z z, \tag{2.22}$$

where $V_{0,\gamma}$ ($\gamma = x, y, z$) is the amplitude and k_γ the wavenumber of the standing wave oriented along the γ–direction. The lattice thus produced has a period $a_\gamma = \lambda_\gamma/2$ in the γ–direction.

In many respects, the situation of ultracold atoms trapped in 3D optical potentials resembles that of electrons interacting with the potential created by the ions of a crystal. Most lattice geometries found in crystals can be realised with optical potentials using different laser arrangements. For instance, the interference of three laser beams in the xy-plane can be used to create hexagonal lattices

$$V_{\mathrm{OL}}^{(\mathrm{hexagonal})}(\mathbf{r}) = \sum_{j=1,2,3} V_0 \sin^2(kx\cos\theta_j + ky\sin\theta_j) + V_{0,z}\sin^2 k_z z, \tag{2.23}$$

where $\theta_1 = -\theta_3 = \pi/3$ and $\theta_2 = \pi$, or triangular lattices

$$V_{\mathrm{OL}}^{(\mathrm{triangular})}(\mathbf{r}) = 3 + 4\cos(3kx/2)\cos(\sqrt{3}ky/2) + 2\cos(\sqrt{3}ky) + V_{0,z}\sin^2 k_z z, \tag{2.24}$$

such as those found in graphite or solid ^{3}He structures, respectively (see e.g. Refs [50, 51]). In contrast to electrons in solids, however, ultracold atoms trapped in optical lattices evolve in an absolutely defect-less potential, in the absence of phonons, and the possibility to tune the laser parameters, such as the intensity or the laser geometry, offers many very desirable features that are not available in solid-state systems. For instance, by setting the potential barrier in one direction of space to a very large value, the motion of the particles in this direction is frozen out, which allows the realisation of effectively one- or two-dimensional systems. Also, very remarkably, the structure of the lattice can be modified dynamically. This allows the simultaneous manipulation of atoms trapped in the lattice, a feature that makes the optical lattice a system of choice in the context of quantum information processing (see e.g. Ref. [48]).

Throughout this thesis, we will use another laser arrangement called a *superlattice* that consists of a superposition of two laser beams with different wavelengths

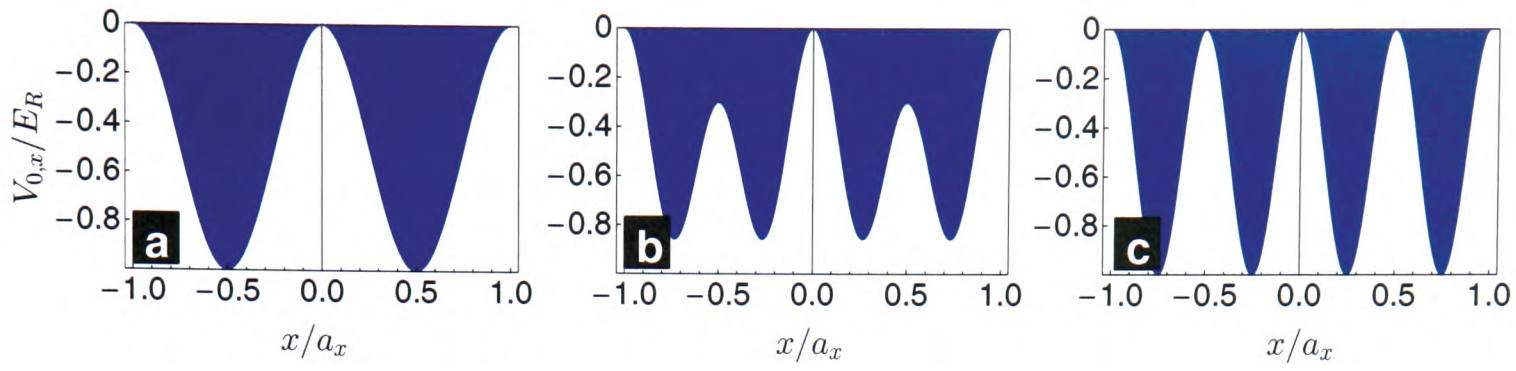


Figure 2.3. Profile of a superlattice potential along the x-direction with $V_{0,x} = 1E_R$ for (a) $s = 0$, (b) $s = 0.7$ and (c) $s = 1$.

λ_L and λ_S along the same direction

$$V_{\mathrm{OL}}^{\mathrm{super}}(\mathbf{r}, s) = V_{0,y} \sin^2 k_y y + V_{0,z} \sin^2 k_z z - V_{0,x}[(1-s)\sin^2(k_{x,L}x) + s\sin^2(k_{x,S}x)], \tag{2.25}$$

where $k_{x,L} = 2\pi/\lambda_L$ and $k_{x,S} = 2\pi/\lambda_S$. The wavelengths are related by an integer factor of proportionality η such that $\lambda_L = \lambda_S/\eta$, and the parameter s controls the relative intensity of the two lasers. Starting with $\eta = 2$ and $s = 0$, progressively increasing the parameter s turns the lattice potential into an array of double-well potentials until it recovers the shape of a sinusoidal lattice with a shorter periodicity for $s = 1$ (see Fig. 2.3).

Potentials of the same type as Eq. (2.25) have recently been implemented in a number of experiments (see e.g. [52, 53]). They offer the possibility to control interactions between neighbouring sites by raising or lowering the potential barrier separating them, and also to dynamically double the number of sites in a lattice, thus changing its filling factor. Sophisticated arrangements allow the selective manipulation of the potential barrier between neighbouring sites in the left/right or up/down directions of the plane, or to shift one side of the double-well before merging two sites into one [54–56]. Because they allow the control of the atomic interactions between neighbouring atoms in parallel, superlattices considerably extend the possibilities

offered by optical lattices to engineer or manipulate the quantum state of large ensembles of atoms [32]. So far, superlattices have successfully been used to realise entangling operations between neighbouring atoms, and to engineer Heisenberg-type spin Hamiltonians [52, 55].

2.4 Single particle in optical (super-)lattices

Since the potential experienced by the atoms in an optical lattice is periodic, their energy levels exhibit a band structure [38, 57]. For simplicity, let us consider here the Hamiltonian (2.21) in the x–direction, the extension to the three-dimensional case being straightforward.

By virtue of the Bloch theorem, since $V_{\mathrm{OL}}(x) = V_{\mathrm{OL}}(x+a_x)$ the eigenfunctions of the Hamiltonian (2.21) associated with the energy level n have the form of a plane wave multiplying a function with the periodicity of the lattice

$$\psi_{n,q}(x) = \mathrm{e}^{\mathrm{i}qr} u_{n,q}(x), \tag{2.26}$$

where $u_{n,q}(x) = u_{n,q}(x + a_x)$, which in turn implies that

$$\psi_{n,q}(x + a_x) = \mathrm{e}^{\mathrm{i}qa_x} \psi_{n,q}(x). \tag{2.27}$$

The function $\psi_{n,q}(x) = \langle\, x \,|\, \psi_{n,q} \,\rangle$ is called the Bloch function of the crystal, and $u_{n,q}(x) = \langle\, x \,|\, u_{n,q} \,\rangle$ its associated Bloch orbital. The Bloch theorem introduces the vector q, which is often called the crystal momentum, or quasi-momentum. However, it does not correspond to the particle momentum in the crystal, and must be seen as a quantum number characterising the translational symmetry of the lattice [57].

Introducing the condition $u_{n,q}(x) = u_{n,q}(x + a_x)$ into the Schrödinger equation

yields the following equation for the Bloch orbitals

$$\hat{H}_q u_{n,q}(x) = \varepsilon_q^{(n)} u_{n,q}(x) \tag{2.28}$$

$$\left[\frac{(\hat{p}+q)^2}{2m} + V_{\mathrm{OL}}(x)\right] u_{n,q}(x) = \varepsilon_q^{(n)} u_{n,q}(x), \tag{2.29}$$

where $\varepsilon_q^{(n)}$ is the energy associated with the Bloch function $\psi_{n,q}(x)$. As a consequence of the translational invariance of the lattice potential, the energy levels $\varepsilon_q^{(n)}$ form energy bands labelled by n. Also, defining $G_i = 2\pi j/a_x$, they have the property that $\varepsilon_q^{(n)} = \varepsilon_{q+G_j}^{(n)}$ $\forall j$, and thus it is sufficient to consider just those values of q inside the first Brillouin zone defined as $-\pi/a_x < q \leq \pi/a_x$.

Because Bloch functions obey Eq. (2.27), they can always be written as a Fourier series in plane waves of the form

$$\psi_{n,q}(x) = \sum_j \mathrm{e}^{\mathrm{i}qa_x j} w_n(x - ja_x) \tag{2.30}$$

for any fixed x, where the functions $w_n(x-ja_x) = \langle\, x \,|\, w_{n,j} \,\rangle$ are centred at site j, and are orthogonal with respect to the band and site indices [58]. These functions are called Wannier functions, they form an orthonormal basis set, and will be described in more detail in the next section [57, 59].

Using Eqs. (2.30) and (2.28), the matrix elements of the Hamiltonian $\hat{H}_q$ are given by

$$(\hat{H}_q)_{nm} = \left\langle \psi_{n,q} \middle| \hat{H}_q \middle| \psi_{m,q} \right\rangle = \sum_j \mathrm{e}^{\mathrm{i}qaj} \varepsilon(j)_{nm}, \tag{2.31}$$

where the matrix element $\varepsilon(j)_{nm} = \left\langle w_{n,j} \middle| \hat{H}_q \middle| w_{m,0} \right\rangle$. When the Hamiltonian $(\hat{H}_q^{\mathrm{eff}})_{nm} = \sum_{j=-j_{\mathrm{eff}}}^{j_{\mathrm{eff}}} \mathrm{e}^{\mathrm{i}qaj} \varepsilon(j)_{nm}$ resulting from the truncation of the sum in Eq. (2.31) reproduces accurately the band structure $\varepsilon_q^{(n)}$, it corresponds to an effective single-particle Hamiltonian for the system. In the simplest case $j = -1, 0, 1$, the effective Hamil-

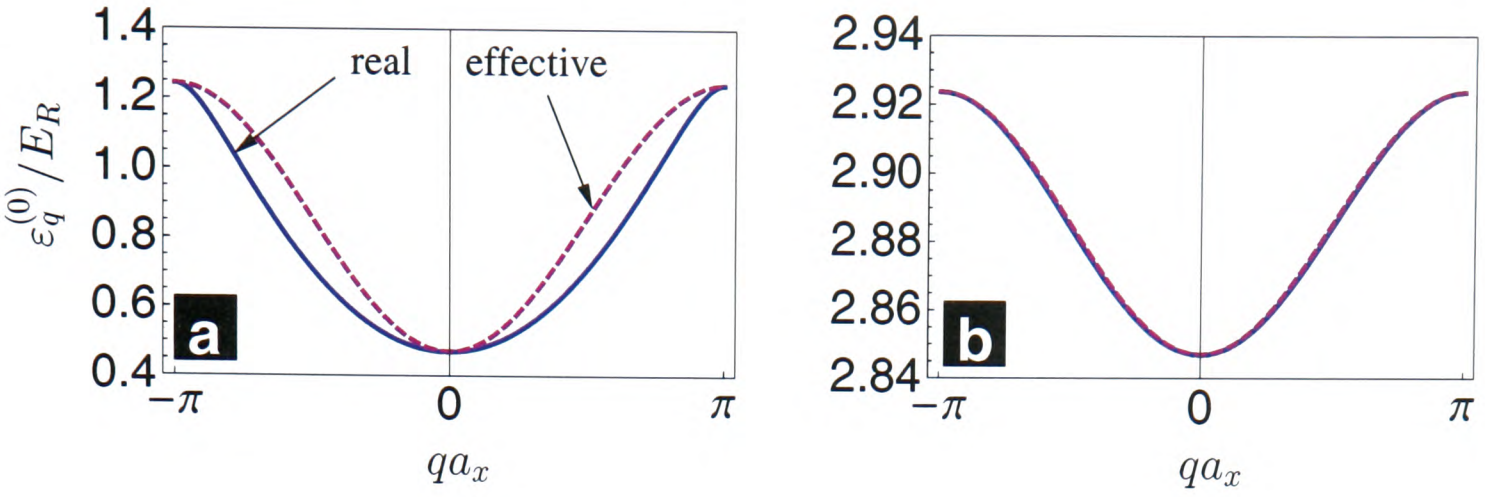


Figure 2.4. First energy band of a square lattice for (a) $V_{0,x} = 1E_R$ and (b) $V_{0,x} = 10E_R$. The dotted lines denote the energy of the effective tight-binding Hamiltonian.

tonian is said to be tight-binding, since it only involves basis functions located in neighbouring sites.

Considering only one band, the effective tight-binding Hamiltonian yields an energy of the form $\varepsilon_q^{(n),\text{eff}} = E+2J\cos a_x q$, where the parameters E and J correspond to the on-site energy of a particle, and J to the hopping rate between two sites. In this case the hopping term corresponds to $[\varepsilon_{\pi/a_x}^{(n),\text{eff}} - \varepsilon_0^{(n),\text{eff}}]/4$, that is a quarter of the bandwidth. In Fig. 2.4, the exact energy of the first band of a square lattice is plotted alongside the energy of the effective tight-binding Hamiltonian with fitted parameters E and J. The effective Hamiltonian reproduces the exact band structure very accurately for $V_{0,x} > 10\,E_R$.

The same cannot be said for the band structure associated with the superlattice potential (2.25). In Fig. 2.5a, we plot the two first energy bands associated with the potential (2.25) with $s = 0.9$ and compare it with effective energies of the form $\varepsilon_q^{(i),\text{eff}} = E_i+2J_i\cos a_x q$. Even for $V_{0,x} = 10\,E_R$, the agreement between the exact and effective Hamiltonian is mediocre. This situation could be improved by including terms in the sum of Eq. (2.31) that involve matrix elements between basis states associated with more distant sites. Alternatively, the introduction in the definition of

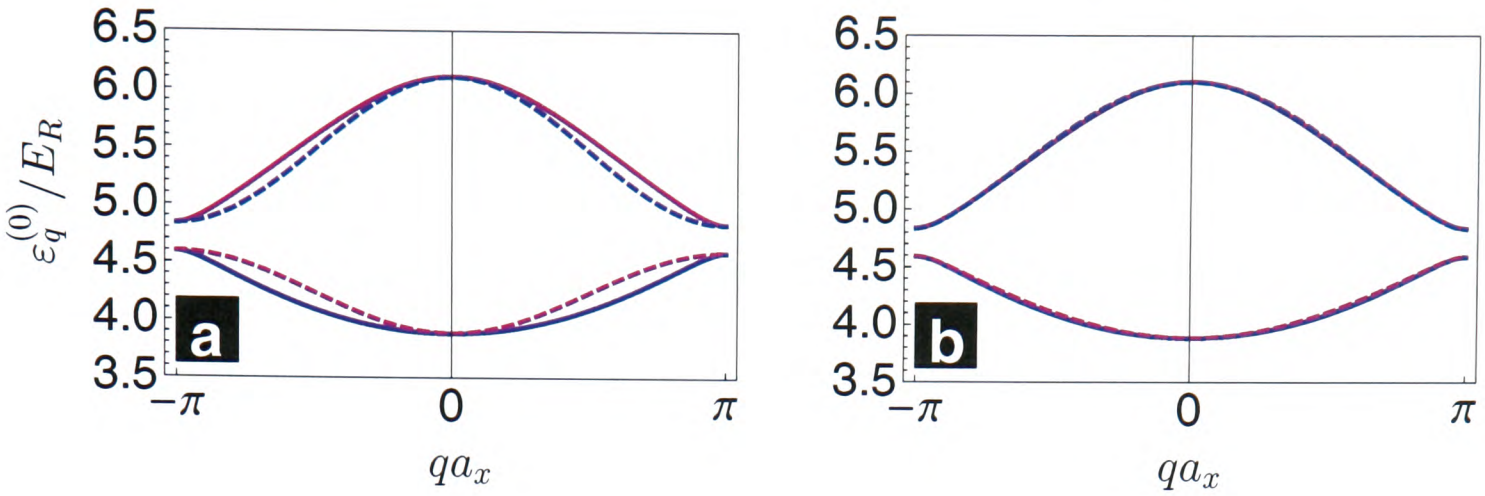


Figure 2.5. First and second energy bands of a superlattice potential with $s = 0.9$ and $V_{0,x} = 10E_R$. The dotted lines denote the energy of an effective tight-binding Hamiltonian (a) without off-diagonal matrix elements and (b) with diagonal matrix elements.

the effective Hamiltonian of terms $\varepsilon(j)_{nm} = -\varepsilon(-j)_{nm}$ with $n \neq m$— which yields off-diagonal matrix elements of the form $(\hat{H}_q^{\text{eff}})_{nm} = (\hat{H}_q^{\text{eff}})_{mn}^* = \mathrm{i}2J_{nm} \sin a_x q$— considerably improve the agreement between the exact energy and the eigenvalues of the effective Hamiltonian (see Fig. 2.5b). Therefore, the single-particle dynamics in optical superlattices can also be effectively described by a tight-binding model. We will use this fact in the next chapter where we derive a model describing the dynamics of ultracold atoms trapped in a superlattice potential. The possibility to use a single particle tight-binding model is desirable in the context of numerical simulations, as it allows the description of the single particle dynamics using solely nearest-neighbour hopping terms, which facilitates the construction of the Hamiltonian.

2.5 Wannier functions

As we have stated in the previous section, Wannier functions form an orthonormal basis that allows the expansion of the Bloch functions of single particles in terms of localised wavefunctions. Thus, they constitute a set of choice to define the bosonic field operators used to derive the parameters of models describing many-

body lattice problems (see e.g. Refs. [3, 48]). They are also essential for evaluating quantities such as quasi-momentum distributions from experimental data sets (see e.g. Refs. [60–62]).

In this section, we discuss the general properties of Wannier functions. We introduce a generalised definition of the latter that we will use in the next chapter to compute the parameters of a tight-binding model describing the dynamics of particles in a superlattice potential. In such models, the parameters related to the single-particle dynamics of the system can be fitted from the band-structure, and so the use of Wannier functions is only necessary to evaluate the matrix elements of two-particles interaction operator. We also present an algorithm based on the use of generalised Wannier functions that allows the evaluation of maximally localised functions for arbitrary lattice geometries.

2.5.1 Simple Wannier functions

The Wannier function (WF) associated with a site with position $\mathbf{R}$ in a multidimensional crystal is defined as the Fourier transform of the crystal's Bloch function

$$w_n(\mathbf{r}-\mathbf{R}) = \frac{V}{(2\pi)^3}\int_{\mathrm{BZ}} \mathrm{d}\mathbf{q}\mathrm{e}^{-\mathrm{i}\mathbf{q}\mathbf{R}}\psi_{n,\mathbf{q}}(\mathbf{r}), \tag{2.32}$$

where BZ denotes the Brillouin zone, and V is the size of a unit cell of the lattice, e.g. $V = a_x a_y a_z$ for a square lattice [63, 64] (see Fig. 2.6). In crystals, the position of the sites corresponds to the location of the atoms; in optical lattices, they correspond to the location of the field intensity minima for blue detuned optical lattices, and maxima for red detuned ones. In the following, we use the notation $\langle\, \mathbf{r} \,|\, \mathbf{R}n \,\rangle = w_n(\mathbf{r}-\mathbf{R})$, with $\mathbf{R}$ the location of the "home" cell. As a consequence of the orthogonality of the Bloch functions $\langle\, \psi_{n,\mathbf{q}} \,|\, \psi_{n',\mathbf{q}'} \,\rangle = \delta_{n,n'}\delta_{\mathbf{q}',\mathbf{q}}$, WFs form an orthogonal set of basis functions with respect to both band and site indices, that

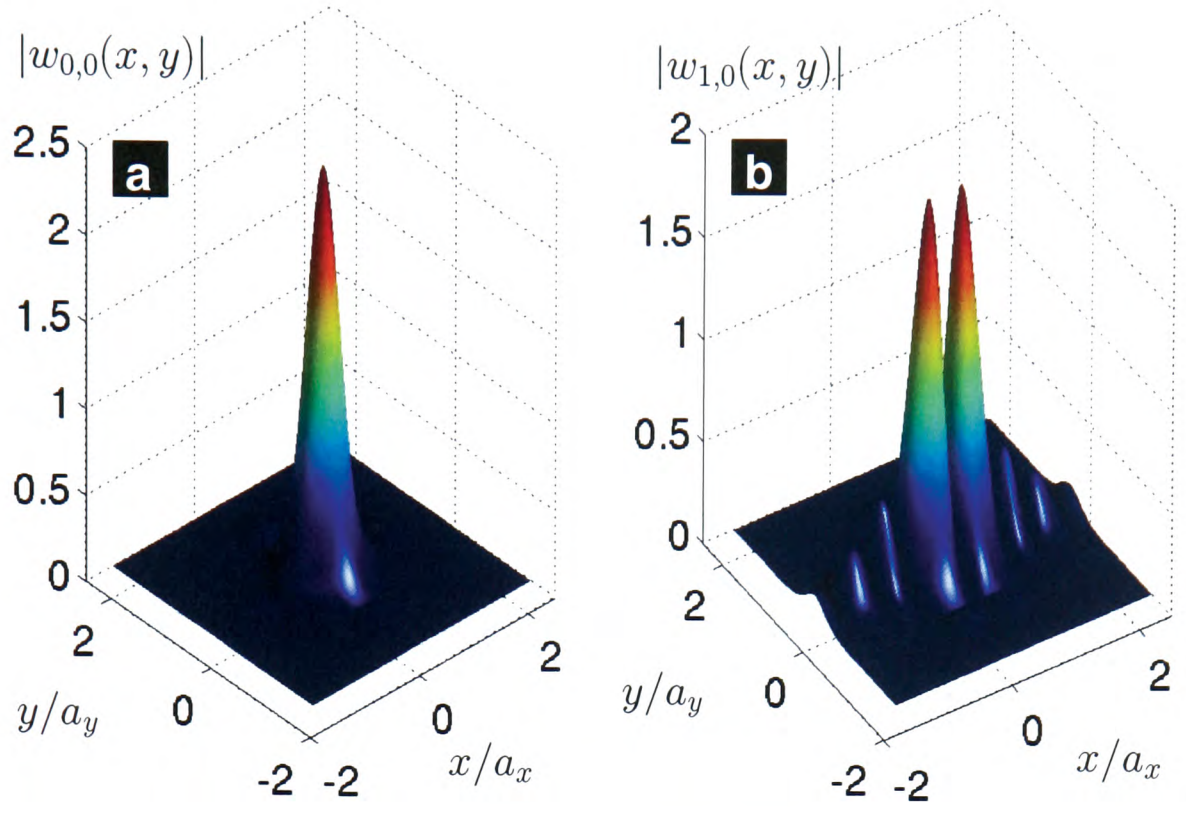


Figure 2.6. 2D representation of the Wannier functions for the (a) lowest and (b) first-excited band of a 2D isotropic square lattice with $V_{0,x} = V_{0,y} = 5E_R$.

is $\langle \mathbf{R}n \,|\, \mathbf{R}'n' \rangle = \delta_{n,n'}\delta_{R,R'}$. In analogy to the case of particles in free space, the Bloch function can be understood as the representation of a particle wave-function in (quasi-)momentum space. Hence, its Fourier transform, the WF, can be seen as the position representation of the particle's wave-function in the lattice [65].

In spite of their rather simple definition, WFs have the peculiarity that they are not uniquely defined. Indeed, given a set of Bloch orbitals, an equally valid set is obtained by applying the transformation

$$u_{n,\mathbf{q}}(\mathbf{r}) \rightarrow \mathrm{e}^{\mathrm{i}\phi_n(\mathbf{q})}\, u_{n,\mathbf{q}}(\mathbf{r}), \tag{2.33}$$

where $\phi_n(\mathbf{q})$ is a real function of $\mathbf{q}$. The choice of the phases $\phi_n(\mathbf{q})$ does not affect the centre of WFs, but it does affect their localisation properties, by which we mean their spread. Therefore, the non-uniqueness of the definition of WFs forces us to

choose a convention for the phase, that is, to fix a definition for the WFs we want to use.

The convention that is most often used involves choosing the phase that produces the set of WFs that is the most localised, that is, the WFs with the smallest spread

$$\Omega = \sum_n [\langle r^2 \rangle_n - \langle r \rangle_n^2], \tag{2.34}$$

where n runs over the different band indices of the WFs present in the basis set, and $\langle \circ \rangle_n = \langle \mathbf{R}n \,|\, \circ \,|\, \mathbf{R}n \rangle$ [65, 66]. This choice of phase clarifies the interpretation of WFs, as it assigns a well defined location to the particles evolving in the lattice. Also, the use of localised WFs allows the simplification of the models describing the particle dynamics in the lattice, as their use when evaluating interaction matrix elements favours local interactions. In the case of optical lattices, the well-localised WFs associated with the atoms produce on-site interaction terms that are at least 10^3 times greater (from $V_0 = 5E_R$ in a square lattice) than nearest-neighbour interactions, which allows these terms to be neglected. Thus, the dynamics of the atoms in such setups is accurately described by the Bose-Hubbard model (see e.g. Refs. [3, 48]).

2.5.2 Approximations of Wannier functions

In the simple case of a square lattice, good approximations of the WFs can be obtained by expanding the lattice potential around its minima to second order [48]. This procedure yields an harmonic potential with frequency $\omega_\gamma = \sqrt{4V_{0,\gamma}E_R}/\hbar$ ($\gamma = x, y, z$), which makes it possible to equate the WF associated with the lowest band with the ground state wavefunction of the harmonic oscillator

$$w_0(\mathbf{r} - \mathbf{R}) \sim \prod_{\gamma=x,y,z} (\pi a_{0,\gamma}^2)^{-1/4} \mathrm{e}^{-(r_\gamma - R_\gamma)^2/(2a_{0,\gamma}^2)},$$

where $a_{0,\gamma} = (m\omega_\gamma 2/\hbar)^{-1/2}$.

The utilisation of this approximation greatly simplifies the calculation of the system's interaction parameters [3, 48]. Also, since the energy gap $\Delta E_\gamma = \hbar\omega_\gamma$ between levels is known, it provides a useful estimate of the gap between different energy bands of the lattice.

2.5.3 Comment on the nearsightedness of particles evolving in a lattice

If we take $u_{n,\mathbf{q}}(\mathbf{r}) \approx u_n(\mathbf{r})$, then the WF centred at site $\mathbf{R} = 0$ is given by $w_n(\mathbf{r}) \approx u_n(\mathbf{r})[\sin(k\mathbf{r})/(k\mathbf{r})]$. This WF is identical to the Bloch orbital at $\mathbf{R} = 0$, and then decays rapidly into oscillations of decreasing amplitude proportional to $\sim 1/r$. This decaying behaviour is very characteristic of WFs. In general, it can be shown that the decay properties of WFs are closely related to the analyticity properties of Bloch functions [63, 67].

For simplicity, let us consider a one-dimensional Fourier transform

$$g(r) = \int_{-\infty}^{\infty} \mathrm{e}^{\mathrm{i}qr} g(q)\mathrm{d}q, \tag{2.35}$$

where $g(q)$ is an integrable function. For instance, if $g(q)$ is a piece-wise continuous function that is one in the interval $k \in [-1, 1]$ and zero elsewhere, then the function $g(r) = 2\sin(r)/(r)$ decays proportionally to $1/r$. Using integration by parts, one finds after some algebra that

$$r^{\ell+1} g(r) \leq (-\mathrm{i})^{-\ell} \int_{-\infty}^{\infty} \mathrm{e}^{\mathrm{i}kr} \left(\frac{\partial}{\partial k}\right)^{\ell} g(k)\,\mathrm{d}k. \tag{2.36}$$

This inequality indicates that if the ℓ-th derivative of $g(k)$ is continuous, then $g(r)$ will decay as $\sim r^{-(l+1)}$. So in fact, the decay properties of Fourier transforms depend

on how many derivatives of $g(q)$ are continuous [67].

It was shown that Bloch orbitals, as well as the band energy, are analytic functions of the quasi-momentum $\mathbf{q}$ [63, 68]. Thus, WFs decay faster than algebraically, i.e. any power of r [63, 67]. By convention, one then says that WFs decay exponentially, as opposed to algebraically, although at that point the notion of exponential decay does not mean that they decay *strictly* like an exponential function (see e.g. Figs. 2.7 and 2.8). In general, the amplitude of WFs cannot decay faster, whatever choice of phases $\phi_n(\mathbf{q})$, than an exponential function such that $|w_n(r)| \sim |r|^\alpha \exp(-h|r|)$ where α and h are real numbers [64, 67, 69, 70].

2.5.4 Generalised Wannier functions

Using the definition of Eq. (2.32), one finds that the hopping rate of the particle between sites $\mathbf{R}$ and $\mathbf{R}'$ yields $\left\langle \mathbf{R}n \left| \hat{H}_{\mathrm{OL}} \right| \mathbf{R}'m \right\rangle = \delta_{nm} \frac{V}{(2\pi)^3} \int_{\mathrm{BZ}} \mathrm{d}\mathbf{q}\, \mathrm{e}^{-\mathrm{i}\mathbf{q}(\mathbf{R}-\mathbf{R}')} \varepsilon_{\mathbf{q}}^{(n)}$. Consequently, since intra-band hopping terms are equal to zero, this definition of WFs does not allow the inclusion of off-diagonal matrix elements in the definition of the single particle Hamiltonian (2.31). More general WFs are obtained by using another gauge transformation involving the Bloch orbitals associated with different energy bands

$$u_{n,\mathbf{q}}(\mathbf{r}) \rightarrow \sum_m U_{mn}^{(\mathbf{q})}\, u_{m,\mathbf{q}}(\mathbf{r}), \tag{2.37}$$

where $U_{mn}^{(q)}$ is a unitary matrix that mixes the bands at wavevector k. The previous gauge (2.33) can be seen as a special case of Eq. (2.37) for a diagonal $U_{mn}^{(q)}$. Now the index n of the *generalised* Bloch orbital (2.37) is no longer associated with a band, but with a given mixing of several bands. Also, because they involve several bands, hopping terms between generalised Wannier functions (GWFs) with different indices n are allowed. This is a useful property, since as we have seen in Sec. 2.4, in the case of superlattices the accuracy of the tight-binding model is improved by the

inclusion of intra-band hopping terms in the effective single-particle Hamiltonian. We will use GWFs to compute the matrix elements of two-body interactions in the next chapter where we derive a model describing the dynamics of ultracold atoms trapped in superlattices. We will see that the mixing matrices $U_{mn}^{(q)}$ associated with the GWFs can be related to the eigenvectors of the effective Hamiltonian of the system using a simple relation [71].

2.5.5 Optimisation of Wannier functions

When it is possible to separate the variables of the lattice potential, as in the case of the square lattice or superlattice potential we use in the next chapter, the WFs associated with the lattice can be written in the form $w_{n_x,n_y,n_z}(\mathbf{r}) = w_{n_x}(x)w_{n_y}(y)w_{n_z}(z)$. The improvement of localisation of multidimensional WFs of this form is then facilitated by the fact that the WFs associated with each direction of space can be optimised separately using an algorithm described in Refs. [49, 66] based on the minimisation of the Berry curvature of the 1D band. For more sophisticated lattice geometries, the optimisation of WFs is more problematic. Such a method was recently proposed, and is based on the idea that GWFs can be used to minimise the spread (2.34) by appropriately choosing the elements of the matrices $U_{mn}^{(\mathbf{q})}$. It was originally published by Marzari *et al.* in Ref. [66] for the purpose of studying the electric polarisation of crystalline insulators, and more generally bond properties in crystals. We present this method below, and discuss some of its limitations.

This optimisation method is based on the first observation that the spread operator (2.34) can be expanded into two parts

$$\Omega = \Omega_I + \tilde{\Omega}, \tag{2.38}$$

where

$$\Omega_I = \sum_n \left[\langle r^2 \rangle_n - \sum_{\mathbf{R},\mathbf{m}} |\langle \mathbf{Rm} | \mathbf{r} | \mathbf{0n} \rangle|^2 \right], \tag{2.39}$$

and

$$\tilde{\Omega} = \sum_n \sum_{\mathbf{R}m \neq \mathbf{0}n} |\langle \mathbf{Rm} | \mathbf{r} | \mathbf{0n} \rangle|^2. \tag{2.40}$$

It was shown that the first term is actually invariant to gauge transformations. In contrast, the second term of Eq. (2.38) is not. Also, since this term is positive definite, its minimisation leads automatically to a reduction of the spread.

However, the minimisation of $\tilde{\Omega}$ in real space is computationally very demanding. The key observation of Marzari *et al.* is that this minimisation can be carried out more easily in momentum space, for when sampling momentum space only the first Brillouin zone need be considered, which is comparatively easier to sample than even a restricted portion of real space. Using the relation

$$\langle \mathbf{R}n | \mathbf{r} | \mathbf{0}m \rangle = \mathrm{i} \frac{V}{(2\pi)^3} \int \mathrm{d}\mathbf{q}\, \mathrm{e}^{\mathrm{i}\mathbf{q}\mathbf{R}} \langle u_{n\mathbf{q}} | \nabla_{\mathbf{q}} | u_{m\mathbf{q}} \rangle \tag{2.41}$$

the spread operator Ω can be recast in terms of integrals in q-space. The discretisation of this expression for the purpose of deriving an optimisation algorithm is obtained via the transformation

$$\frac{V}{(2\pi)^3} \int \mathrm{d}\mathbf{q} \rightarrow \frac{1}{N} \sum_{\mathbf{q}}, \tag{2.42}$$

where N is the number of cells in the system, and a discretised version of n-dimensional derivatives given by

$$\nabla f(\mathbf{q}) = \sum_{\mathbf{b}} w_b \mathbf{b} [f(\mathbf{q} + \mathbf{b}) - f(\mathbf{q})], \tag{2.43}$$

where $\mathbf{b}$ is a vector connecting a $\mathbf{q}$-point to one of its Z neighbours that satisfies the

condition $\sum_{\mathbf{b}} w_b b_\alpha b_\beta = \delta_{\alpha\beta}$ by an appropriate choice of weights w_b. For instance, in a cubic lattice $Z = 6$ and the weights are given by $w_b = 1/(2|b|^2)$. The discretisation of the spread operator involves sums of terms of the form $\langle u_{n\mathbf{q}} | \nabla_{\mathbf{q}} | u_{m\mathbf{q}} \rangle = \sum_{\mathbf{b}} w_{\mathbf{b}} \mathbf{b} [M_{nm}^{(\mathbf{q},\mathbf{b})} - 1]$, where

$$M_{nm}^{(\mathbf{q},\mathbf{b})} = \langle u_{n,\mathbf{q}} | u_{m,\mathbf{q}+\mathbf{b}} \rangle . \tag{2.44}$$

Consequently, once the spread operator has been expressed in discretised q-space, it can be reduced to a functional of the quantity $M_{nm}^{(\mathbf{q},\mathbf{b})}$.

The next observation made by Marzari *et al.* is that an infinitesimal gauge transformation given by

$$U_{mn}^{(\mathbf{q})} = \delta_{mn} + \mathrm{d}W_{mn}^{(\mathbf{q})}, \tag{2.45}$$

where $\mathrm{d}W$ is an infinitesimal matrix $\mathrm{d}W^\dagger = -\mathrm{d}W$, modifies the value of the spread as a consequence of the fact that it transforms $|u_{n,\mathbf{q}}\rangle \rightarrow |u_{n,\mathbf{q}}\rangle + \sum_m \mathrm{d}W_{mn}^{(q)} |u_{m,\mathbf{q}}\rangle$ and hence the quantity $M_{nm}^{(\mathbf{q},\mathbf{b})}$. Using elements of matrix differential calculus, an expression relating the difference of the spread with respect to the matrix $\mathrm{d}W$ was found to be

$$G^{(\mathbf{q})} = \frac{\mathrm{d}\Omega}{\mathrm{d}W^{(\mathbf{q})}} = 4 \sum_{\mathbf{b}} w_b (\mathcal{A}[R^{(\mathbf{q},\mathbf{b})}] - \mathcal{S}[T^{(\mathbf{q},\mathbf{b})}]), \tag{2.46}$$

where $\mathcal{A}[B] = (B - B^\dagger)/2$ and $\mathcal{S}[B] = (B + B^\dagger)/(2\mathrm{i})$ are superoperators, $R_{mn}^{(\mathbf{q},\mathbf{b})} = M_{nm}^{(\mathbf{q},\mathbf{b})} M_{nn}^{(\mathbf{q},\mathbf{b})*}$ and $T_{mn}^{(\mathbf{q},\mathbf{b})} = q_n^{(\mathbf{q},\mathbf{b})} M_{nm}^{(\mathbf{q},\mathbf{b})} / M_{nn}^{(\mathbf{q},\mathbf{b})}$.

Eq. (2.46) is particularly remarkable, as it allows the use of a steepest descent algorithm to minimise the spread. Using Eq. (2.46), one step of the steepest descent algorithm transforms an initial matrix $W_0^{(\mathbf{q})}$ to $W_1^{(\mathbf{q})} = W_0^{(\mathbf{q})} + \epsilon G^{(\mathbf{q})}$ where $\epsilon = \alpha/(4w)$ is an infinitesimal positive number with $w = \sum_{\mathbf{b}} w_b$ and α a parameter of the order of one. This provides an expression to update the infinitesimal matrix $\mathrm{d}W^{(\mathbf{q})} \simeq \Delta W^{(\mathbf{q})} = \epsilon G^{(\mathbf{q})}$ in a way that decreases the spread. Indeed, using the

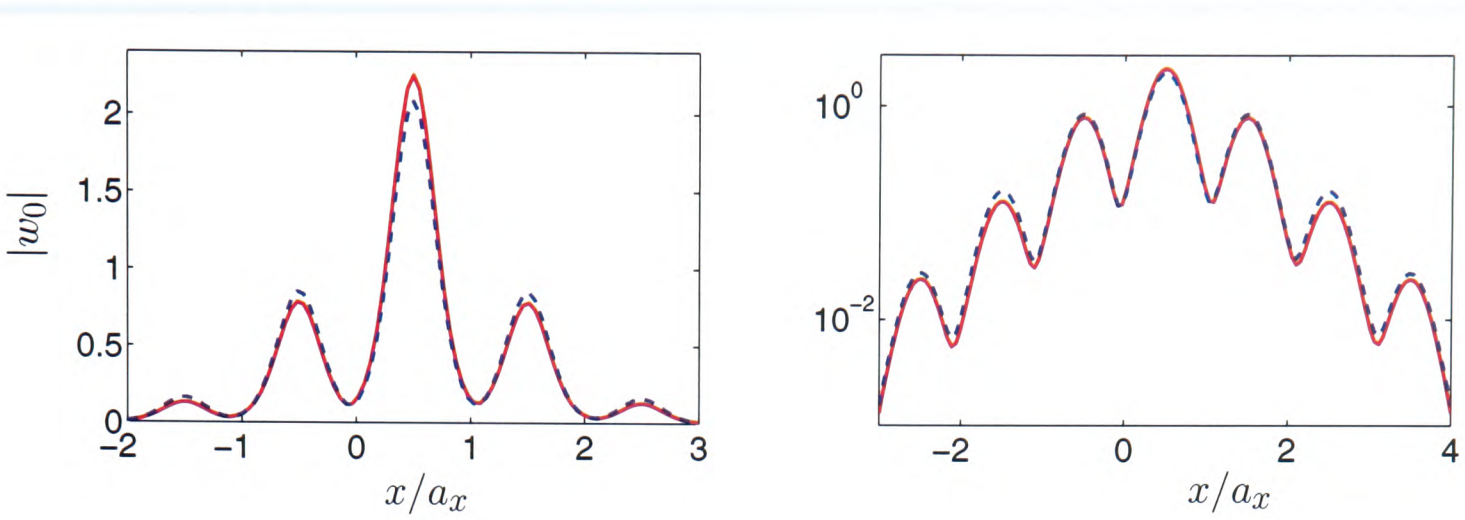


Figure 2.7. Initial (dashed) and optimised WFs of the lowest band along the x-direction for a square lattice with $V_{0,x} = 10E_R$ using an initial set of Bloch orbitals that produces poorly localised WFs. Although the localisation procedure has converged within 0.01%, its effect is quite modest.

property of the trace of the matrix derivative $\mathrm{tr}(A\mathrm{d}X)/\mathrm{d}X = A$ and $\mathrm{d}W^\dagger = -\mathrm{d}W$, one finds that the difference $\mathrm{d}\Omega$ between the initial spread and the spread after one step is given by $\mathrm{d}\Omega = -\epsilon \sum_{\mathbf{q}} ||G^{(\mathbf{q})}||^2 < 0$ where $||X||^2 = \sum_{mn} |X_{mn}|^2$. Therefore, the application of one step of the steepest descent algorithm reduces the value of the spread, hence improving the localisation of the GWFs.

Starting with an initial set of Bloch orbitals $\{|\, u_{n,\mathbf{q}}\rangle^{(0)}\}$, the tensor $M_{nm}^{(\mathbf{q},\mathbf{b})(0)}$ is evaluated and the initial mixing matrix is set to $U_{mn}^{(q)} = \delta_{mn}$. After each step of the steepest descent algorithm, the mixing matrices are updated as $U^{(\mathbf{q})} \rightarrow U^{(\mathbf{q})} \exp[\mathrm{d}W^{(\mathbf{q})}]$, and the new set of $M_{nm}^{(\mathbf{q},\mathbf{b})}$ as $M_{nm}^{(\mathbf{q},\mathbf{b})} = U^{(\mathbf{q})\dagger} M_{nm}^{(\mathbf{q},\mathbf{b})(0)} U^{(\mathbf{q}+\mathbf{b})}$. These steps are repeated until convergence is obtained. The initial set of Bloch orbitals has to be chosen such that its associated WFs are already well-localised within each site. It was reported in several places (see e.g. [59, 72]) that a good choice of initial functions facilitates the convergence of the algorithm.

When the energy bands are well separated, the particle dynamics is effectively described by considering only a single-band. In this situation, the above algorithm

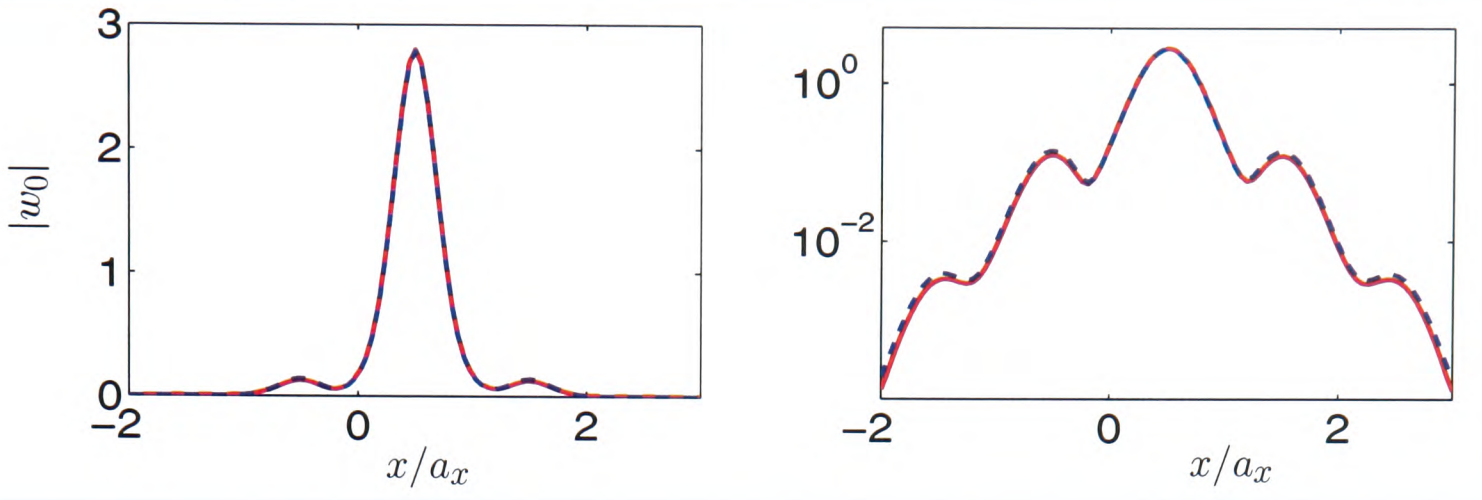


Figure 2.8. Initial (dashed) and optimised WFs of the lowest band along the x-direction for a square lattice with $V_{0,x} = 10E_R$ using an initial set of Bloch orbitals that produces already well-localised WFs.

can be simplified by taking

$$G^{(\mathbf{q})} = \mathrm{i}4 \sum_{\mathbf{b}} w_b \mathrm{Im} \ln M^{(\mathbf{q},\mathbf{b})} \tag{2.47}$$

to generate maximally localised WF associated with a single-band in multiple dimensions. To illustrate the different features and limitations of the localisation algorithm, we have used Eq. (2.47) for the case of a two-dimensional square lattice. Since the variables of the square potential are separable, the 2D WF of the lowest band $w_0(x, y) = w_0(x)w_0(y)$ is equal to the product of two one-dimensional WFs that can be optimised separately. The 2D WFs thus obtained are optimally localised, and hence they are left unchanged by the localisation procedure. This allows comparison of the 2D WFs resulting from the localisation procedure starting from an initial set of Bloch orbitals producing less well-localised WFs. We have obtained the best results for a sampling of the q-space with $\Delta q = 2\pi/40$, and obtained a convergence of the spread operator within 0.01% after a few tens of steps of the steepest-descent procedure.

As reported in Ref. [72], the localisation algorithm applied to 2D WFs does not

always converge to the optimal solution for which $d\Omega$ vanishes, and its effect can therefore be modest. This problem is related to the nature of steepest-descent algorithm that can be trapped in local minima close to the optimal solution. Starting with an initial set of Bloch orbitals producing poorly localised WFs, we have experienced the same problem, and found that the algorithm converged to a non-optimal solution (see Fig. 2.7). In this case, the choice of the initial set of Bloch orbitals is essential, the best initial sets being those producing already well-localised WFs (see Fig. 2.8). Another issue related to the use of the localisation procedure is concerned with its sensitivity to different sampling of the q-space, and the value of the parameter α. These points are discussed in Ref. [66], where it is asked whether higher-order finite-difference representations of $\nabla_{\mathbf{q}}$ would improve this issue. However, the inclusion of higher-order terms increases the complexity of the algorithm, and makes it even slower. As suggested in Ref. [66], changing the value of the parameter α during the steepest-descent algorithm may improve the results and help to avoid false local minima, although this requires the implementation and testing of different strategies for different types of geometries and sampling, which is computationally demanding especially in higher dimensions or when considering many bands.

As a consequence of the different points discussed above, the utilisation of this localisation procedure proves difficult in the context of dynamical simulations, since it involves optimising the parameters of the algorithm for every change of lattice configuration. Hence, when the variables of the potential can be separated, it is more advantageous to consider products of optimally localised 1D WFs that are simpler to compute. However, it must be stressed that the localisation procedure from Marzari *et al.* remains a very useful tool when dealing with very sophisticated lattice geometries, for which already well-localised WFs cannot be found from first principles.

Chapter 3

Publication

Fast initialisation of a high-fidelity quantum register using optical superlattices.

Benoit Vaucher, Stephen R. Clark, Uwe Dorner, Dieter Jaksch

Clarendon Laboratory, University of Oxford, Parks Road, Oxford OX1 3PU, United Kingdom

New J. Phys. **9**, 221 (2007)

We propose a method for the fast generation of a quantum register of addressable qubits consisting of ultracold atoms stored in an optical lattice. Starting with a half filled lattice we remove every second lattice barrier by adiabatically switching on a superlattice potential which leads to a long wavelength lattice in the Mott insulator state with unit filling. The larger periodicity of the resulting lattice could make individual addressing of the atoms via an external laser feasible. We develop a Bose-Hubbard-like model for describing the dynamics of cold atoms in a lattice when doubling the lattice periodicity via the addition of a superlattice potential. The dynamics of the transition from a half filled to a commensurately filled lattice is analysed numerically with the help of the Time Evolving Block Decimation algorithm and analytically using the Kibble-Zurek theory. We show that the time scale for the whole process, i.e. creating the half filled lattice and subsequent doubling of the lattice periodicity, is significantly faster than adiabatic direct quantum freezing of a superfluid into a Mott insulator for large lattice periods. Our method therefore provides a high fidelity quantum register of addressable qubits on a fast time scale.

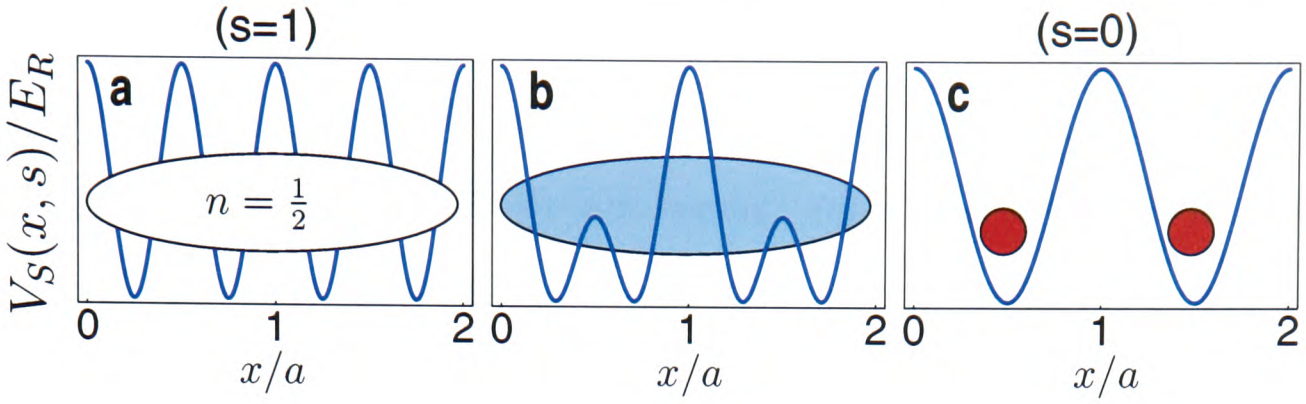


Figure 3.1. (a) The initial profile of the lattice is associated with the value of $s = 1$. The periodicity of the lattice is then progressively doubled (b) until it reaches its final profile (c) associated with the parameter $s = 0$. The number of sites M corresponds to the number of unit cells in the large lattice limit. By starting with a filling factor of $n = 1/2$, this procedure leads to a lattice with filling factor of $n = 1$.

3.1 Introduction

Systems of cold atoms trapped in optical lattices provide the unique opportunity to coherently manipulate a large number of atoms [48, 73, 74]. The remarkable degree of experimental control offered by these systems, as well as the possibility to use the internal hyperfine states of the atoms to encode qubits, make them particularly suited for quantum information processing (QIP). In this context, optical lattices in a Mott-insulating (MI) state with unit filling can be viewed as the realisation of a quantum register, and it is possible to collectively manipulate the qubits stored in such a register experimentally [11, 16]. However, in many quantum computing schemes based on neutral atoms stored in optical lattices the application of single qubit gates [74] or single qubit measurements [13] requires the ability to address single atoms with a focused laser beam. This remains experimentally challenging since these operations have to be performed without perturbing the state of other atoms in their vicinity.

A number of strategies have been proposed to circumvent this problem by using global operations [10, 75, 76], e.g. via "marker atoms" which are moved to a par-

ticular lattice site and interact with the corresponding register qubit such that an external laser affects only that qubit [8]. Another way is simply to use a quantum register in which the atoms are distant enough such that they can be addressed individually by a laser. This method requires an optical lattice with filling factor $n = 1$ in the MI state with a sufficiently large distance between the atoms [77]. The initialisation time of a MI state is proportional to the tunneling time of the atoms between neighbouring sites. Therefore, by using the conventional method of quantum-freezing a superfluid (SF) state [5, 11, 78, 79], it scales exponentially with the lattice spacing [47, 80, 81].

In this paper we propose an alternative method to generate a long wavelength lattice with one atom per site in the MI state. Starting with a one dimensional lattice with a short period—and hence a short initialisation time—and filling factor $n = 1/2$ we remove every second potential barrier by adiabatically turning on a superlattice. This superlattice potential has already been experimentally realised [54, 82]. This procedure eventually leads to a long wavelength lattice in which the periodicity has been doubled and where the atoms are in a MI state with $n = 1$ (see figure 3.1). This scheme does not require changing the angles of the intersecting laser beams. Furthermore, we show that our method allows for the initialisation of a MI state with unit filling factor on a time-scale which, although scaling exponentially with the final lattice spacing, is approximately one order of magnitude smaller than the direct quantum-freezing method. Although we only consider the case of an homogeneous lattice, the results presented in this paper extend to the case of weak harmonic confinements, quartic [83] and box traps [84].

This paper is structured as follows: In Sec. 3.2 we introduce the model used to describe the system dynamics. In Sec. 3.3.1 we discuss ground state properties, particularly two-site correlation functions and quasi momentum distributions. Also, we present and discuss numerical results for the probability of staying in the ground

state during the transition depending on the speed of the ramping. In Sec. 3.3.2 we apply the analytical Kibble-Zurek theory and compare it with our numerical results. Finally, we summarise and conclude in Sec. 3.4.

3.2 Model

We consider a gas of interacting ultracold bosonic atoms loaded into a three dimensional optical lattice. The lattice is formed by pairwise orthogonal standing wave laser fields and its optical potential is given by [3]

$$V_{OL}(\mathbf{r}, s) = V_T \left[\sin^2(kz) + \sin^2(ky)\right] - V_S(x, s). \tag{3.1}$$

Here V_T is the depth of the potential in the y– and z–directions created by pairs of lasers with wave number $k = 2\pi/\lambda$, wave length λ and period $a_T = \lambda/2$. The extension to the case of different optical potentials in the y– and z–directions is straightforward. In the x–direction two pairs of laser beams with a long wavelength λ_L and short wavelength $\lambda_S = \lambda_L/2$ are applied. The potential in the x-direction is thus given by

$$V_S(x, s) = V_0 \left(1 - s\right) \sin^2\left(k_L x\right) + V_0\, s\, \sin^2\left(k_S x\right), \tag{3.2}$$

with V_0 the depth of the lattice, $k_L = 2\pi/\lambda_L$ and $k_S = 2\pi/\lambda_S$. The depths of the potentials will be expressed in units of the recoil energy $E_R = k_L^2/2m$ with m the mass of the atoms (taking $\hbar = 1$ throughout). The parameter $s \in [0, 1]$ is determined by the relative intensities of the two pairs of lasers. By changing s from 1 to 0 the lattice profile is continuously transformed from a sinusoidal potential with a small period $a_S = \lambda_S/2$ to one with a long period $a = \lambda_L/2$, thus halving the number of lattice sites per unit length along the x-direction (see figure 3.1). The lattice

constant a corresponds to the size of a unit cell for $s < 1$ [1]. We refer to the lattice profile with parameters $s = 1$ and $s = 0$ as to the *small lattice limit* and the *large lattice limit*, respectively.

The Hamiltonian of the system in second quantisation reads

$$\hat{H} = \int \mathrm{d}\mathbf{r}\, \hat{\psi}^\dagger(\bar{\mathbf{r}})\, \hat{h}_0(\bar{\mathbf{r}})\, \hat{\psi}(\bar{\mathbf{r}}) + \frac{g}{2} \int \mathrm{d}\mathbf{r}\, \hat{\psi}^\dagger(\bar{\mathbf{r}})\, \hat{\psi}^\dagger(\bar{\mathbf{r}})\, \hat{\psi}(\bar{\mathbf{r}})\, \hat{\psi}(\bar{\mathbf{r}}), \tag{3.3}$$

where $\hat{h}_0(\bar{\mathbf{r}}) = -(1/2m)\nabla^2 + V_{OL}(\bar{\mathbf{r}})$ is the one-particle Hamiltonian. The symbol $\bar{\mathbf{r}} = (\mathbf{r}, s)$ represents the position variable $\mathbf{r}$ and lattice parameter s. The interaction between the atoms is modelled by s-wave scattering with $g = 4\pi a_s/m$ where a_s is the s-wave scattering length. The bosonic field operators obey the usual commutation relations $[\psi(\bar{\mathbf{r}}), \psi^\dagger(\bar{\mathbf{r}}')] = \delta(\mathbf{r} - \mathbf{r}')$ with δ denoting the Dirac delta function.

We restrict our considerations to the case where V_T is sufficiently large so that motion along the y– and z–directions is frozen. The dynamics of the system is then effectively one dimensional along the x–direction. As shown in figure 3.2a the two lowest bands of the Hamiltonian $\hat{h}_{0,x} = -(1/2m)\,(\mathrm{d}/\mathrm{d}x)^2 + V_S(x, s)$ are separated in energy by much less than the typical motional excitation energy $E_{\mathrm{ex}} = \sqrt{4V_0 E_R}$ [3] for values $s \approx 1$ [2]. Therefore, despite assuming that atoms loaded into the lattice are ultracold, we have to consider the two lowest Bloch bands in x–direction to obtain an accurate description of the atomic dynamics. However, excitations to higher bands in the y– and z–directions are neglected in our investigations since we assume that the temperature of the atomic cloud is $k_B T \ll E_{\mathrm{ex}}$. We then expand the bosonic field operator as

$$\hat{\psi}(\bar{\mathbf{r}}) = \sum_{i=1}^{M} \phi_{a,i}(\bar{\mathbf{r}})\, \hat{a}_i + \sum_{i=1}^{M} \phi_{b,i}(\bar{\mathbf{r}})\, \hat{b}_i, \tag{3.4}$$

where M is the number of lattice sites and $\hat{\alpha}_i^\dagger$ $(\alpha = a, b)$ creates a particle in the

[1] To avoid any discontinuity, we work with a lattice periodicity of a even in the case $s = 1$.

[2] The two lowest bands form two segments of the lowest Bloch band if a cell size of $a/2$ is used in the case $s = 1$.

mode associated with the localised function $\phi_{\alpha,i}(\bar{\mathbf{r}})$ centred at site i. The mode functions $\phi_{\alpha,i}(\bar{\mathbf{r}}) = w_{\alpha,i}(x,s)W_{i,0}(y)W_{i,0}(z)$ are factorised into a product of well localised Wannier functions (WF) $W_{i,0}$ of the lowest Bloch band in the y– and z–directions [57] and mode functions $w_{\alpha,i}(x,s)$ in x–direction. The aim of the next section is to describe the single particle dynamics in the tight binding (TB) approximation. If we were to use Wannier functions for $w_{\alpha,i}(x,s)$ this approximation would restrict our model to sinusoidal Bloch bands [59]. Because of the deviation of the lowest two bands from a sinusoidal dispersion relation (see figure 3.2a) when $s \approx 1$ we instead use generalised Wannier function (GWFs) for $w_{\alpha,i}(x,s)$ (see 3.A for a detailed definition and a description of their properties) [66]. By exploiting the optimisation procedure described in 3.A we calculate GWFs $w_{\alpha,i}(x,s)$ which are well localised at lattice sites i. Typical shapes of GWFs and the effects of optimising their localisation are shown in figure 3.3. We note that these GWFs are in general composed of superpositions of Bloch orbitals of both bands and are not related to Wannier functions by a local transformation. Only when $s \approx 0$ the $w_{\alpha,i}(x,s)$ are equivalent to the Wannier functions of the first and the second Bloch band, respectively. Finally, they are always (anti-)symmetric with respect to the centre of the lattice site i for $\alpha = a$ ($\alpha = b$).

3.2.1 Single-particle Hamiltonian

Inserting the approximate field operator equation (3.4) into the first term of equation (3.3) yields the single-particle part of the Hamiltonian in terms of $\hat{a}_i^\dagger$ and $\hat{b}_i^\dagger$. Applying the tight binding approximation, which amounts to keeping only nearest-

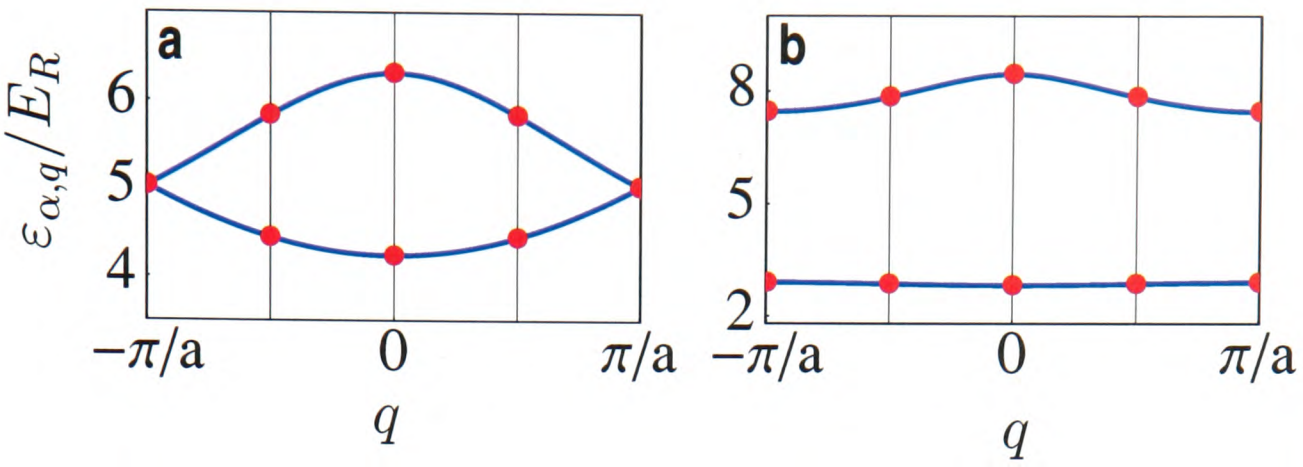


Figure 3.2. Band structure along the x–direction in (a) the small and (b) large lattice limit for $V_0 = 10E_R$. The points represents the values of q for $q = 0, \pi/a, \pi/2a$. The value of $\varepsilon_{\alpha,q}$ correspond to the energy of single-particles with momentum q in the α–th Bloch band. In the small lattice limit, the two first Bloch bands are connected.

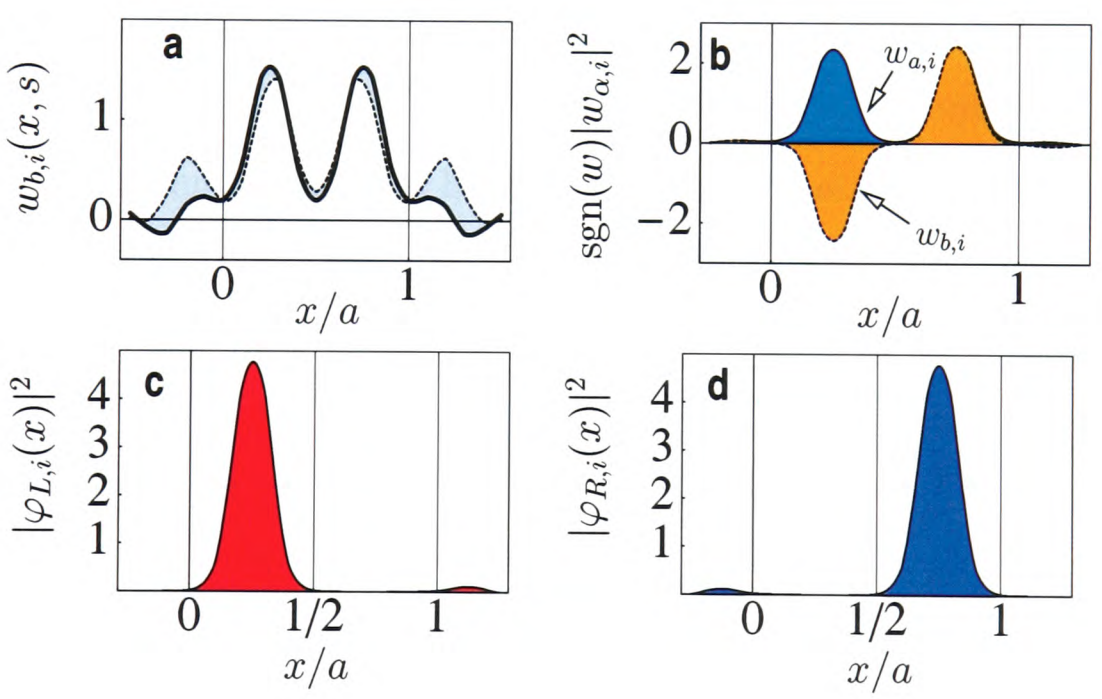


Figure 3.3. (a) Optimised (thick line) and non-optimised (dashed line) GWFs associated with the first mode for $V_0 = 30E_R$ and the lattice profiles $s = 1$. The area between the optimised and non-optimised mode functions is shaded in order to illustrate how the localisation procedure reduces the spread of the optimised function. (b) The square of the mode functions for $V_0 = 30E_R$ and $s = 1$. By combining the mode functions shown in (b), we can construct two new mode functions corresponding to particles localised in either the left (c) or the right (d) well of a given site.

neighbour hopping terms, the single-particle Hamiltonian can be approximated by

$$\begin{aligned}\hat{H}_0(s) &= \sum_{i=1}^{M-1}\left(J_{bb}(s)\,\hat{b}_i^\dagger\hat{b}_{i+1} - J_{aa}(s)\,\hat{a}_i^\dagger\hat{a}_{i+1} + \text{h.c}\right)\\ &+ \sum_{i=1}^{M-1}\left(J_{ba}(s)\,\hat{b}_i^\dagger\hat{a}_{i+1} - J_{ab}(s)\,\hat{a}_i^\dagger\hat{b}_{i+1} + \text{h.c.}\right)\\ &+ \sum_{i=1}^{M}\left(V_a(s)\,\hat{a}_i^\dagger\hat{a}_i + V_b(s)\,\hat{b}_i^\dagger\hat{b}_i\right),\end{aligned} \tag{3.5}$$

where

$$J_{\alpha\beta}(s) = \int \mathrm{d}x\, w^*_{\alpha,i}(x,s)\,\hat{h}_{0,x}(s)\,w_{\beta,i+1}(x,s), \tag{3.6}$$

is the hopping matrix element between neighbouring sites along the x–axis and

$$V_\alpha(s) = \int \mathrm{d}x\, w^*_{\alpha,i}(x,s)\,\hat{h}_{0,x}(s)\,w_{\alpha,i}(x,s), \tag{3.7}$$

is the local on-site energy of a particle in mode α. Note that hopping between modes a and b within one site is not allowed by the symmetry properties of the GWFs. However, the inclusion of non-zero hopping matrix elements J_{ab} and J_{ba} is essential to accurately reproduce the single particle behaviour of the full Hamiltonian (3.3). The symmetry properties of WFs would not allow the inclusion of these terms [59].

For periodic boundary conditions, the parameters V_α and $J_{\alpha,\beta}$ can be found from the band structure without explicit calculation of the mode functions (see 3.B). The numerical values of V_α and $J_{\alpha,\beta}$ for $V_0 = 30E_R$ are shown in figure 3.4a. Using these parameters, we find that $\hat{H}_0(s)$ very accurately reproduces the band structure of the exact Hamiltonian for all values of s, thus justifying the utilisation of the TB approximation and the corresponding GWFs.

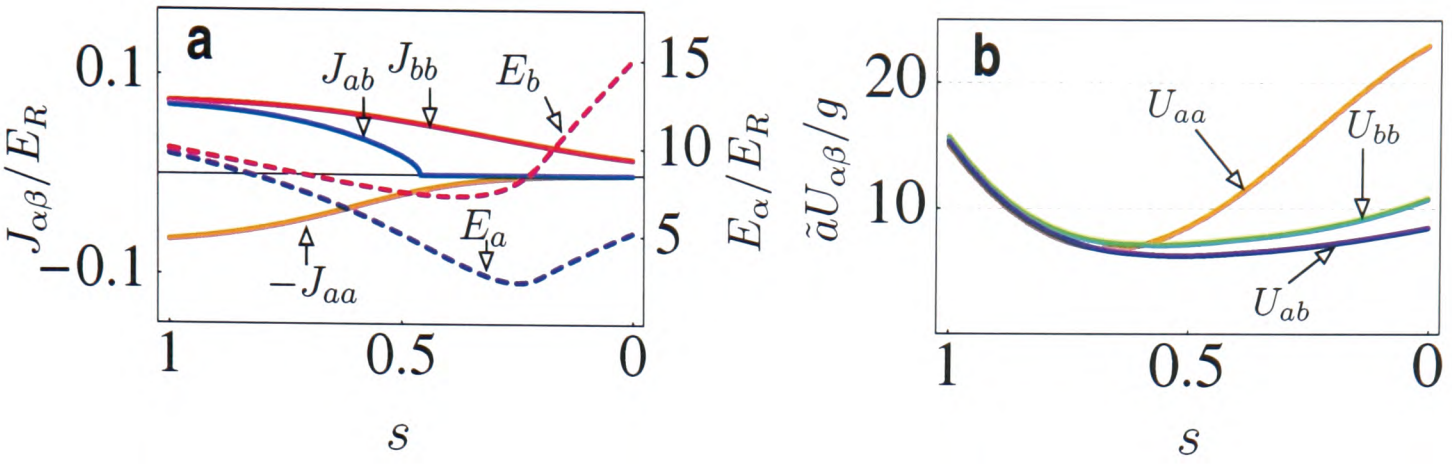


Figure 3.4. Parameters of the effective Hamiltonian $\hat{H}_{\text{eff}}$ as functions of s for a lattice depth of $V_0 = 30E_R$ and $V_T = 60E_R$ with $\tilde{a} = a\,a_T^2$. The hopping matrix elements (a) have been calculated using the method described in 3.B, while the on-site interaction energies (b) are calculated using optimised GWFs.

3.2.2 Interaction Hamiltonian

To calculate the interaction matrix elements of $\hat{H}$ the explicit form of the localised GWFs is needed. We find that for $V_0 > 10E_R$, off-site interaction terms are at least two orders of magnitude smaller than on-site interactions. We therefore only keep the dominant on-site terms and find the interaction Hamiltonian $\hat{H}_I$

$$\begin{aligned}\hat{H}_I(s) &= \sum_{i=1}^{M} \frac{U_{aa}(s)}{2}\,\hat{n}_i^a\left(\hat{n}_i^a - 1\right) + \frac{U_{bb}(s)}{2}\,\hat{n}_i^b\left(\hat{n}_i^b - 1\right) \\ &\quad + \sum_{i=1}^{M} \frac{U_{ab}(s)}{2}\left(4\hat{n}_i^a\hat{n}_i^b + \hat{b}_i^\dagger\hat{b}_i^\dagger\hat{a}_i\hat{a}_i + \hat{a}_i^\dagger\hat{a}_i^\dagger\hat{b}_i\hat{b}_i\right), \end{aligned} \tag{3.8}$$

where $\hat{n}_i^a = \hat{a}_i^\dagger\hat{a}_i$ and $\hat{n}_i^b = \hat{b}_i^\dagger\hat{b}_i$ are the site-occupation number operators. The on-site interaction matrix elements are given by

$$U_{\alpha,\beta}(s) = g\int d\mathbf{r}\, w_{\alpha,i}^*(\bar{\mathbf{r}})\, w_{\beta,i}^*(\bar{\mathbf{r}})\, w_{\alpha,i}(\bar{\mathbf{r}})\, w_{\beta,i}(\bar{\mathbf{r}}). \tag{3.9}$$

The numerical values of $U_{\alpha,\beta}$ as a function of the lattice profile s are shown in figure 3.4b. Figure 3.4b shows that their values become equal as $s \longrightarrow 1$ for sufficiently

large V_0.

Combining the single- and two-particle contributions the effective Hamiltonian describing the system dynamics is given by

$$\hat{H}_{\text{eff}}(s) = \hat{H}_0(s) + \hat{H}_I(s). \tag{3.10}$$

By using $\hat{H}_{\text{eff}}(s)$ for s varying in time we implicitly assume that the system adiabatically follows changes in the mode functions $w_{\alpha,i}$. For all dynamical calculations carried out in this work we have carefully chosen the time dependence of s so that such non-adiabatic contributions can safely be neglected.

3.2.3 Limiting cases

In the small lattice limit ($s = 1$), the superpositions $\varphi_{L,i} = (w_{a,i} - w_{b,i})/\sqrt{2}$ and $\varphi_{R,i} = (w_{a,i} + w_{b,i})/\sqrt{2}$ correspond to mode functions localised in the left and in the right well of site i respectively (see figure 3.3c and 3.3d). The associated bosonic operators are defined by

$$\hat{c}^\dagger_{L,i} = \frac{1}{\sqrt{2}}(\hat{a}^\dagger_i - \hat{b}^\dagger_i), \qquad \hat{c}^\dagger_{R,i} = \frac{1}{\sqrt{2}}(\hat{a}^\dagger_i + \hat{b}^\dagger_i). \tag{3.11}$$

Given that the new mode functions are sufficiently localised within each well, the parameters of $\hat{H}_{\text{eff}}$ for $s = 1$ can be written as

$$V_a = E - J, \quad V_b = E + J, \quad J_{\alpha,\beta} = J/2, \quad U_{\alpha,\beta} = U/2, \tag{3.12}$$

where $J = \int \mathrm{d}x\, \varphi^*_{R,i} \hat{h}_{0,x} \varphi_{L,i+1}$, $E = \int \mathrm{d}x\, \varphi^*_{L,i} \hat{h}_{0,x} \varphi_{L,i}$ and $U = g \int \mathrm{d}x\, |\varphi_{R,i}|^4$. Notice that the parameters shown in figure 3.4 are consistent with these equations. Expressing the Hamiltonian (3.10) in terms of the operators $\hat{c}^\dagger_{\alpha,i}$ ($\alpha = L, R$) and using

the parameters (3.12) we find that

$$H'_{\text{eff}} = -J \sum_{i'=1}^{2M-1} \hat{c}^{\dagger}_{i'} \hat{c}_{i'+1} + \text{h.c.} + E \sum_{i'=1}^{2M} \hat{c}^{\dagger}_{i'} \hat{c}_{i'} + \frac{U}{2} \sum_{i'=1}^{2M} \hat{c}^{\dagger}_{i'} \hat{c}^{\dagger}_{i'} \hat{c}_{i'} \hat{c}_{i'}, \tag{3.13}$$

where

$$\hat{c}^{\dagger}_{i'} = \begin{cases} \hat{c}^{\dagger}_{L,\frac{i'+1}{2}} & \text{if } i \text{ odd}, \\ \hat{c}^{\dagger}_{R,\frac{i'}{2}} & \text{if } i \text{ even}. \end{cases} \tag{3.14}$$

Therefore, as expected, $\hat{H}_{\text{eff}}(s = 1)$ is equivalent to the one-band Bose-Hubbard model (BHM) [3] with $2M$ sites.

The mode functions keep their symmetry with the two peaks moving towards the centre of the cell when s is decreased. When $s \approx 0$ is reached $w_{a,i}(x, s)$ and $w_{b,i}(x, s)$ are equivalent to the Wannier functions of the first and the second Bloch band, respectively. In this limit we obtain a standard two band Bose-Hubbard model for M sites.

3.3 Time-scale for the preparation of the quantum register

In this section we present numerical as well as analytical results characterising the ground state properties of the system and the time-scale necessary to initialise the quantum register.

3.3.1 Numerical results

The numerical calculations have been carried out using both the exact matrix representation of the Hamiltonian $\hat{H}_{\text{eff}}$ and the Time-Evolving Block Decimation (TEBD) algorithm (see 3.C for details).

We have evaluated the ground state and dynamical properties of our system for two different values of g corresponding to different interaction regimes. These values have been chosen such that in the large lattice limit (with filling factor $n = 1$) the ground state is a Mott-insulator state for g_1 and g_2 with $J_{aa}/U_{aa} < 0.3$ [85]. In the small lattice limit, g_1 and g_2 produce ground states corresponding to a strongly interacting Tonks-Girardeau (TG) gas ($U/J = 215$) and a superfluid ($U/J = 7$), respectively.

Ground states properties

In the large lattice limit, the ground state $|\psi_{0,L}\rangle$ of the system is populated exclusively by particles in the lowest Bloch band, i.e. a–mode particles. Therefore, in this limit, we only consider the one-particle density matrix given by

$$\rho^L_{ij}(\psi) = \langle\psi\,|\,\hat{a}^\dagger_i \hat{a}_j\,|\,\psi\rangle\,, \tag{3.15}$$

where $|\psi\rangle$ is the state of the system. The quasi-momentum distribution of particles in the a-mode is given by [86]

$$n^L_q(\psi) = \frac{1}{M}\sum_{i,j=1}^{M} \mathrm{e}^{-\mathrm{i}qa(i-j)}\,\rho^L_{ij}(\psi). \tag{3.16}$$

As expected, in this limit and for commensurate filling $n = 1$ the ground state is a Mott-insulator for both values of g (see figures 3.5a–d). The quasi-momentum distributions show that in this limit particles are uniformly distributed in the first band (see figures 3.5a and 3.5c).

In the small lattice limit, the one-particle density matrix is given by

$$\rho^S_{i'j'}(\psi) = \langle\psi\,|\,\hat{c}^\dagger_{i'} \hat{c}_{j'}\,|\,\psi\rangle\,, \tag{3.17}$$

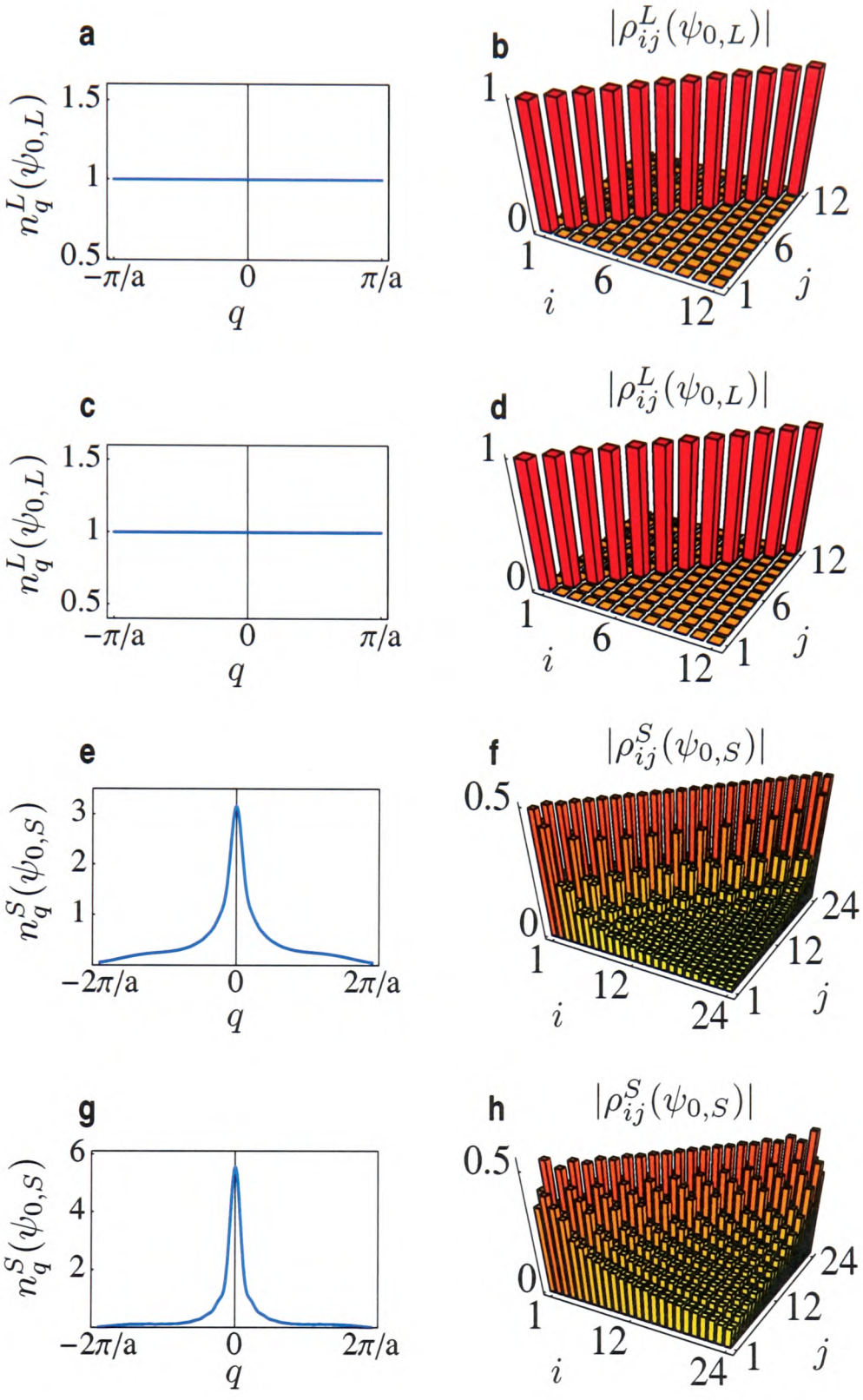


Figure 3.5. Ground state one-particle density matrix and quasi-momentum distribution for $M = 12$ lattice sites and the parameters of figure 3.4. The figures (a–d) correspond to the large lattice limit and the figures (e–h) to the small lattice limit. The quasi-momentum distribution (a), (e) and one-particle density matrix (b), (f) are for $g = g_1$. The quasi-momentum distribution (c), (g) and one-particle density matrix (d), (h) are for $g = g_2$.

where the operators $\hat{c}^\dagger_{i'}$ are constructed from the $\hat{a}^\dagger_i$ and $\hat{b}^\dagger_i$ operators using the transformations (3.11). The quasi-momentum distribution is given by

$$n^S_q(\psi) = \frac{1}{2M} \sum_{i',j'=1}^{2M} \mathrm{e}^{-\mathrm{i}q\frac{a}{2}(i'-j')}\, \rho^S_{i'j'}(\psi). \tag{3.18}$$

In this limit (with filling factor $n = 1/2$), the characteristics of the ground state $|\,\psi_{0,S}\rangle$ depend on the value of g. For $g = g_1$, the ratio $U/J = 215$ and the ground state's correlations as well as the quasi-momentum distributions (see figures 3.5e–f) are characteristic of a TG gas (see e.g. [87] and references therein). The value $g = g_2$ yields the ratio $U/J = 7$ and the system exhibits the behaviour of a superfluid (see figures 3.5g–h), with particles occupying mainly the $q = 0$ momentum state. Notice that one-dimensional systems described by the BHM with a fixed filling factor $n = 1$ cross the MI-SF phase boundary at the critical point $(J/U)_c \approx 0.3$ [85]. Thus, in our case the superfluid behaviour of the system in the small lattice limit is due to the fractional filling of the lattice.

Simulation of the dynamics

Starting from a system with half-filling and a lattice profile $s = 1$, we investigate the time-scale required to obtain a nearly perfect MI state—or quantum register—with filling factor $n = 1$ by ramping the lattice profile down to $s = 0$. The quality of the register is determined by the fidelity

$$F = |\langle\, \psi \,|\, \psi_{0,L} \,\rangle|^2\,, \tag{3.19}$$

defined as the overlap between the state of the system $|\,\psi\rangle$ at the end of the ramping process and the ground state in the large lattice limit $|\,\psi_{0,L}\rangle$. Furthermore, we

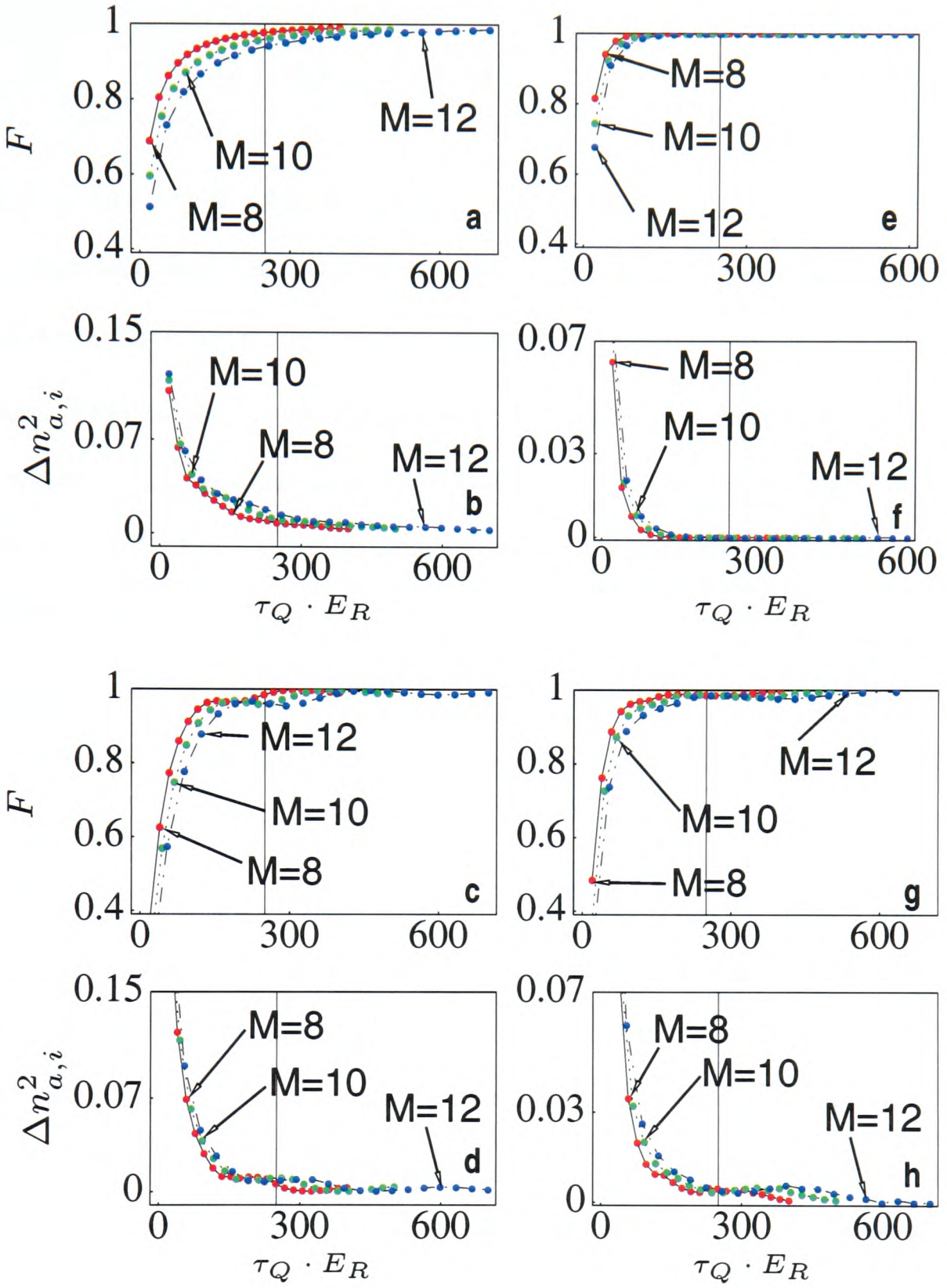


Figure 3.6. Dynamical simulation of $\hat{H}_{\text{eff}}$ using the parameters shown in figure 3.4 for two different values of g. The ramping strategies s_{gap} and s_{man} are shown in figure 3.7a. Simulation results for the fidelity and particle-number fluctuations using: (a–b) a linear ramp and $g = g_1$; (c–d) a linear ramp and $g = g_2$; (e–f) the ramp s_{gap} and $g = g_1$; (g–h) the ramp s_{man} and $g = g_2$. The vertical lines indicate the value of the particle tunneling time ($t_{\text{tun}} \sim 1/J_{aa}$) in the large lattice limit.

calculate the fluctuations of the number of particles in the a-mode at site i

$$\Delta n_{a,i} = \sqrt{\langle (\hat{n}_i^a)^2 \rangle - \langle \hat{n}_i^a \rangle^2}, \tag{3.20}$$

where $\langle \circ \rangle = \langle \psi \,|\, \circ \,|\, \psi \rangle$. Since particle-number fluctuations are suppressed in a MI state, non-zero fluctuations indicate the presence of excitations, such as double occupancies or particles in the second band, in the final state.

We test different ramps by simulating the system dynamics between $t_\mathrm{i} = 0$ to $t_\mathrm{f} = \tau_Q$ where τ_Q is the ramping time (the time required to complete the ramping process from $s = 1$ to $s = 0$). Here, each ramp σ corresponds to a function $s = s_\sigma(t)$ varying from $s_\sigma(0) = 1$ to $s_\sigma(\tau_Q) = 0$.

For linear ramping we use $s_\mathrm{lin}(t) = (\tau_Q - t/E_R)/\tau_Q$. The fidelity and particle-number fluctuations obtained using this strategy for different quench times and $g = g_1$ and $g = g_2$ are shown in figures 3.6a–d. The linear ramp is shown in figure 3.7a.

Another ramping strategy we use consists of adapting the velocity of the ramp proportionally to the energy gap between the ground and the first excited state. This ramp is denoted by $s_\mathrm{gap}(t)$. We evaluate the ramp function $s_\mathrm{gap}(t)$ numerically (see 3.D) for a system with $M = 4$ sites and $V_0 = 30E_R$. The ramp $s_\mathrm{gap}(t)$ for $g = g_1$ is shown in figure 3.7a. We expect this ramping strategy to be more efficient than the linear one, since accelerating the ramp when the gap is large while slowing it down when the gap is small should suppress transitions of particles to excited levels. Our numerical calculations have shown that when $g = g_1$, the utilisation of this ramp does indeed reduce the quench time needed to obtain a nearly perfect fidelity to a half of the tunneling time in the large lattice limit (see figure 3.6e–f). For $g = g_2$, we find that compared to $s_\mathrm{lin}(t)$, this strategy only marginally improves the fidelity.

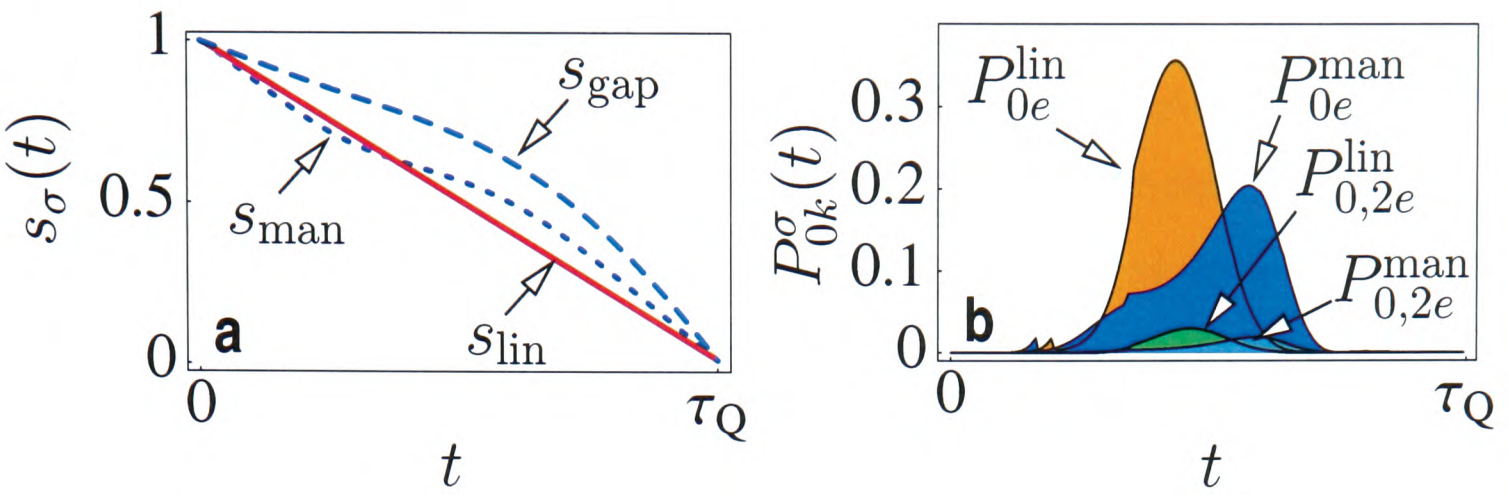


Figure 3.7. (a) Different ramps used in our numerical calculations. (b) Transition probability between the ground and the first (labeled by e) and second (labeled by $2e$) excited states as a function of time for the ramps $s_{\rm lin}$ and $s_{\rm man}$. The transition probabilities have been calculated via the exact diagonalisation of $\hat{H}_{\rm eff}$ for $M = 4$ and a quench time of $\tau_Q = 20/E_R$.

In order to reduce the time required to obtain a given fidelity for $g = g_2$, a more sophisticated ramping strategy is needed. In the following, we provide a simple method to estimate the efficiency of different ramps without running a complete dynamical simulation of the system. The transition probability between the ground and some excited state $|\,k\rangle$ at time t for a ramp σ is approximately given by [88]

$$P^\sigma_{0k}(t) \approx \frac{2}{\omega^2_{0k}} \left| \langle 0 \,|\, \frac{\mathrm{d}}{\mathrm{d}t} \,|\, k \rangle \right|^2 [1 - \cos(\omega_{0k} t)]\,, \tag{3.21}$$

where $|\,k\rangle = |\,k(\sigma, t)\rangle$ is the k-th instantaneous eigenstate[3] of $\hat{H}_{\rm eff}(s_\sigma(t))$ and ω_{0k} is the transition frequency between the ground state and $|\,k\rangle$. Therefore, the assessment of the efficiency of a ramp can be done by evaluating the functional

$$A(\sigma, \tau_Q) = \frac{1}{\tau_Q} \sum_k \int_0^{\tau_Q} \mathrm{d}t\, P^\sigma_{0k}(t), \tag{3.22}$$

where the index k runs over all the values associated with levels connected to the

[3]Note that neglecting non-adiabatic changes of the GWFs does not correspond to $P^\sigma_{0k}(t) = 0$ at all times.

ground state. The functional $A(\sigma, \tau_Q)$ corresponds to the average transition probability per unit time for a given strategy σ and quench time τ_Q. We calculate the value of the functional $A(\sigma, \tau_Q)$ numerically via exact diagonalisation of $\hat{H}_{\text{eff}}$ for a small system. This method allows to optimise ramps by minimising the value of $A(\sigma, \tau_Q)$. The optimised ramp for a small system is then used in the simulation of larger systems. For instance, the strategy $s_{\text{man}}(t)$ shown in figure 3.7a was designed and optimised manually using this method. For $g = g_2$, we find that $A(\text{lin}, \tau_Q)/A(\text{man}, \tau_Q) \approx 2.3$ for $\tau_Q = 20/E_R$ (see figure 3.7b), thus showing the better efficiency of the strategy $s_{\text{man}}(t)$ compared to $s_{\text{lin}}(t)$. As shown in figure 3.6, dynamical simulations of the system with $g = g_2$ confirm that this strategy reduces the time required to obtain a given fidelity.

For systems initially in the superfluid regime ($g = g_2$), the fidelity curves exhibit small oscillations (see figure 3.6e). These can be understood from time-dependent perturbation theory as oscillations occurring when some of the frequencies involved in the Fourier decomposition of the perturbation Hamiltonian enter into resonance with system frequencies. This is expected since superfluids have a dense spectrum at low energies and are therefore likely to enter into resonance with one of the frequencies of the perturbation Hamiltonian [89]. Hence, the amplitude of the oscillations in the fidelity curve associated with a ramping strategy $s_1(t)$ should be smaller than those associated with a ramping strategy $s_2(t)$ if $A(1, \tau_Q) < A(2, \tau_Q)$ for all τ_Q. This is what is observed from our numerical simulations (see figures 3.6f-h).

The quasi-momentum distribution of the particles in the a–mode at the end of the different ramping processes for a system with $g = g_1$ are shown in figure 3.8. For the linear ramp, the quasi-momentum distribution of particles shown in figure 3.8a does not correspond to that of a MI state for the quench times considered. In contrast, for the ramp s_{gap} the quasi-momentum distribution becomes approximately flat for quench times of $\tau_Q > 200/E_R$. Even for the fastest ramps, we find that the

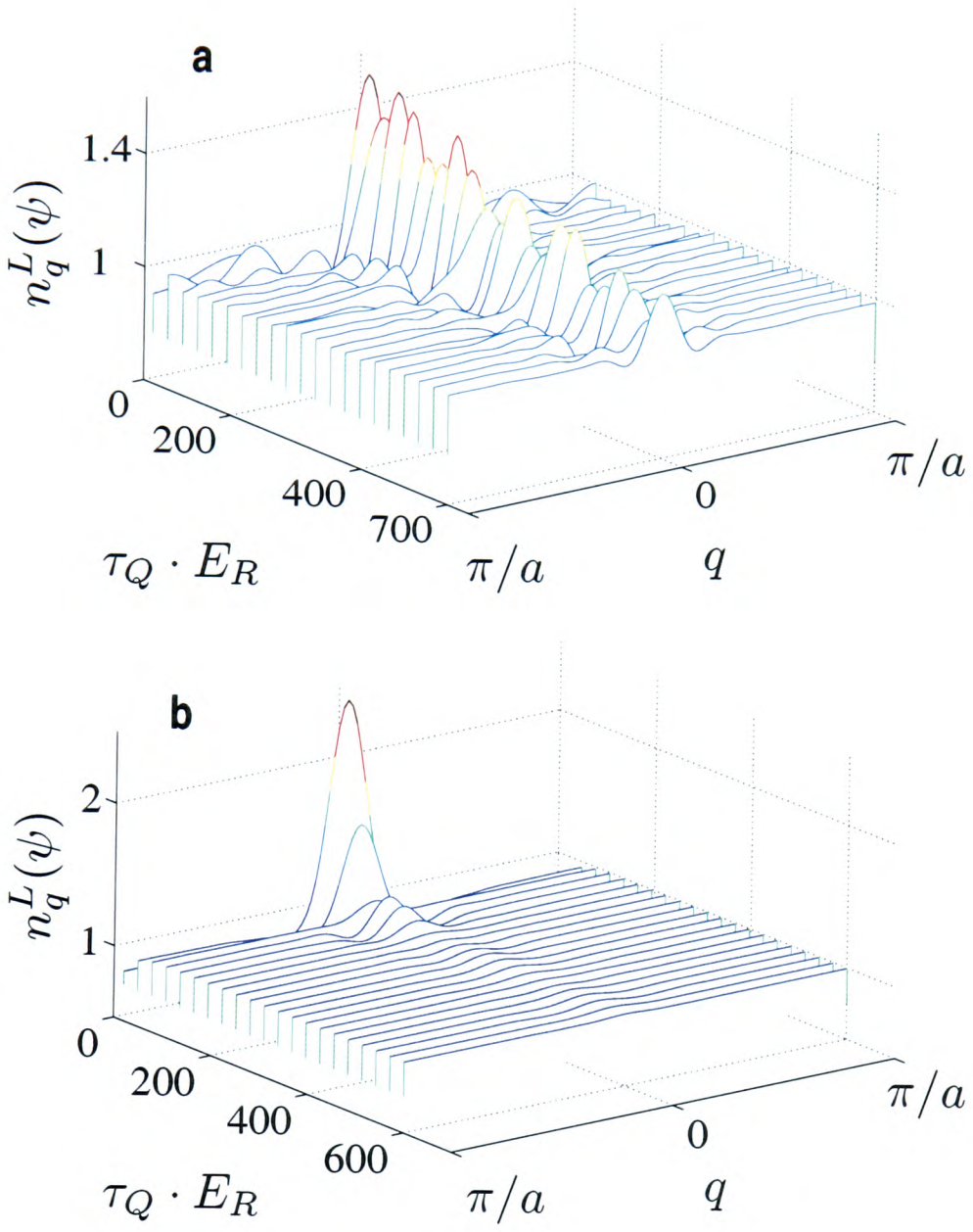


Figure 3.8. The quasi-momentum distributions at the end of a ramp for a system of $M = 12$ sites using the parameters shown in figure 3.4 for $g = g_1$. (a) s_{lin}; (b) s_{gap} .

occupation of the b–mode is less than 2% of the total number of particles. Thus, the experimental measure of the register fidelity can be made by comparing the quasi-momentum distribution of particles in the final state with, e.g. that shown in figure 3.5c.

Discussion of the numerical results

In the BHM with $U/J \ll 1$, the tunneling time $1/J$ determines the adiabatic time-scale of the system. However, as soon as many-body interactions are sufficiently large, this time-scale often becomes very non-adiabatic [90]. The main observation that can be drawn from the numerical calculations presented in the last section is that by preparing the system in a TG state ($g = g_1$), and using an efficient ramping strategy, it is possible to initialise a very deep MI state on a time scale equivalent to half the tunneling time in the large lattice limit (see figure 3.6b). The time required to initialise a MI state with unit filling as well as a TG state with half filling is approximately ten times the tunneling time of the final system [80, 81, 90, 91]. Since the tunneling time in the large lattice limit is two orders of magnitude larger than in the small lattice limit, the total time required to initialise a MI state using our procedure is an order of magnitude faster than the direct quantum freezing method. In this estimation we assume that the initial BEC has zero temperature, i.e., we do not take the effect of defects present in the initial state into account.

The experimental realisation of initial states with $g = g_1$ and $g = g_2$ can be achieved using Feshbach resonances. For a magnetic Feshbach resonance fluctuations in the magnetic field result in fluctuations of the size of the gap between the ground and the first excited state which will affect the performance of our scheme. For instance, in the case $g = g_1$ magnetic field fluctuations of 10 mG will change the gap by approximately 0.5% for ^{85}Rb or ^{133}Cs atoms [42, 92]. We assume adiabatic evolution of the system and thus these fluctuations will have negligible repercussions

on the fidelity of the final state. To realise the superfluid regime with $g = g_2$ very stable magnetic fields are required. Magnetic field fluctuations of e.g. 1 mG will lead to gap fluctuations of approximately 1% in ^{23}Na and ^{85}Rb. We finally remark that our scheme could also be used without employing a Feshbach resonance. This case corresponds to an intermediate value of g between g_1 and g_2. While a detailed analysis of the intermediate regime is beyond the scope of the present work we do not expect qualitative differences compared to the interaction strengths considered here.

3.3.2 Analytical results

In this section we derive an approximate expression for the quench time required to obtain a given fidelity in the case of a linear ramp.

The energy spectrum of systems in the TG and superfluid regime is gapless [4](see e.g. [37]), while in the Mott-insulating regime, the gap between the ground and first excited state is proportional to the on-site interaction energy [89]. Since the relaxation time $\tau(t)$ of the system—the time required by the system to adjust to a change of parameters at time t—is inversely proportional to the gap between the ground and the first excited state, the relaxation time in the small lattice limit is large, while it is small and finite in the large lattice limit. This observation suggests that the *adiabatic-impulse* (AI) assumption from Kibble-Zurek (KZ) theory can be used to evaluate the adiabaticity of a ramp with respect to the quench time [93–95].

The AI approximation is based on the following considerations: (i) When the gap between the ground and the first excited state is large, the relaxation time of the system is short and thus a system starting its evolution in the ground state remains in the ground state, i.e. its evolution is *adiabatic*. (ii) When the gap between the ground and the first excited state is small, the system's relaxation time is large and

[4]In finite size systems, the spectrum is not gapless, only very dense.

the system no longer adapts to changes of the Hamiltonian's parameters and its state becomes effectively frozen. The system is then in the *impulse regime*. The instant $\hat{t}$ at which the system passes from the impulse to the adiabatic regime, and inversely, is defined by the equation [93, 94, 96]

$$\tau(\hat{t}) = \alpha\hat{t}, \tag{3.23}$$

where $\alpha = \mathcal{O}(1)$ is a constant. Note that $\hat{t}$ is a time and not an operator. In the AI approximation, the time-evolution of the system is either adiabatic or impulse. Thus, the *density of defects* $\mathscr{D}$, which corresponds to the density of excitations caused by a change of parameters which drive the system from the impulse to the adiabatic regime can be approximated by [94]

$$\mathscr{D} \simeq \left| \left\langle \Psi_e(\hat{t}) \,|\, \Psi_g(0) \right\rangle \right|^2, \tag{3.24}$$

where $|\,\Psi_g(0)\rangle$ and $\left|\,\Psi_e(\hat{t})\right\rangle$ are the ground and first excited states at the initial time $t = 0$ and at time $t = \hat{t}$, respectively. Hence, without solving the time-dependent Schrödinger equation it is possible to make predictions for the density of defects (3.24) resulting from a given dynamical process.

In order to apply the KZ theory to our problem, we develop an effective model describing the system dynamics. A similar model was recently examined by Cucchietti *et al.* [95]. We find from numerical calculations (see figure 3.7b) that most of the excitations created in the system are caused by transitions from the ground to the first excited state. Furthermore, we examined the form of the eigenvectors of the Hamiltonian (3.10) in both limits for different system sizes via exact diagonalisation. This revealed that both the ground state and the first accessible excited state can be approximated by an expansion in only two basis states. The elements

of this reduced basis set are given by

$$|1\rangle = \bigotimes_{i=1}^{M} |1\rangle_i \,, \tag{3.25}$$

$$\begin{aligned} |2\rangle = (&|2;0;1;\cdots;1\rangle + |2;1;0;1;\cdots;1\rangle + |2;1;1;0;1;\cdots;1\rangle \\ &+ |1;2;1;0;1;\cdots;1\rangle + \cdots)/\sqrt{M(M-1)}, \end{aligned} \tag{3.26}$$

where, e.g.

$$|2;0;1;\cdots;1\rangle = |2\rangle_1 \otimes |0\rangle_2 \otimes |1\rangle_3 \otimes \cdots \otimes |1\rangle_M$$

with $|n\rangle_i = (1/\sqrt{n!})(\hat{a}_i^\dagger)^n |\,\mathrm{vac}\rangle$. The basis state $|2\rangle$ corresponds to a superposition of all possible states of a system of M particles in the a-modes with $(M-2)$ singly occupied sites, one doubly occupied site, and one empty site. In the limit $M \to \infty$, the matrix representation $\hat{H}_R$ of Hamiltonian (3.10) in the reduced basis $\{|1\rangle, |2\rangle\}$ reads, up to a constant energy V_a

$$\hat{H}_R = \begin{pmatrix} 0 & \sqrt{2}\, J_{aa}(t) \\ \sqrt{2}\, J_{aa}(t) & U_{aa}(t) \end{pmatrix}. \tag{3.27}$$

The instantaneous eigenstates of equation (3.27) associated with the energies of the ground and first excited levels are given by

$$|g(t)\rangle = -\sin(\theta(t)/2)\,|1\rangle + \cos(\theta(t)/2)\,|2\rangle\,, \text{ and} \tag{3.28}$$

$$|e(t)\rangle = \cos(\theta(t)/2)\,|1\rangle + \sin(\theta(t)/2)\,|2\rangle\,, \tag{3.29}$$

respectively, with $\cos(\theta(t)) = -U_{aa}(t)/[U_{aa}(t)^2 + 8J_{aa}(t)^2]^{\frac{1}{2}}$, $\theta \in [0, \pi]$. Furthermore, we approximate the parameters J_{aa} and U_{aa} as linear functions of time

$$J_{aa}(t) = \Delta J_{aa}(\tau_Q - t)/\tau_Q \tag{3.30}$$

$$U_{aa}(t) = U_{\text{init}} + \Delta U_{aa} t/\tau_Q \tag{3.31}$$

where $\Delta J_{aa} = |J_{aa}(s=1) - J_{aa}(s=0)|$, $\Delta U_{aa} = |U_{\text{init}} - U_{aa}(s=0)|$ and $U_{\text{init}} = \min[U_{aa}]$.

We further simplify the Hamiltonian $\hat{H}_R$ by replacing the hopping term $J_{aa}(t)$ by its time average. Setting $J_{aa}(t) = \bar{J}_{aa}$ with $\bar{J}_{aa} = (1/\tau_Q)\int_0^{\tau_Q} \mathrm{d}t\, J_{aa}(t)$ and rescaling the time as $t \longrightarrow t' - (U_{\text{init}}\tau_Q/\Delta U_{aa})$ yields the transformation

$$\hat{H}_R \longrightarrow \hat{H}_R = \begin{pmatrix} 0 & \sqrt{2}\,\bar{J}_{aa} \\ \sqrt{2}\,\bar{J}_{aa} & \Delta U_{aa} t'/\tau_Q \end{pmatrix}, \tag{3.32}$$

which turns $\hat{H}_R$ into the Landau-Zener form $\hat{H}_R = \hat{A}t' + \hat{B}$, where $\hat{A}$ and $\hat{B}$ are Hermitian matrices and $\hat{A}$ is diagonal [97–99]. The energy spectrum of the Hamiltonian (3.32) reproduces approximately the features of the spectrum of $\hat{H}_{\text{eff}}$ except that the gap is overestimated in the small lattice limit.

Starting at $t = 0$ in the small lattice limit where the system is impulse, we use the AI approximation to derive the density of defects at the end of a linear ramp which drives the system to the large lattice limit, where the system is adiabatic. Defining the relaxation time as the inverse of the energy gap $1/\Delta E$ between the levels of $\hat{H}_R$, with $\Delta E = [(\Delta U_{aa} t/\tau_Q)^2 + (2\sqrt{2}\bar{J}_{aa})^2]^{\frac{1}{2}}$, equation (3.23) can be solved analytically and the instant $\hat{t}$ at which our system exits the impulse regime is given by

$$\hat{t} = \sqrt{\frac{\tau_Q}{\Delta U_{aa}}}\sqrt{\sqrt{\frac{1}{\alpha} + (\eta\tau_Q)^2} - \eta\tau_Q}, \tag{3.33}$$

where $\eta = 4\bar{J}_{aa}^2/\Delta U_{aa}$. We evaluate the density of defects $\mathscr{D}$ using equation (3.24) with $|\Psi_g(t_i)\rangle = |g(0)\rangle$ and $|\Psi_e(\hat{t})\rangle = |e(\hat{t})\rangle$. In order to simplify the expression

number of defects is approximately measured by the operator

$$\hat{K} = \sum_{i=1}^{M} \hat{n}_i^a(\hat{n}_i^a - 1). \tag{3.36}$$

Hence, the density of defects is given by $\mathscr{D} = \langle \hat{K} \rangle / M = \langle (\hat{n}_i^a)^2 \rangle - \langle \hat{n}_i^a \rangle$. Numerical calculations show that the density of defects $\mathscr{D}$ has the same scaling behaviour as $\Delta n_{a,i}^2$. A comparison between equation (3.34) and the numerical values of the density of defects in the large lattice limit for different values of the ramping time τ_Q is shown in figure 3.9. For $M = 12$ particles and $g = g_2$, we find that the analytical formula for $\mathscr{D}$ fits the numerical data well for $\alpha = 1.41$. For $g = g_1$ the fit is less accurate. This is expected since for this value of g, the system has a less distinct separation between the adiabatic and impulse regime than for $g = g_2$. For the number of particles we have been able to simulate, the fit improves as we increase the number of particles for both values of g. In addition to this, we see from equation (3.35) that the time required to initialise a register with a given fidelity—and thus the adiabatic time for small $\mathscr{D}$—scales with the ratio $\Delta U_{aa}/\bar{J}_{aa}^2$.

3.4 Conclusion

We have shown that the dynamics of an optical lattice whose periodicity is doubled via superlattice potentials is very well described by a two-mode Hubbard-like Hamiltonian. The parameters of this Hamiltonian have been evaluated in the tight binding approximation using optimally localised GWFs. The doubling of the period removes half of the lattice sites and doubles the filling factor. We have shown that this doubling can be used for the fast initialisation of a quantum register. By starting from a half filled lattice in the small lattice limit filled by either a TG ($g = g_1$) gas or a superfluid ($g = g_2$), a commensurate MI state corresponding to an atomic

quantum register can obtained on timescales shorter than those achieved by direct quantum freezing of a superfluid with same lattice spacing. Furthermore, we derived an analytical expression for the density of defects as a function of the quench time for linear ramping of the superlattice. We found that the time required to achieve a given density of defects is proportional to the ratio $\Delta U_{aa}/\bar{J}_{aa}^2$.

Our numerical calculations of ground state properties suggest that doubling the lattice period drives the system through a quantum phase transition for large lattices $M \to \infty$. The eventual abrupt change in the ground state properties might be observable by time-of-flight measurements. An investigation of whether such a quantum phase transition indeed exists is beyond the scope of the current work but will be investigated in future work.

In this work we concentrated on the transition from filling factor $n = 1/2$ to $n = 1$. We finally note that the idea developed in this paper may be extended by considering lattices with an initial filling factor of $n = 1/2^\ell$ (where ℓ is an integer). Subsequently removing every second barrier will create a lattice with period $2a$ and filling factor $1/2^{\ell-1}$. This procedure could be repeated ℓ times providing a lattice with filling factor $n = 1$ and large lattice spacing $2^\ell a$.

Acknowledgements

This work was supported by the EU through the STREP project OLAQUI and a Marie Curie Intra-European Fellowship within the 6th European Community Framework Programme. The research was also supported by the EPSRC (UK) through the QIP IRC (GR/S82716/01) and project EP/C51933/01. DJ thanks the Beijing International Center for Mathematical Research at Peking University for hospitality while carrying out parts of this work.

Appendix

3.A Definition and localisation properties of GWFs

In the TB limit, the effective single particle Hamiltonian of our system in momentum space (in the basis $|\alpha\rangle_q = [(1/\sqrt{M})\sum_{i=1}^{M} \mathrm{e}^{\mathrm{i}qai}\hat{\alpha}_i^\dagger]\,|0\rangle$ with $\alpha = a, b$) can be written as

$$\hat{H}_{0,q} = \sum_{\mu=-1,0,1} \hat{\varepsilon}(\mu)\,\mathrm{e}^{-\mathrm{i}a\mu q}. \tag{3.37}$$

The elements of the matrices $\hat{\varepsilon}(\mu)$ are given by [100]

$$\varepsilon_{\alpha\beta}(\mu) = \langle w_{\alpha,i}\,|\,\hat{h}_{0,x}\,|\,w_{\beta,i+\mu}\rangle\,. \tag{3.38}$$

For $\mu = 0$ and $\mu = 1$, the elements of the matrices $\hat{\varepsilon}(\mu)$ correspond to the local site energy and hopping matrix elements between neighbouring sites, respectively. For the TB approximation to be accurate, we need the eigenvalues $E_{\alpha,q}$ of $\hat{H}_{0,q}$ to reproduce very closely the band structure of the exact single particle Hamiltonian $\hat{h}_{0,x}$ for all values of the lattice profile s. If we were to use WFs as mode functions $w_{\alpha,i}$, the matrices $\hat{\varepsilon}$ would be diagonal [59] and the dispersion relations of the two Bloch bands sinusoidal. In order to obtain a more accurate description, we use GWFs as mode functions. The definition of GWFs is given by

$$w_{\alpha,i}(x,s) = \sqrt{\frac{a}{2\pi}}\int_{-\frac{\pi}{a}}^{\frac{\pi}{a}} \mathrm{d}q\,\mathrm{e}^{-\mathrm{i}qR_i}\,\tilde{\Psi}_{\alpha,q}(x,s), \tag{3.39}$$

where $\tilde{\Psi}_{\alpha,q} = \sum_{\beta=a,b} U^{(q)*}_{\beta,\alpha}\,\Psi_{\beta,q}$ is called the *generalised-Bloch orbital* with $\Psi_{\alpha,q}$ the Bloch function associated with the band α and R_i is the centre of site i [66, 71]. The rows of the 2×2 matrix $U^{(q)}$ contain the normalised eigenvectors of $\hat{H}_{0,q}$ associated with the eigenvalues $E_{\alpha,q}$, that is $\sum_{\mu=a,b}(\hat{H}_{0,q})_{n,\mu}U^{(q)}_{\alpha,\mu} = E_{\alpha,q}U^{(k)}_{\alpha,n}$ [100]. Inserting

GWFs in equation (3.38), we recover the elements $\varepsilon_{\alpha\beta}(\mu)$ and, hence, GWFs correspond to the mode functions associated with the effective Hamiltonian $\hat{H}_{0,q}$ [100]. Notice that the definition of GWFs reduces to that of WFs for $U^{(q)} = \mathbb{1}$.

Localisation properties of GWFs

Given a valid set of GWFs, another equally valid set of GWFs can be obtained by applying the following transformation on the $U^{(q)}$ matrices

$$U^{(q)} \rightarrow \begin{pmatrix} \mathrm{e}^{\mathrm{i}\phi_a(q)} & 0 \\ 0 & \mathrm{e}^{\mathrm{i}\phi_b(q)} \end{pmatrix} U^{(q)}, \tag{3.40}$$

where $\phi_\alpha(q)$ are (real) functions of q which can be chosen freely as long as they do not introduce discontinuities in the generalised Bloch function [65]. The gauge transformation (3.40) is equivalent to re-phasing each Bloch function as $\Psi_{\alpha,q} \rightarrow \mathrm{e}^{\mathrm{i}\phi_\alpha(q)}\Psi_{\alpha,q}$. Notice that gauge transformations do not affect the value of the parameters V_α and $J_{\alpha,\beta}$ calculated using the relations (3.7) and (3.6), respectively, but they alter the localisation properties—the spread—of the GWFs. Following the convention suggested by Blount [65], we set the phase functions $\phi_\alpha(q)$ in a manner that leads to maximally localised GWFs. That is, we choose the phase functions such that the resulting GWFs minimise the spread functional

$$\Omega = \sum_\alpha \langle x^2 \rangle_\alpha - \langle x \rangle_\alpha^2, \tag{3.41}$$

where in our case $\alpha = a, b$ while $\langle x^2 \rangle_\alpha = \langle w_{\alpha,i} \,|\, x^2 \,|\, w_{\alpha,i} \rangle$ and $\langle x \rangle_\alpha = \langle w_{\alpha,i} \,|\, x \,|\, w_{\alpha,i} \rangle$ correspond to the centre of a GWF and its second moment, respectively.

Expanding $\tilde{u}_{\alpha,q}(x,s) = \mathrm{e}^{-\mathrm{i}qx}\tilde{\Psi}_{\alpha,q}(x,s)$ into plane waves yields

$$\tilde{u}_{\alpha,q}(x,s) = \sum_j G_{\alpha,j}(q,s)\,\mathrm{e}^{\mathrm{i}K_j x}, \tag{3.42}$$

where $K_j = 2\pi j/L$ with $L = Ma$. Invoking the translational symmetry of the lattice and the convolution theorem [65], the value of the functional Ω is minimised when the expansion coefficients $G_{\alpha,j}(q,s)$ are chosen real, which is always possible when the lattice possesses mirror symmetry [100]. This is equivalent to the choice of purely real GWFs for even generalised-Bloch functions and purely imaginary ones for odd generalised-Bloch functions. Notice that this conclusion is in agreement with a conjecture of Marzari *et al.* [66] on the real nature (up to a global phase) of maximally localised WFs.

We have numerically evaluated the phases $\phi_\alpha(q)$ using the algorithm described in [66] for the special case of 1D WFs. This procedure minimised the functional Ω in the limit of very fine sampling of the q-space. The effect of this localisation procedure is illustrated in figure 3.3a.

3.B Parameters of the single-particle Hamiltonian

We diagonalise $\hat{H}_0$ in momentum space for periodic boundary conditions. Using the Fourier transformations $\hat{a}_i = (1/\sqrt{M})\sum_q \mathrm{e}^{\mathrm{i}qai}\hat{a}_q$ and $\hat{b}_i = (1/\sqrt{M})\sum_q \mathrm{e}^{\mathrm{i}qai}\hat{b}_q$, $\hat{H}_0$ becomes block diagonal

$$\hat{H}_0 = \sum_q \hat{H}_{0,q}, \tag{3.43}$$

where $q = 2\pi\nu/Ma$, $\nu = 1 \ldots M$. In the basis $\left\{ |\, a\rangle_q \,, |\, b\rangle_q \right\}$, the operator $\hat{H}_{0,q}$ reads

$$\hat{H}_{0,q} = \begin{pmatrix} V_a - 2J_{aa}\,\cos qa & -\mathrm{i}2J_{ab}\,\sin qa \\ \mathrm{i}2J_{ab}\,\sin qa & V_b + 2J_{bb}\,\cos qa \end{pmatrix}, \tag{3.44}$$

with $|\, a\rangle_q = \hat{a}_q^\dagger\,|\,0\rangle$ and $|\, b\rangle_q = \hat{b}_q^\dagger\,|\,0\rangle$. For simplicity, the explicit dependence of the parameters on the lattice profile has been dropped.

Due to the periodicity of the lattice, the eigenvalues of $\hat{H}_{0,q}$ exhibit a band structure. By choosing the points $q = 0,\ \pi/a,\ \pi/2a$ in the Brillouin zone, we derive and solve a set of equations for the parameters V_α and $J_{\alpha,\beta}$ as functions of the eigenvalues $E_{\alpha,q}$ of $\hat{H}_{0,q}$

$$J_{aa} = \frac{E_{a,\pi} - E_{a,0}}{4} \quad , \quad J_{bb} = \frac{E_{b,0} - E_{b,\pi}}{4}, \tag{3.45}$$

$$V_a = \frac{E_{a,0} + E_{a,\pi}}{2} \quad , \quad V_b = \frac{E_{b,0} + E_{b,\pi}}{2}, \tag{3.46}$$

$$J_{ab} = \frac{1}{4}\left[(E_{b,\frac{\pi}{2}} - E_{a,\frac{\pi}{2}})^2 - (V_a - V_b)^2 \right]^{\frac{1}{2}}. \tag{3.47}$$

For the eigenvalues of $\hat{H}_{0,q}$ to reproduce the band structure of the exact single-particle Hamiltonian along the x–direction $\hat{h}_{0,x}$, we evaluate the parameters V_α and $J_{\alpha,\beta}$ using the eigenvalues $\varepsilon_{\alpha,q}$ of $\hat{h}_{0,x}$ obtained via exact numerical diagonalisation for the same points in the Brillouin zone (see figure 3.2). The numerical values of the parameters obtained via this procedure are shown in figure 3.4a.

The accuracy of the TB approximation can be tested by evaluating the standard deviation between the exact and approximated band structure. That is, taking N_q different points q_i on each band, we define the standard deviation between the exact and approximate band structure for a given lattice profile by $\sigma_s^2 = (1/2N_q)\sum_{i=1}^{N_q}(\Delta\varepsilon_{a,q_i}^2 + \Delta\varepsilon_{b,q_i}^2)$, with $\Delta\varepsilon_{\alpha,q_i} = \varepsilon_{\alpha,q_i} - E_{\alpha,q_i}$. Averaging over N_s different lattice profiles s_i, we obtain $\langle\sigma\rangle_s = [(1/N_s)\sum_{i=1}^{N_s}\sigma_{s_i}^2]^{\frac{1}{2}} = 3.4\times10^{-2}E_R$

for a lattice depth of $V_0 = 10\,E_R$. This excellent agreement improves further as we increase the value of V_0, and hence fully justifies the tight-binding approximation.

3.C Dynamical and ground state calculations using the TEBD algorithm

The TEBD algorithm is based on directly manipulating a matrix product representation of the many-body wave function. Here, we shall briefly describe the key aspects of this algorithm and refer the reader to some of the recent literature [101–104] for more detail.

An arbitrary state of a 1D quantum lattice system composed of M sites can be written as

$$|\,\psi\rangle = \sum_{j_1=1}^{\mathrm{d}} \cdots \sum_{j_M=1}^{\mathrm{d}} c_{j_1 \cdots j_M}\,|\,j_1, \ldots, j_M\rangle\,,$$

where $c_{j_1 \cdots j_M}$ is a set of d^M complex amplitudes and $|\,j_m\rangle$ is a basis spanning the local d-dimensional Hilbert space of site m. Within time-dependent DMRG the amplitudes $c_{j_1 \cdots j_M}$ are constructed from a product of tensors

$$c_{j_1 j_2 \cdots j_M} = \sum_{\{\alpha\}=1}^{\{\chi\}} \Gamma^{[1]j_1}_{\alpha_1} \lambda^{[1]}_{\alpha_1} \Gamma^{[2]j_2}_{\alpha_1 \alpha_2} \lambda^{[2]}_{\alpha_2} \cdots \Gamma^{[M]j_M}_{\alpha_{M-1}}, \tag{3.48}$$

where $\{\alpha\} = \{\alpha_1, \cdots, \alpha_{M-1}\}$, $\{\chi\} = \{\chi_1, \cdots, \chi_{M-1}\}$ and with Γ and λ tensors chosen to be constructed from the set of $M-1$ Schmidt decompositions for contiguous partitions of the system. Specifically, the elements of $\lambda^{[m]}_{\alpha}$ are taken to be Schmidt coefficients of the bipartite splitting after site m in $|\,\psi\rangle = \sum_{\alpha=1}^{\chi_m} \lambda^{[m]}_{\alpha}\,|\,L^m_\alpha\rangle\,|\,R^m_\alpha\rangle$ with Schmidt rank χ_m. The Schmidt states $|\,L^m_\alpha\rangle$ and $|\,R^m_\alpha\rangle$ spanning the left $\{1, \cdots, m\}$ and right $\{m+1, \cdots, M\}$ subsystems of sites respectively are then specified by the corresponding sums remaining in equation (3.48).

The usefulness of this representation is based on the observation that for 1D systems with a Hamiltonian composed of nearest neighbour terms the ground state and low-lying excited states have Schmidt coefficients $\lambda_\alpha^{[m]}$ which rapidly decay with α when arranged in descending order. Consequently, rather than allowing the Schmidt ranks χ_m to grow to their maximum permissible value a much smaller fixed upper-limit χ can be imposed truncating the representation while still providing a near unit overlap with the exact state $|\psi\rangle$. Fixing the Schmidt ranks results in the number of parameters scaling as $O(\mathrm{d}\chi^2 M)$ and so curtails the possible exponential growth with M seen for general coefficients $c_{j_1 \cdots j_M}$.

The matrix product representation also permits the efficient update of the state after the action of a unitary operator on any two neighbouring lattice sites. This proceeds by modifying the Γ tensors associated to the sites and the λ tensor linking them and requiring a number of operations which scales as $O(\mathrm{d}^4\chi^3)$. The resulting tensors are then systematically truncated back to a maximum rank of χ.

Dynamical simulations can be performed by decomposing the time evolution operator $\exp(-iH\delta t)$, for small time step δt, into a sequence of pairwise unitaries via a Suzuki-Trotter expansion. Given the properties outlined such a calculation is likely to be accurate for a practical value of χ if both the initial state and the states generated by the dynamics remain in the low-energy manifold of the system. To determine the appropriate χ calculations are repeated with increasing values of χ until the final result converges and are unaffected by further increases. For practical purposes the convergence is usually quantified by the robustness of the expectation values calculated. The accuracy of a calculation is also gauged by the sum of the discarded Schmidt coefficients at each time step - a quantity which should necessarily be small - and the deviation of normalisation of the final state from unity which indicates the accumulated effect of truncation.

Finally, initial states are typically taken to be the ground state of the system

which are found either by applying the DMRG procedure or, as in this work, by simulating imaginary time evolution through the repeated application of $\exp(-H\delta t)$ and subsequent renormalisation of the state. In our simulations, we have used $\chi = 40$.

3.D The ramp s_{gap}

The ramp s_{gap} can be evaluated as follows. The energy gap between the ground and the first excited state associated with a given lattice profile s is given by $\text{gap}(s) = \omega_{0e}$ where $\omega_{0k} = (\varepsilon_{\text{eff},k} - \varepsilon_{\text{eff},0})$ with $\varepsilon_{\text{eff},\alpha}$ the α-th instantaneous eigenvalue of $\hat{H}_{\text{eff}}(s)$. The gap is evaluated numerically via the direct diagonalisation of $\hat{H}_{\text{eff}}$ for a small number of sites. The function $s_{\text{gap}}(t)$ is defined by the equation $\mathrm{d}s_{\text{gap}}(t)/\mathrm{d}t = \text{gap}(s_{\text{gap}}(t))/K$ where $K^{-1} = \int_0^{\tau_Q} \mathrm{d}t\, \text{gap}(s_{\text{gap}}(t))$ is a normalisation constant.

Chapter 4

Publication

Creation of resilient entangled states and a resource for measurement-based quantum computation with optical superlattices.

B. Vaucher, A. Nunnenkamp, and D. Jaksch

Clarendon Laboratory, University of Oxford, Parks Road, Oxford OX1 3PU, United Kingdom

New J. Phys. **10**, 023005 (2008)

We investigate how to create entangled states of ultracold atoms trapped in optical lattices by dynamically manipulating the shape of the lattice potential. We consider an additional potential (the superlattice) that allows both the splitting of each site into a double well potential, and the control of the height of potential barrier between sites. We use superlattice manipulations to perform entangling operations between neighbouring qubits encoded on the Zeeman levels of the atoms without having to perform transfers between the different vibrational states of the atoms. We show how to use superlattices to engineer many-body entangled states resilient to collective dephasing noise. Also, we present a method to realise a 2D resource for measurement-based quantum computing via Bell-pair measurements. We analyse measurement networks that allow the execution of quantum algorithms while maintaining the resilience properties of the system throughout the computation.

4.1 Introduction

The experimental realisation of bosonic spinor condensates in optical lattices has opened up the possibility to exploit the spin degree of freedom for a wide range of applications [105, 106]. Recently, further experiments have proved that these systems are promising candidates for quantum information processing purposes (see [55] and references therein) and the study of quantum magnetism [53]. In the literature there are several proposals using spinor condensates in optical lattice, e.g. to create macroscopic entangled states [107, 108] or to explore magnetic quantum phases [109]. In this paper, we consider the possibility of using optical superlattices to manipulate the spin degrees of freedom of the atoms and engineer many-body entangled states.

Superlattice setups allow the transformation of every site of the optical lattice into a double-well potential, and also the control of the potential barrier between sites [53, 56, 82]. Atoms with overlapping motional wave functions interact via cold collisions that coherently modify their spin, while conserving the total magnetisation of the system [110, 111]. Thus, by splitting each lattice site into a double-well potential, two atoms occupying the same site become separated by a potential barrier, and the interactions between them are switched off. Similarly, interactions between atoms can be switched on again for a certain time by lowering the potential barrier between the two sides of the double-well. Therefore, superlattice manipulations offer the possibility to apply operations between large numbers of atoms in parallel. In this work, we propose to exploit this parallelism to engineer highly-entangled many-body states.

The process of splitting a Bose-Einstein condensate using double-well potentials has already been studied in the context of mean-field theory [112–114]. In the first part of this paper, we will derive a two-mode effective Hamiltonian that allows an accurate description of the system as the superlattice is progressively turned on.

Our approach differs from previous treatments of double well potentials (see e.g. Ref. [112]) or the work in Ref. [109], as the effective model we use is valid even for low barrier heights. We will use this effective Hamiltonian to analyse the process of splitting every site into a double-well potential starting with two atoms per site. We will show that this process creates a Bell state encoded on the Zeeman levels of the atoms in every site, each atom occupying one side of the double-well. Since these states are resilient to collective dephasing noise, we will use a lattice with a Bell pair in every site as a starting point to engineer many-body entangled states.

In the second part, we present a new method for implementing an entangling $\sqrt{\text{SWAP}}$ gate that does not require to transfer the atoms between different vibrational states. We will show that the application of this entangling gate between (or inside) Bell pairs allows the creation of many-body entangled states resilient to collective dephasing noise.

In the final part, we propose a new method involving superlattice manipulations to realise a 2D resource state for measurement-based quantum computation (MBQC) formally similar to a Bell-encoded cluster state. Since the realisation of logical gates between non-neighbouring qubits is practically very difficult in optical lattices [10], the one-way model for quantum computation is particularly relevant for these systems [12, 13, 115]. The resource state we propose is resilient to collective dephasing noise, which makes it less prone to decoherence than the usual cluster states. Its utilisation as a resource for MBQC requires adjustments of the measurement patterns used for cluster states, which we describe in the last section. We note that the realisation of Bell-encoded cluster states as a resource for MBQC was proposed in Ref. [116] using lattice manipulations in three dimensions. The distinguishing feature of our proposal is that the resource state is created via 2D superlattice operations which have been demonstrated in the lab already.

This paper is organised as follows. In Sec. 4.2 we derive an effective model for

describing the dynamics of atoms within one site in the presence of a superlattice potential. In Sec. 4.3, starting with a lattice where every site contains two atoms of opposite spin, we show how to create a Bell pair in each site by splitting it using a superlattice potential. In Sec. 4.4, we present how to perform a gate between two neighbouring qubits by manipulating the superlattice potential, and in Sec. 4.5 and Sec. 4.6 we show how to use this gate to create and probe many-body entangled states. Finally, in Sec. 4.7 we propose a method for creating a resource for MBQC via Bell-pair measurements and provide measurements network to implement a universal set of gates. We conclude in Sec. 4.8.

4.2 Model

We consider a gas of ultracold alkali atoms loaded into a deep optical lattice. The atoms are assumed to be bosons initialised in the $f = 1$ hyperfine manifold [106]. The lattice potential is given by $V_{OL}(\mathbf{r}, s, \theta) = V_T[\sin^2(\pi z/a)+\sin^2(\pi y/a)+V_S(x, s, \theta)]$ where V_T is the depth of the potential and

$$V_S(x, s, \theta) = (1 - s)\, \sin^2\left(\frac{\pi x}{a} + \theta\right) + s\, \sin^2\left(\frac{2\pi x}{a}\right). \tag{4.1}$$

The depth of the potential will be given in units of the recoil energy $E_R = \hbar^2\pi^2/(2Ma^2)$ where M is the mass of the atoms. The parameter $s \in [0, 1]$ is determined by the relative intensities of the two pairs of lasers. The constant a corresponds to the size of a unit cell when $s = 0$ (see Fig. 4.1a). We will refer to unit cells when $s = 0$ as to *lattice sites*. Changing the value of s from 0 to 1 transforms each site in a double well potential. We will refer to each side of this double well potential when $s = 1$ as to a *subsite*. The angle θ allows for the manipulation of the potential barrier *inside* each site ($\theta = 0$) or *between* sites ($\theta = \pi/2$). A few lattice

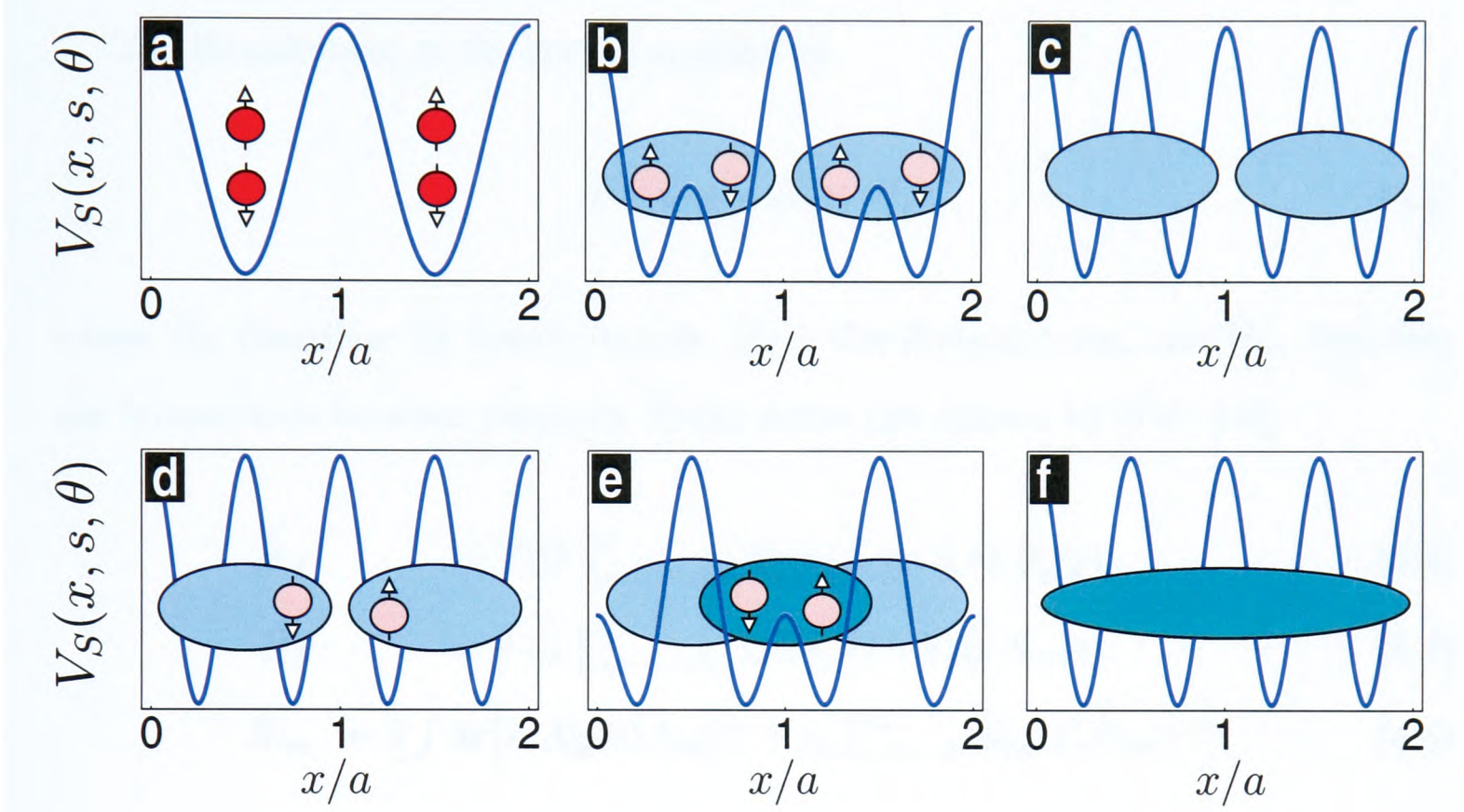


Figure 4.1. (a) The system is initialised with two atoms per site in the state $w_a(\mathbf{r})^2 \otimes \mathcal{S}(|f_1 = 1, m_1 = +1; f_2 = 1, m_2 = -1\rangle)$ and the lattice parameters are $s = 0$ and $\theta = 0$. (b) The lattice potential is smoothly altered by increasing the lattice parameter s while $\theta = 0$. (c) At the end of the first step, the lattice parameter is $s = 1$. Each lattice site then contains a Bell pair. (d-f) After setting the angle to $\theta = \pi/2$, the other set of barriers are lowered by decreasing the lattice parameter s from $s = 1$ (d) to $0 < s < 1$ (e) and back to $s = 1$ (f).

profiles corresponding to different parameters s and θ are shown in Fig. 4.1. In the following, we will refer to the lattice profiles corresponding to the values of $s \approx 0$ and $s \approx 1$ as to the *large* and *small* lattice limits, respectively.

We assume the lattice depth V_T to be sufficiently large so that hopping can be neglected in the small and in the large lattice limits [47].

The Hamiltonian of the system is given by

$$\hat{H} = \hat{H}_K + \hat{H}_Z + \hat{H}_{\text{int}} \tag{4.2}$$

where $\hat{H}_K$ describes the kinetic energy, $\hat{H}_Z$ is the Zeeman term, and $\hat{H}_{\text{int}}$ describes the interactions between particles. These terms are defined by [117, 118]

$$\hat{H}_K = \int \mathrm{d}\mathbf{r} \sum_{\sigma=-1,0,1} \hat{\Psi}^\dagger_\sigma(\mathbf{r})\, \hat{h}_0(\mathbf{r}, s, \theta)\, \hat{\Psi}_\sigma(\mathbf{r}), \tag{4.3}$$

$$\hat{H}_Z = \int \mathrm{d}\mathbf{r} \sum_{\sigma=-1,0,1} \Delta E_{Z,\sigma}(B)\, \hat{\Psi}^\dagger_\sigma(\mathbf{r}) \hat{\Psi}_\sigma(\mathbf{r}), \tag{4.4}$$

$$\hat{H}_{\text{int}} = \tfrac{1}{2} \int \mathrm{d}\mathbf{r} \Big[c_0 \hat{A}^\dagger_{00}(\mathbf{r}) \hat{A}_{00}(\mathbf{r}) + c_2 \sum\nolimits_{m=-2}^{2} \hat{A}^\dagger_{2m}(\mathbf{r}) \hat{A}_{2m}(\mathbf{r}) \Big], \tag{4.5}$$

where $c_0 = 4\pi\hbar^2(2a_2 + a_0)/(3M)$ and $c_2 = 4\pi\hbar^2(a_2 - a_0)/(3M)$ with a_F the s-wave scattering length of the channel associated with the total angular momentum F, $\hat{h}_0 = (-\hbar^2\nabla^2/2M) + V_{OL}(\mathbf{r}, s, \theta)$ and $\Delta E_{Z,\sigma}(B)$ is the energy shift caused by the Zeeman effect in the presence of a magnetic field $\mathbf{B} = (0, 0, B)$ oriented in the z–direction. The operator $\hat{A}_{Fm_F}(\mathbf{r})$ is given by

$$\hat{A}_{Fm_F}(\mathbf{r}) = \sum_{m_1,m_2=-f}^{f} \langle\, F, m_F \,|\, f_1, m_1; f_2, m_2 \,\rangle\, \hat{\Psi}_{m_1}(\mathbf{r}) \hat{\Psi}_{m_2}(\mathbf{r}), \tag{4.6}$$

where $|\, f_1, m_1; f_2, m_2\rangle = |\, f_1, m_1\rangle \otimes |\, f_2, m_2\rangle$ and $\langle\, F, m_F \,|\, f_1, m_1; f_2, m_2 \,\rangle$ is a Clebsch-Gordan coefficient.

In 4.A, we derive the effective Hamiltonian describing the dynamics of the atoms

at one site using the field operator

$$\hat{\Psi}^{\dagger}_{\sigma}(\mathbf{r}) = \hat{a}^{\dagger}_{\sigma} w_a(\mathbf{r}) + \hat{b}^{\dagger}_{\sigma} w_b(\mathbf{r}), \tag{4.7}$$

where $\hat{a}^{\dagger}_{\sigma}(\hat{b}^{\dagger}_{\sigma})$ is the operator that creates a particle with spin $|\, f = 1, m_f = \sigma\rangle$ ($\sigma = \{-1, 0, 1\}$ denotes the Zeeman level) in a motional state associated with the symmetric (anti-symmetric) mode function $w_a(w_b)$. The mode functions are centred in the middle of the site, and their shape depends on the lattice parameter s. The field operators obey the canonical bosonic commutation relations $[\hat{\Psi}_{\sigma}(\mathbf{r}), \hat{\Psi}^{\dagger}_{\sigma'}(\mathbf{r}')] = \delta_{\sigma\sigma'}\delta(\mathbf{r} - \mathbf{r}')$ and $[\hat{\Psi}_{\sigma}(\mathbf{r}), \hat{\Psi}_{\sigma'}(\mathbf{r}')] = [\hat{\Psi}^{\dagger}_{\sigma}(\mathbf{r}), \hat{\Psi}^{\dagger}_{\sigma'}(\mathbf{r}')] = 0$. We will see in the next section that the inclusion of a second motional mode in the Hamiltonian allows an accurate description of the system's dynamics in both the large *and* the small lattice limit [119]. A more detailed explanation of the interaction term (4.5), as well as the full Hamiltonian of the system in terms of creation (annihilation) operators can be found in 4.A.

4.3 Creation of a Bell state on every lattice site

In this section, we use the effective Hamiltonian introduced in the previous section to show how to generate a lattice where every site contains a Bell state encoded on the Zeeman levels of the atoms. This procedure will be used as a preliminary step to engineer several types of many-body entangled states.

We start with a deep optical lattice in the large lattice limit (LLL) and two atoms per lattice site in the state

$$|\,\psi_{\text{init}}\rangle = w_a(\mathbf{r})^2 \otimes \mathcal{S}\left(|\, f_1 = 1, m_1 = +1; f_2 = 1, m_2 = -1\rangle\right), \tag{4.8}$$

where $\mathcal{S}$ is the symmetrisation operator. In general, the two atoms can undergo

spin-changing collisions coupling to various hyperfine levels. As we want to implement qubits on the Zeeman levels, we will limit the spin dynamics effectively to two hyperfine states. There are several ways to achieve this in practice: (i) One possibility is to exploit the conservation of angular momentum and choose two states such as $|f = 2, m_f = +2\rangle$ and $|f = 1, m_f = +1\rangle$, which are not coupled to any other hyperfine states by the inter-atomic interaction. (ii) An accidental degeneracy in ^{87}Rb offers yet another possible route: since the two s-wave scattering lengths a_0 and a_2 are almost equal, transitions between the state $|f_1 = 1, m_1 = 0; f_2 = 1, m_2 = 0\rangle$ and states where particles have opposite spins occur on a time scale $(c_0 + c_2)/c_2 \approx 3a_2/(a_2 - a_0) \approx 300$ times slower than any other allowed transition. Hence, after initialising the system at time $t = 0$ in state (4.8), we can limit our dynamical description to transitions between states with opposite spins, as long as the manipulations we are about to propose happen on a faster time scale than this transition. Notice that the use of fast-switched microwave fields that suppress spin-changing collisions [105] allows the relaxation of the constraint to be faster than the original time-scale of spin-changing collisions. The preparation of the state (4.8) has already been experimentally achieved [106, 111].

The first step in our proposal consists of raising the superlattice potential, i.e. changing the lattice parameter $s(t)$ from the LLL at time $t = 0$ to the small lattice limit (SLL) at some time $t = T$ sufficiently slowly so that the ramp does not create excitations in the system. Once the superlattice is fully ramped up, each site is split in two, atoms no longer interact with each other and their spin state remains frozen in time.

The shape of the mode functions $w_a(\mathbf{r})$ and $w_b(\mathbf{r})$ depends on the lattice parameter. In the LLL, they correspond to the ground and first excited state of each lattice site. However, as the lattice parameter s approaches the SLL, the mode functions transform into the symmetric and anti-symmetric superpositions

$w_a(\mathbf{r}) = [\varphi_L(\mathbf{r}) + \varphi_R(\mathbf{r})]/\sqrt{2}$ and $w_b(\mathbf{r}) = [\varphi_L(\mathbf{r}) - \varphi_R(\mathbf{r})]/\sqrt{2}$, where the mode functions $\varphi_L(\mathbf{r})$ and $\varphi_R(\mathbf{r})$ are centred on either side of the double-well potential [112, 119]. Hence, when the mode functions $w_{L,R}(\mathbf{r})$ become centred within each sub-site [119], it is convenient to write the Hamiltonian of the system in terms of the operators

$$\begin{aligned} \hat{c}^\dagger_{L,\sigma} &= (\hat{a}^\dagger_\sigma + \hat{b}^\dagger_\sigma)/\sqrt{2} \\ \hat{c}^\dagger_{R,\sigma} &= (\hat{a}^\dagger_\sigma - \hat{b}^\dagger_\sigma)/\sqrt{2}, \end{aligned} \tag{4.9}$$

which create a particle with spin σ on the left and right side of the double-well potential, respectively. In the basis

$$\begin{aligned} |\uparrow\downarrow,\rangle = \hat{c}^\dagger_{L,\uparrow}\hat{c}^\dagger_{L,\downarrow}\,|\,\mathrm{vac}\rangle &= (\hat{a}^\dagger_\uparrow + \hat{b}^\dagger_\uparrow)(\hat{a}^\dagger_\downarrow + \hat{b}^\dagger_\downarrow)/2\,|\,\mathrm{vac}\rangle\,, \\ |\uparrow,\downarrow\rangle = \hat{c}^\dagger_{L,\uparrow}\hat{c}^\dagger_{R,\downarrow}\,|\,\mathrm{vac}\rangle &= (\hat{a}^\dagger_\uparrow + \hat{b}^\dagger_\uparrow)(\hat{a}^\dagger_\downarrow - \hat{b}^\dagger_\downarrow)/2\,|\,\mathrm{vac}\rangle\,, \\ |\downarrow,\uparrow\rangle = \hat{c}^\dagger_{L,\uparrow}\hat{c}^\dagger_{R,\downarrow}\,|\,\mathrm{vac}\rangle &= (\hat{a}^\dagger_\uparrow - \hat{b}^\dagger_\uparrow)(\hat{a}^\dagger_\downarrow + \hat{b}^\dagger_\downarrow)/2\,|\,\mathrm{vac}\rangle\,, \\ |,\uparrow\downarrow\rangle = \hat{c}^\dagger_{R,\uparrow}\hat{c}^\dagger_{R,\downarrow}\,|\,\mathrm{vac}\rangle &= (\hat{a}^\dagger_\uparrow - \hat{b}^\dagger_\uparrow)(\hat{a}^\dagger_\downarrow - \hat{b}^\dagger_\downarrow)/2\,|\,\mathrm{vac}\rangle\,, \end{aligned} \tag{4.10}$$

the Hamiltonian of the system reads (see 4.A)

$$\hat{H}_{\uparrow\downarrow} = \begin{pmatrix} \tilde{E}+\tilde{U}_{\uparrow\downarrow} & \tilde{J}_{\uparrow\downarrow} & \tilde{J}_{\uparrow\downarrow} & \chi_{\uparrow\downarrow} \\ \tilde{J}_{\uparrow\downarrow} & \tilde{E}+\chi_{\uparrow\downarrow} & \chi_{\uparrow\downarrow} & \tilde{J}_{\uparrow\downarrow} \\ \tilde{J}_{\uparrow\downarrow} & \chi_{\uparrow\downarrow} & \tilde{E}+\chi_{\uparrow\downarrow} & \tilde{J}_{\uparrow\downarrow} \\ \chi_{\uparrow\downarrow} & \tilde{J}_{\uparrow\downarrow} & \tilde{J}_{\uparrow\downarrow} & \tilde{E}+\tilde{U}_{\uparrow\downarrow} \end{pmatrix}, \tag{4.11}$$

where $\tilde{E} = V_a + V_b$ with $V_\nu = \int \mathrm{d}\mathbf{r}\, w^*_\nu(\mathbf{r})\hat{h}_0\, w_\nu(\mathbf{r})$ and $\hat{h}_0 = (-\hbar^2\nabla^2/2M) + V_{OL}(\mathbf{r}, s, \theta)$ is the sum of the single-particle energies, $\tilde{U}_{\uparrow\downarrow} = \gamma_{\uparrow\downarrow}(U_{aa} + U_{bb} + 6U_{ab})/4$ with $\gamma_{\uparrow\downarrow}U_{\nu\nu'} = \gamma_{\uparrow\downarrow}\int \mathrm{d}\mathbf{r}\,(|w_\nu(\mathbf{r})||w_{\nu'}(\mathbf{r})|)^2$ and $\gamma_{\uparrow\downarrow} = c_0 - c_2$ is the generalised on-site interaction, $\tilde{J}_{\uparrow\downarrow} = (V_a - V_b)/2 + \gamma_{\uparrow\downarrow}(U_{aa} - U_{bb})/4$ the generalised tunneling matrix element

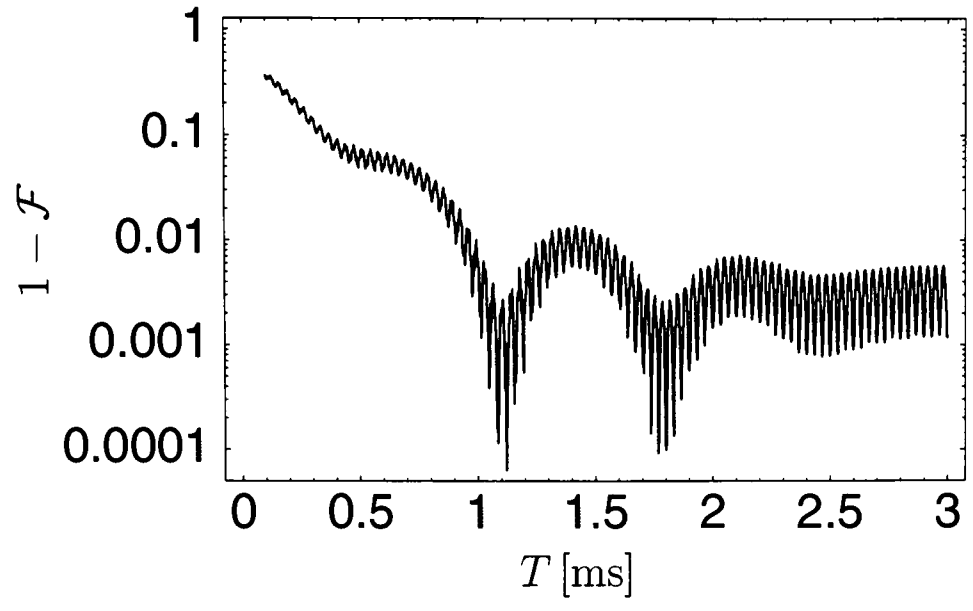


Figure 4.2. Numerical calculation of the anti-fidelity $1 - \mathcal{F}$ where $\mathcal{F} = |\langle \psi | \psi_0 \rangle|^2$ with $|\psi\rangle$ the state of the two atoms at the end of the ramping. We have used the parameters of a lattice with period $a = \lambda/2$, $\lambda = 840\,\mathrm{nm}$, and $V_T = 60E_R$, initialised with two ^{87}Rb atoms per site in the state (4.8) at time $T = 0$ and a magnetic field of $B = 30\,\mathrm{G}$.

between the two sides of the well, and $\chi_{\uparrow\downarrow} = \gamma_{\uparrow\downarrow}(U_{aa} + U_{bb} - 2U_{ab})/4$ corresponds to the density-density interaction energy between the two sides of the double-well. The latter is proportional to the overlap between the functions $\varphi_L(\mathbf{r})$ and $\varphi_R(\mathbf{r})$. It cancels in the small lattice limit as a consequence of the localisation of the mode functions $\varphi_L(\mathbf{r})$ and $\varphi_R(\mathbf{r})$ inside each subsite.

Our two-mode model does not only describe the system well in both limits, it also takes into account the effects of density-density interactions between two subsites when the potential barrier between them is still not fully ramped up. This property makes it particularly valuable for the study of the system dynamics *between* the two limits.

In the SLL, the Hamiltonian (4.11) reduces (up to the energy shift E) to

$$\hat{H}^{\mathrm{SLL}}_{\uparrow\downarrow} = \begin{pmatrix} U_{\uparrow\downarrow} & -J & -J & 0 \\ -J & 0 & 0 & -J \\ -J & 0 & 0 & -J \\ 0 & -J & -J & U_{\uparrow\downarrow} \end{pmatrix}. \tag{4.12}$$

where $V_a = E - J$ and $V_b = E + J$ with $E = \int \mathrm{d}\mathbf{r}\, \varphi_L^*(\mathbf{r}) \hat{h}_0\, \varphi_L(\mathbf{r})$ is the single-particle energy and $J = \int \mathrm{d}\mathbf{r}\, \varphi_L^*(\mathbf{r}) \hat{h}_0\, \varphi_R(\mathbf{r})$ the hopping integral, and $\tilde{U}_{\uparrow\downarrow} = \gamma_{\uparrow\downarrow} \int \mathrm{d}\mathbf{r}\, |\varphi_L|^4$ is the on-site interaction [119].

For zero tunneling $J = 0$, the Hamiltonian $\hat{H}^{\mathrm{SLL}}_{\uparrow\downarrow}$ has two degenerate ground states: $|\uparrow,\downarrow\rangle$ and $|\downarrow,\uparrow\rangle$. This degeneracy is lifted at finite J where the symmetric superposition

$$|\psi_0\rangle = \frac{1}{\sqrt{2}}(|\uparrow,\downarrow\rangle + |\downarrow,\uparrow\rangle) \tag{4.13}$$

is the ground and the antisymmetric superposition the first excited state. These two low-lying energy levels with an energy splitting of $4J^2/U_{\uparrow\downarrow}$ are separated from the other excited states by the interaction energy $U_{\uparrow\downarrow}$.

We have carried out a dynamical simulation of the splitting dynamics using the exact *full* Hamiltonian defined in Eq. (4.2) and 4.A for two particles and one site. For the time-scales considered throughout this paper, non-adiabatic effects due to the changes of shape of the mode functions can be safely neglected [119]. We have used $s(t) = \sin^2[t/(2T)]$, and computed the anti-fidelity $1 - \mathcal{F}$ with $\mathcal{F} = |\langle \psi | \psi_0 \rangle|^2$ between the state $|\psi\rangle$ of the system at the end of the numerical simulation of the ramp and the Bell state (4.13). For the parameters considered, we have found that the anti-fidelity reaches $1 - \mathcal{F} \approx 10^{-3}$ for a quench time of $T \sim 1.1 \pm 0.1\,\mathrm{ms}$ (see Fig. 4.2). It is expected that better fidelity can be obtained for larger values of $U_{\uparrow\downarrow}$ [120]. This observation makes our scheme relevant for current experimental

setups.

Thus, changing the topology of the optical lattice from the LLL to the SLL drives the state of the atoms within each lattice site from (4.8) to the maximally entangled Bell state (4.13). Non-adiabatic transitions to excited states are suppressed by opposite parity in the case of the first excited state and by the on-site interaction $U_{\uparrow\downarrow}$ in the case of the other excited states. After this first step has been completed, a system of initially N sites contains $k = 2N$ subsites and its state is given by a tensor product of Bell pairs

$$\left| \Phi_k^{(0)} \right\rangle = \bigotimes_{i=1}^{N} |\psi_0\rangle \,. \tag{4.14}$$

Remarkably, the system in state (4.14) is resilient to dephasing noise for a magnetic field slowly varying over a distance of one lattice site [55].

4.4 Implementation of an entangling gate

Since the interactions between two atoms depend on the overlap between their wave functions, they can be dynamically switched on and off by lowering and raising the potential barrier between the two subsites. This is done by varying the lattice parameter s from $s = 1$ at time $t = 0$ to $s = 1 - \eta$ and back to $s = 1$ at time $t = \tau$. In the SLL, where $\tilde{J}_{\uparrow\downarrow}/\tilde{U}_{\uparrow\downarrow} \ll 1$, tunneling can be treated perturbatively, and the Hamiltonian (4.11) can be projected onto the subspace of singly-occupied sites.

We distinguish two cases: either the neighbouring subsites are occupied by atoms with opposite or equal spins. For two atoms with opposite spins, we can use Eq. (4.11) and the effective Hamiltonian in the basis $|\uparrow,\downarrow\rangle$ and $|\downarrow,\uparrow\rangle$ reads (up

to a constant energy shift) in second-order perturbation theory

$$\hat{H}^{(\mathrm{eff})}_{\uparrow\downarrow} = \left(\frac{2\tilde{J}^2_{\uparrow\downarrow}}{\tilde{U}_{\uparrow\downarrow}} + \chi_{\uparrow\downarrow}\right)\begin{pmatrix} 1 & 1 \\ 1 & 1 \end{pmatrix}. \tag{4.15}$$

Since the effective Hamiltonian commutes with itself at different times, we obtain the following analytical expression for the time evolution operator

$$\hat{U}(\tau) = \exp\left(-\frac{\mathrm{i}}{\hbar}\int_0^\tau H^{(\mathrm{eff})}_{\uparrow\downarrow}\,\mathrm{d}t\right) = \begin{pmatrix} \mathrm{e}^{-\mathrm{i}\phi}\cos\phi & -\mathrm{i}\mathrm{e}^{-\mathrm{i}\phi}\sin\phi \\ -\mathrm{i}\mathrm{e}^{-\mathrm{i}\phi}\sin\phi & \mathrm{e}^{-\mathrm{i}\phi}\cos\phi \end{pmatrix}, \tag{4.16}$$

where the phase ϕ is given by

$$\phi(\tau) = \frac{1}{\hbar}\int_0^\tau \left(\frac{2\tilde{J}^2_{\uparrow\downarrow}}{\tilde{U}_{\uparrow\downarrow}} + \chi_{\uparrow\downarrow}\right)\mathrm{d}t. \tag{4.17}$$

While the first term in Eq. (4.17) is due to second-order tunneling [53, 109], the second term is due to density-density interactions. This term is negligible in the SLL, but when the potential barrier between the two sides of the double well is reduced, it adds an extra phase between neighbouring particles with different spins because of the difference between the scattering lengths c_0 and c_2.

For atoms with equal spins $\sigma = \{\uparrow, \downarrow\}$ we start by writing down the basis states as

$$\begin{aligned} |\,\sigma\sigma,\rangle = \hat{c}^\dagger_{L,\sigma}\hat{c}^\dagger_{L,\sigma}\,|\,\mathrm{vac}\rangle &= (\hat{a}^\dagger_\sigma + \hat{b}^\dagger_\sigma)(\hat{a}^\dagger_\sigma + \hat{b}^\dagger_\sigma)/(2\sqrt{2})\,|\,\mathrm{vac}\rangle \\ |\,\sigma,\sigma\rangle = \hat{c}^\dagger_{L,\sigma}\hat{c}^\dagger_{R,\sigma}\,|\,\mathrm{vac}\rangle &= (\hat{a}^\dagger_\sigma + \hat{b}^\dagger_\sigma)(\hat{a}^\dagger_\sigma - \hat{b}^\dagger_\sigma)/2\,|\,\mathrm{vac}\rangle \\ |\,,\sigma\sigma\rangle = \hat{c}^\dagger_{R,\sigma}\hat{c}^\dagger_{R,\sigma}\,|\,\mathrm{vac}\rangle &= (\hat{a}^\dagger_\sigma - \hat{b}^\dagger_\sigma)(\hat{a}^\dagger_\sigma - \hat{b}^\dagger_\sigma)/(2\sqrt{2})\,|\,\mathrm{vac}\rangle\,, \end{aligned} \tag{4.18}$$

in which the Hamiltonian reads

$$\hat{H}_{\sigma\sigma} = \begin{pmatrix} \tilde{E}_{\sigma\sigma} + \tilde{U}_{\sigma\sigma} & \tilde{J}_{\sigma\sigma} & \chi_{\sigma\sigma} \\ \tilde{J}_{\sigma\sigma} & \tilde{E}_{\sigma\sigma} + \chi_{\sigma\sigma} & \tilde{J}_{\sigma\sigma} \\ \chi_{\sigma\sigma} & \tilde{J}_{\sigma\sigma} & \tilde{E}_{\sigma\sigma} + \tilde{U}_{\sigma\sigma} \end{pmatrix}, \tag{4.19}$$

where $\gamma_{\sigma\sigma} = c_0 + c_2$ is the interaction constant for particles with equal spin σ, $\tilde{E}_{\sigma\sigma} = V_a + V_b \pm E_Z$ the sum of single-particle energies, $E_Z = -g\mu_B B/2\hbar$ the Zeeman energy shift in the first order, $\tilde{J}_{\sigma\sigma} = (V_a - V_b)/\sqrt{2} + \gamma_{\sigma\sigma}(U_{aa} - U_{bb})/4$ the generalised tunneling matrix element, $\tilde{U}_{\sigma\sigma} = \gamma_{\sigma\sigma}(U_{aa} + U_{bb} + 6U_{ab})/4$ the generalised on-site interaction and $\chi_{\sigma\sigma} = \gamma_{\sigma\sigma}(U_{aa} + U_{bb} - 2U_{ab})/4$ the off-site density-density interaction.

In the SLL this reduces (up to the energy shift of $\tilde{E}_{\sigma\sigma}$) to

$$\hat{H}^{SLL}_{\sigma\sigma} = \begin{pmatrix} U_{\sigma\sigma} & -\sqrt{2}J & 0 \\ -\sqrt{2}J & 0 & -\sqrt{2}J \\ 0 & -\sqrt{2}J & U_{\sigma\sigma} \end{pmatrix}. \tag{4.20}$$

For the state $|\sigma, \sigma\rangle$ there are no other low-energy states accessible, so that it acquires only the phase factor $e^{i\kappa}$ during the sweep. In second-order perturbation theory we find that κ is similar to (4.17)

$$\kappa = \frac{1}{\hbar}\int_0^\tau \left(\frac{4\tilde{J}^2_{\sigma\sigma}}{\tilde{U}_{\sigma\sigma}} + \chi_{\sigma\sigma}\right) \mathrm{d}t. \tag{4.21}$$

Since $\tilde{J}_{\uparrow\downarrow} \to -J$, $\tilde{J}_{\sigma\sigma} \to -\sqrt{2}J$ and $\gamma_{\uparrow\downarrow}/\gamma_{\sigma\sigma} = (c_0 - c_2)/(c_0 + c_2) \approx 1$, we get $\kappa \approx 2\phi$.

Putting the results of this section together we find that lowering and raising the potential barrier between two subsites n and $n+1$ implements the two-qubit gate

$\hat{U}$ given by

$$\hat{U}\begin{pmatrix} |00\rangle \\ |01\rangle \\ |10\rangle \\ |11\rangle \end{pmatrix} = \begin{pmatrix} e^{iE_Z\tau} & 0 & 0 & 0 \\ 0 & e^{i\phi}\cos\phi & -ie^{i\phi}\sin\phi & 0 \\ 0 & -ie^{i\phi}\sin\phi & e^{i\phi}\cos\phi & 0 \\ 0 & 0 & 0 & e^{-iE_Z\tau} \end{pmatrix}\begin{pmatrix} |00\rangle \\ |01\rangle \\ |10\rangle \\ |11\rangle \end{pmatrix}. \quad (4.22)$$

where $|ij\rangle = |i\rangle_n \otimes |j\rangle_{n+1}$ with $|1\rangle_n = \hat{c}^\dagger_{n,\uparrow}|\text{vac}\rangle$ and $|0\rangle_n = \hat{c}^\dagger_{n,\downarrow}|\text{vac}\rangle$ where $\hat{c}^\dagger_{n,\downarrow}$ and $\hat{c}^\dagger_{n,\uparrow}$ are the creation operators of a particle at subsite n with spin $\downarrow$ and $\uparrow$, respectively.

Numerical simulations of the system dynamics have been carried out using the exact full Hamiltonian for two particles and one site—that is, including the contribution of spin changing collisions to the $m_f = 0$ state—for a system of ^{87}Rb atoms, $V_T = 60E_R$ and $\eta = 0.3$. We have computed the overlap between the states resulting from the numerical simulation with their analytical approximation and found that for the parameters considered and switching times τ up to tens of milliseconds, the time evolution operator of the system is accurately approximated by Eq. (4.22). For longer times τ, the evolution of the system in the reduced Hilbert becomes non-unitary due to slow transitions to the state where the two particles have spins $\sigma = 0$, as expected.

Since the application of the gate $\hat{U}$ is realised in parallel on all qubits in the x–direction, the phase due to the Zeeman shift in the first order in B cancels for systems with an equal number of atoms in the $\sigma = +1$ and $\sigma = -1$ state. For such systems, we find that for ramping times τ such that $\phi(\tau) = \{\pi/4, \pi/2, 3\pi/4\}$, lattice

manipulations realise the gates (in the usual computational basis) [121]

$$\hat{U}_{\frac{\pi}{4}} = \sqrt{\text{SWAP}} \tag{4.23}$$

$$\hat{U}_{\frac{\pi}{2}} = \text{SWAP}, \tag{4.24}$$

$$\hat{U}_{\frac{3\pi}{4}} = \text{SWAP}\sqrt{\text{SWAP}} = \sqrt{\text{SWAP}}^{\dagger}. \tag{4.25}$$

In the remainder of this paper we will show that, using a lattice of Bell pairs as a starting point, this gate[1] can be used to create both many-body entangled states and a resource state for MBQC.

4.5 Creation and detection of a state with a tunable amount of entanglement

Depending on whether the lattice parameter θ is set to $\theta = 0$ or $\theta = \pi/2$, the gate U_ϕ in Eq. (4.22) is applied between neighbouring subsites inside or between lattice sites, respectively. Up to an irrelevant global phase, these operations read

$$\hat{\mathcal{U}}^{\text{in}}(\hat{U}) = \bigotimes_{n=1}^{N} \hat{U} \tag{4.26}$$

or

$$\hat{\mathcal{U}}^{\text{bw}}(\hat{U}) = \hat{\mathbb{1}} \otimes \bigotimes_{n=1}^{N-1} \hat{U} \otimes \hat{\mathbb{1}}. \tag{4.27}$$

Using this notation, we define a *knitting* operator by

$$\hat{\mathcal{K}}(\hat{U}) = \hat{\mathcal{U}}^{\text{in}}(\hat{U})\hat{\mathcal{U}}^{\text{bw}}(\hat{U}). \tag{4.28}$$

[1] In the context of optical lattices, different methods to implement this gate have been put forward for different encodings of the logical qubits [29, 122, 123]. Recently, a $\sqrt{\text{SWAP}}$ gate between qubits encoded on the internal spin state of the atoms was realised experimentally by manipulating both the spin and motional degrees of freedom of the atoms by means of optical superlattices [55].

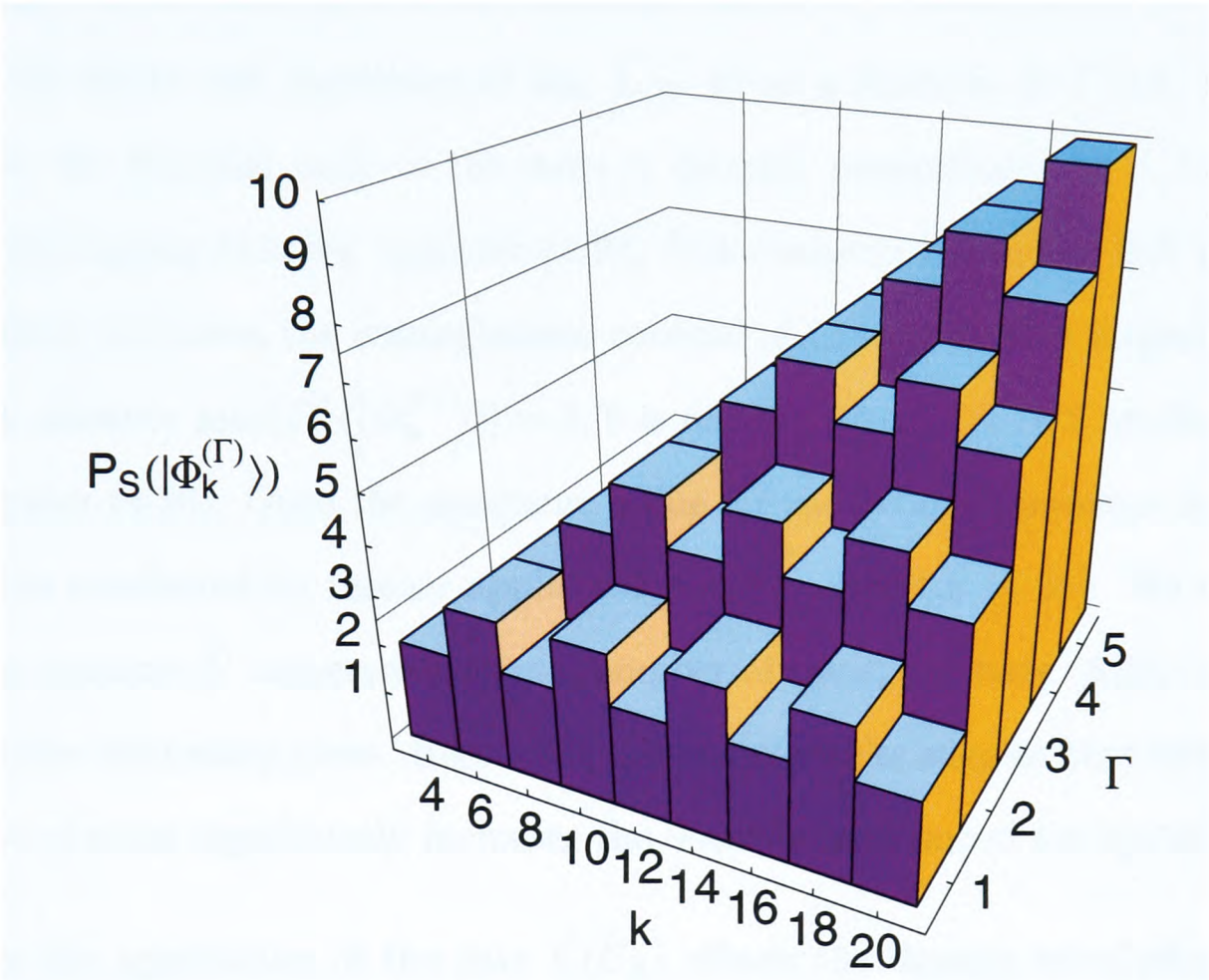


Figure 4.3. Schmidt measure of the state (4.29) as a function of Γ and k. The Schmidt decomposition of the state (4.29) was calculated by partitioning the system in equal parts, which yields the maximum possible Schmidt rank.

Starting from a lattice of Bell pairs, the state resulting from Γ successive applications of the operator $\hat{\mathcal{K}}(\hat{\mathcal{U}}_{\frac{\pi}{4}})$ on the state (4.14) is denoted by

$$\left|\Phi_k^{(\Gamma)}\right\rangle = \hat{\mathcal{K}}(\hat{U}_{\frac{\pi}{4}})^{\Gamma}\left|\Phi_k^{(0)}\right\rangle. \tag{4.29}$$

In Fig. 4.3, we have plotted the Schmidt measure P_{s}^{L} of the state (4.29) for up to $k = 20$ qubits and partitions of size $L = 10$ as a function of Γ [12, 124]. We find that the Schmidt rank of the state is directly proportional to Γ, i.e. applying the entangling knitting operator (4.28) first connects the initial Bell pairs and then further increases the entanglement content of the state. The largest possible Schmidt measure $\max[P_{\mathrm{s}}^{L}(\left|\Phi_k^{(\Gamma)}\right\rangle)] = k/2$ is reached after $\Gamma = N/2$ applications of the operator (4.28). Once the maximum value for the Schmidt measure is reached, it remains unaffected by further applications of the operator (4.28). We note that since the operator $\hat{U}$ conserves the total number of spins, the state (4.29) is resilient to collective dephasing noise. Recent experimental results suggest that resilience to this type of noise significantly increases the decoherence time of the system [55].

Since the application of the gate $\hat{\mathcal{K}}(\hat{U}_{\frac{\pi}{4}})$ affects the density correlations in the lattice, its effect on the system can be observed experimentally via state-selective measurement of the quasi-momentum distribution (QMD) of atoms with spin up [6, 55]

$$n_q^{\uparrow} = \frac{1}{2N}\sum_{i,j=1}^{2N} \mathrm{e}^{-\mathrm{i}\pi q(i-j)/N}\langle \hat{c}_{i,\uparrow}^{\dagger}\hat{c}_{j,\uparrow}\rangle. \tag{4.30}$$

As an illustration, we have plotted in Fig. 4.4 the QMD of a system of $k = 14$ atoms after $\Gamma = 1$ and $\Gamma = 7$ applications of the operator $\hat{\mathcal{K}}(\hat{U}_{\frac{\pi}{4}})$ on the state (4.14). Hence, starting from a lattice of Bell pairs, superlattice manipulations allow the creation of an entangled state with a tunable Schmidt rank that has a distinct experimental signature and is resilient to collective dephasing noise. These properties make this

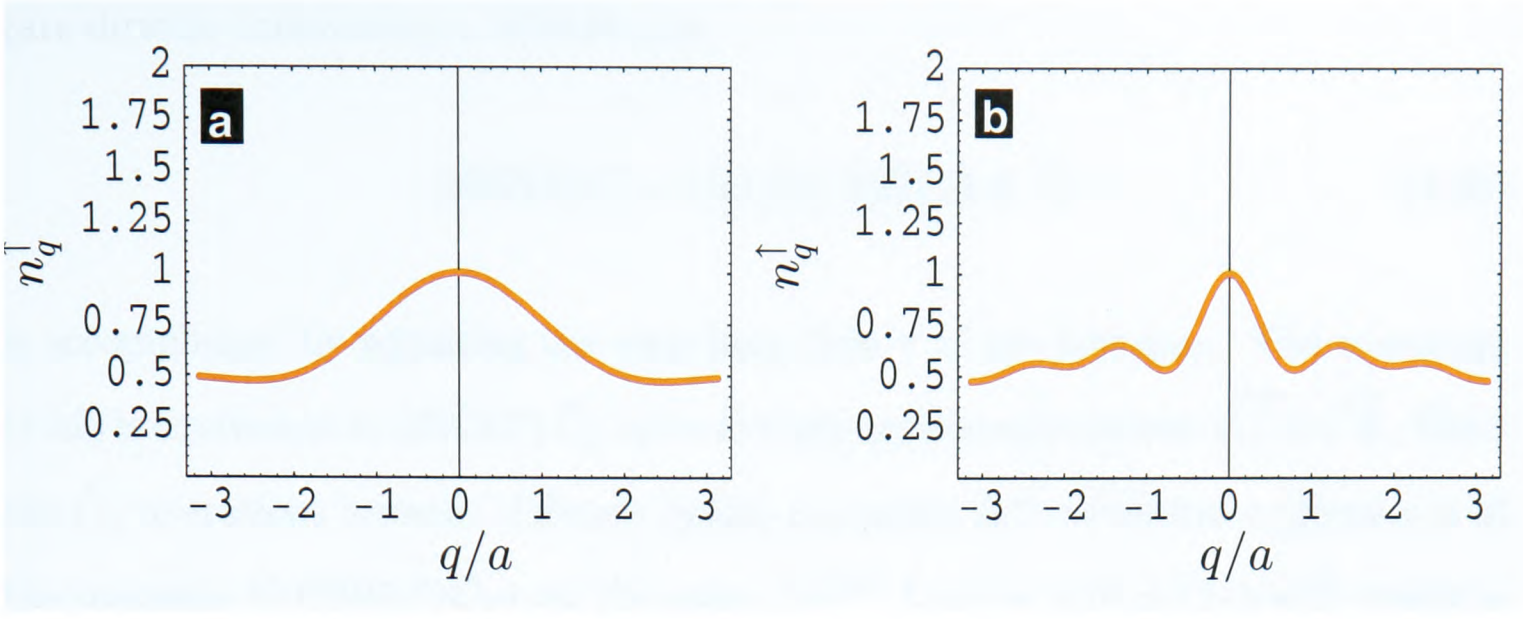


Figure 4.4. (a) Quasi-momentum distribution of $k = 14$ atoms after the application of the gate $\hat{\mathcal{K}}(\hat{U}_{\frac{\pi}{4}})^{\Gamma}$ on the state (4.14) for (a) $\Gamma = 1$ and (b) $\Gamma = 7$. After $\Gamma = 7$ applications of the knitting operator, the state is maximally entangled.

state suitable for experimental studies of many-body entanglement.

4.6 Creation of maximally entangled states

Together with site-selective single-qubit operations applied in parallel on every second atom, superlattice manipulations can be used to implement the entangling phase-gate operation

$$\hat{C}_{\mathrm{i}} = \hat{U}_{\frac{\pi}{4}}(\hat{Z} \otimes \hat{\mathbb{1}})\hat{U}_{\frac{\pi}{4}}(\hat{\mathbb{1}} \otimes \hat{Z}), \tag{4.31}$$

where $\hat{C}_{\mathrm{i}} = \mathrm{diag}(1, -\mathrm{i}, -\mathrm{i}, 1)$ and $\hat{Z}$ is the Pauli matrix defined as $\hat{Z} = \mathrm{diag}(1, -1)$ in the usual computational basis. The operation $\hat{C}_{\mathrm{i}}$ is related to the operation $\hat{C}_Z = \mathrm{diag}(1, 1, 1, -1)$ by applying the single-qubit gate $\sqrt{\hat{Z}} \otimes \sqrt{\hat{Z}}$ on every site of the lattice. A proposal for realising arbitrary single-qubit gates on individual atoms in an optical lattice can be found in Ref. [9]. Notice that the single-qubit operations required to implement the gate (4.31) between sites can be performed in parallel, and so each site need not be addressed separately. The implementation of a phase

gate directly followed by a SWAP gate

$$(\text{SWAP})\,\hat{C}_i = \hat{U}^{\dagger}_{\frac{\pi}{4}}(\hat{Z}\otimes\hat{\mathbb{1}})\hat{U}_{\frac{\pi}{4}}(\hat{\mathbb{1}}\otimes\hat{Z}) \tag{4.32}$$

is accomplished by adjusting the switching time τ of the last gate. The operation (4.32) is equivalent to (SWAP) $\hat{C}_Z$ up to the unitary transformation $\sqrt{\hat{Z}}\otimes\sqrt{\hat{Z}}$. Since the $\hat{C}_Z$ operations between different qubits commute, $k/2$ successive applications of the operator $\hat{\mathcal{K}}((\text{SWAP})\hat{C}_Z)$ on the state $|+\rangle^{\otimes k}$ ($|\pm\rangle = (|0\rangle \pm |1\rangle)/\sqrt{2}$) create a complete graph state $|K_N\rangle$. Complete graphs have the property that each vertex is connected to all the vertices of the graph, i.e. a complete graph of k vertices contains $k(k-1)/2$ edges. Graph states of complete graphs are equivalent to the maximally entangled state $|GHZ\rangle = (|0\rangle^{\otimes k} + |1\rangle^{\otimes k})/\sqrt{2}$ up to local unitary operations.

Superlattice manipulations alone allow the realisation of the state

$$\left|\Phi_k^{\text{graph}}\right\rangle = \hat{\mathcal{U}}^{\text{bw}}(\hat{U}^{\dagger}_{\frac{\pi}{4}})\hat{\mathcal{K}}(\hat{U}^{\dagger}_{\frac{\pi}{4}})^{(k/2)-1}\left|\Phi_k^{(0)}\right\rangle \tag{4.33}$$

resulting from $k-1$ successive applications of the operator (4.25) between and inside each site. The process leading to state (4.33) is schematically represented in Fig. 4.5. This state is resilient to collective dephasing noise, and possesses a structure similar to a complete graph state (see Fig. 4.5). Via the brute-force numerical calculation of the parameters of single-qubit unitary operations, we have found that (4.33) is locally equivalent to a complete graph state of the same size for up to $k = \{4, 6, 8\}$ qubits. This suggests that this property holds for an arbitrary number of qubits.

The resilience of this state to collective dephasing noise, and its symmetry properties make it a good candidate for the improvement of the sensitivity of quantum spectroscopic measurements in noisy environments (see Ref. [125]).

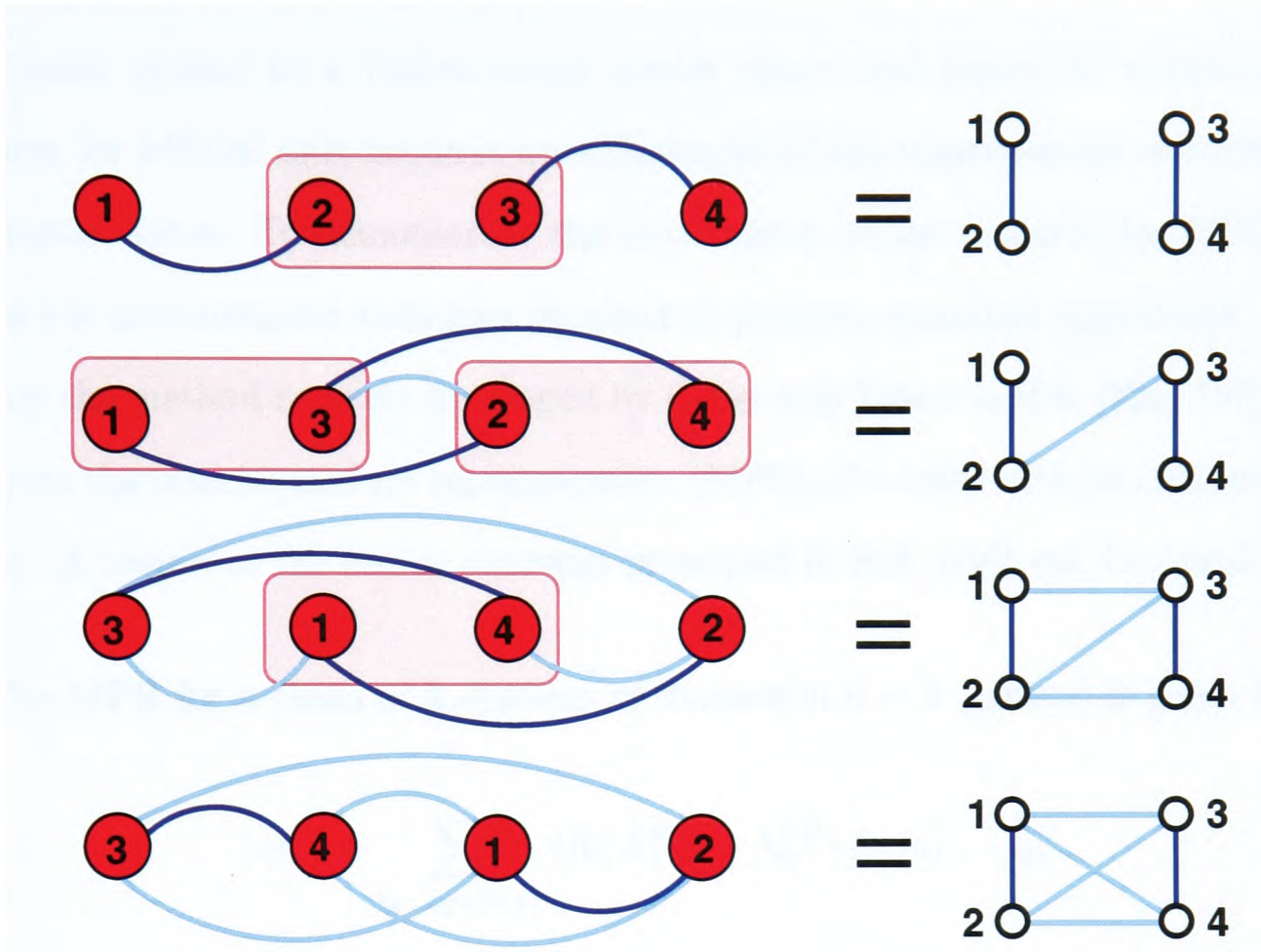


Figure 4.5. Schematic representations of the process leading to state (4.33). Qubits initially forming a Bell pair are linked by a dark blue line. The boxes depict the location where the $\sqrt{SWAP}^{\dagger} = SWAP\sqrt{SWAP}$ is performed. After a $\sqrt{SWAP}$ gate has been applied between two qubits, they are connected by a (light) blue line. Numerical calculations show that for up to 8 qubits, the state (4.33) is equivalent to a complete graph state under local unitary operations.

4.7 Creation of a resource for MBQC

In this section we will show how to create a state useful for MBQC via the application of the $\hat{C}_Z$ gate via lattice manipulations in both the x and y direction. This state is formally similar to a Bell-encoded cluster state, and hence its utilisation as a resource for MBQC only requires an adjustment of the measurement networks used for cluster states. To demonstrate the universality of our resource for MBQC and derive the measurement networks required to perform quantum algorithms, we will employ the method recently developed by Gross and Eisert in Ref. [126, 127], which connects the matrix product representation (MPR) of a state with its computational power. A review of the basics concepts presented in Ref. [126] can be found in 4.B.

The MPR for a chain of k systems of dimension $d = 2$ (qubits) is given by

$$|\psi_\Lambda\rangle = \sum_{i_1 \ldots i_k = \{0,1\}} \langle R| \hat{\Lambda}_1^{[i_1]} \cdots \hat{\Lambda}_k^{[i_k]} |L\rangle |i_1 \cdots i_k\rangle . \tag{4.34}$$

It is specified by a set of $2k$ $D \times D$-matrices, which we will refer to as the correlation matrices, and two D-dimensional vectors $|L\rangle$ and $|R\rangle$ representing boundary conditions. The parameter D is proportional to the amount of correlation between two consecutive blocks of the chain. Notice that the right boundary condition vector $|R\rangle$ appears on the left. This choice improves the clarity of calculations later when we will use the graphical notation explained in 4.B.2.

Starting from a lattice of Bell pairs, we find that the state resulting from the application of the gate $\hat{\mathcal{U}}^{\text{bw}}(\hat{C}_Z)$ on the state $\left|\Phi_k^{(0)}\right\rangle$ (4.14) has the MPS

$$|\psi_{AB}\rangle = \sum_{i_1 \ldots i_k = \{0,1\}} \langle R| \hat{A}^{[i_1]} \hat{B}^{[i_2]} \cdots \hat{A}^{[i_{k-1}]} \hat{B}^{[i_k]} |L\rangle |i_1 \cdots i_k\rangle , \tag{4.35}$$

where

$$\hat{A}^{[0]} = |+\rangle\langle 0|, \quad \hat{A}^{[1]} = |-\rangle\langle 1|, \tag{4.36}$$

$$\hat{B}^{[0]} = |1\rangle\langle 0|, \quad \hat{B}^{[1]} = |0\rangle\langle 1|, \tag{4.37}$$

$$|L\rangle = |+\rangle, \qquad |R\rangle = \sqrt{2}\,|0\rangle. \tag{4.38}$$

Here, each atom is labelled from 1 to k, and the correlation matrices $\hat{A}^{[0/1]}$ and $\hat{B}^{[0/1]}$ are associated with odd and even atoms, respectively. Equivalently, it can be written as

$$|\psi_C\rangle = \sum_{\bar{i}_1 \ldots \bar{i}_N = 0}^{1} \langle R|\hat{C}^{[\bar{i}_1]} \cdots \hat{C}^{[\bar{i}_N]}|L\rangle\, |\bar{i}_1 \cdots \bar{i}_N\rangle, \tag{4.39}$$

where

$$\begin{aligned} \hat{C}^{[\bar{0}]} &= \hat{A}^{[1]}\hat{B}^{[0]} = |-\rangle\langle 0| \\ \hat{C}^{[\bar{1}]} &= \hat{A}^{[0]}\hat{B}^{[1]} = |+\rangle\langle 1|, \end{aligned} \tag{4.40}$$

$$|\bar{0}\rangle = |10\rangle, \quad |\bar{1}\rangle = |01\rangle.$$

In this representation, each site is labelled from 1 to N and the correlation matrix $\hat{C}^{[\bar{0}/\bar{1}]}$ is associated with a pair of atoms. The measurement of odd and even atoms in the X-eigenbasis $\mathcal{B}_X = \{|\pm\rangle = (|0\rangle \pm |1\rangle)/\sqrt{2}\}$ on the state (4.35) projects the auxiliary matrix associated with the measured atom onto the eigenstate $(|0\rangle + (-1)^s|1\rangle)/\sqrt{2}$ depending on the measurement outcome s (see Eq. (4.69) in 4.B). In the graphical notation, this implements the operations

$$\rightarrow\boxed{A[X]}\rightarrow \quad \propto \hat{X}^s\hat{H}, \tag{4.41}$$

$$\rightarrow\boxed{B[X]}\rightarrow \quad \propto \hat{X}\hat{Z}^s, \tag{4.42}$$

for odd and even atoms, respectively. Here, the operator $\hat{H}$ is the Hadamard gate

and $\hat{X}$ the Pauli-X matrix [121]. Similarly, measurements in the ϕ-eigenbasis $\mathcal{B}_\phi = \{(|0\rangle \pm e^{i\phi}|1\rangle)/\sqrt{2}\}$ yield

$$\rightarrow\boxed{A[\phi]}\rightarrow \quad \propto \hat{X}^s \hat{H}\hat{S}(\phi), \tag{4.43}$$

$$\rightarrow\boxed{B[\phi]}\rightarrow \quad \propto \hat{X}\hat{Z}^s \hat{S}(\phi), \tag{4.44}$$

where $\hat{S}(\phi) = \mathrm{diag}(1, e^{i\phi})$ in the usual computational basis. Also, we find that since the measurement of the ith and $(i+1)$th atoms (i odd) in the Bell basis has only two possible outcomes, we have

$$\rightarrow\boxed{C[\bar{X}]}\rightarrow \quad \propto \hat{Z}\hat{X}^s \hat{H}, \tag{4.45}$$

$$\rightarrow\boxed{C[\bar{\phi}]}\rightarrow \quad \propto \hat{Z}\hat{X}^s \hat{H}\hat{S}(\phi), \tag{4.46}$$

where the measurement eigenbases are given by $\mathcal{B}_{\bar{X}} = \{(|\bar{0}\rangle \pm |\bar{1}\rangle)/\sqrt{2}\}$ and $\mathcal{B}_{\bar{\phi}} = \{(|\bar{0}\rangle \pm e^{i\phi}|\bar{1}\rangle)/\sqrt{2}\}$, respectively. Since any single-qubit gate can be decomposed into Euler angles, i.e.

$$\hat{U}_{\mathrm{rot}}(\zeta, \eta, \xi) = \hat{S}(\zeta)\hat{H}\hat{S}(\eta)\hat{H}\hat{S}(\xi), \tag{4.47}$$

the application of one of the following sequence of measurements

$$\rightarrow\boxed{\hat{B}[X_1]}\rightarrow\boxed{A[\phi_2]}\rightarrow\boxed{B[\phi_3]}\rightarrow\boxed{A[X_4]}\rightarrow\boxed{B[\phi_5]}\rightarrow\boxed{A[X_6]}\rightarrow, \tag{4.48}$$

$$\rightarrow\boxed{C[\bar{X}_1]}\rightarrow\boxed{C[\bar{\phi}_2]}\rightarrow\boxed{C[\bar{\phi}_3]}\rightarrow\boxed{C[\bar{\phi}_4]}\rightarrow \tag{4.49}$$

on the state (4.35) realise arbitrary qubit gates, up to a known by-product operator $\hat{U}_\Sigma$. For instance, applying the measurement sequence (4.48) with measurement outcomes $\vec{s} = (1, 0, 0, 0, 1, 1)$, where s_i denotes the outcome of X_i or ϕ_i, implements

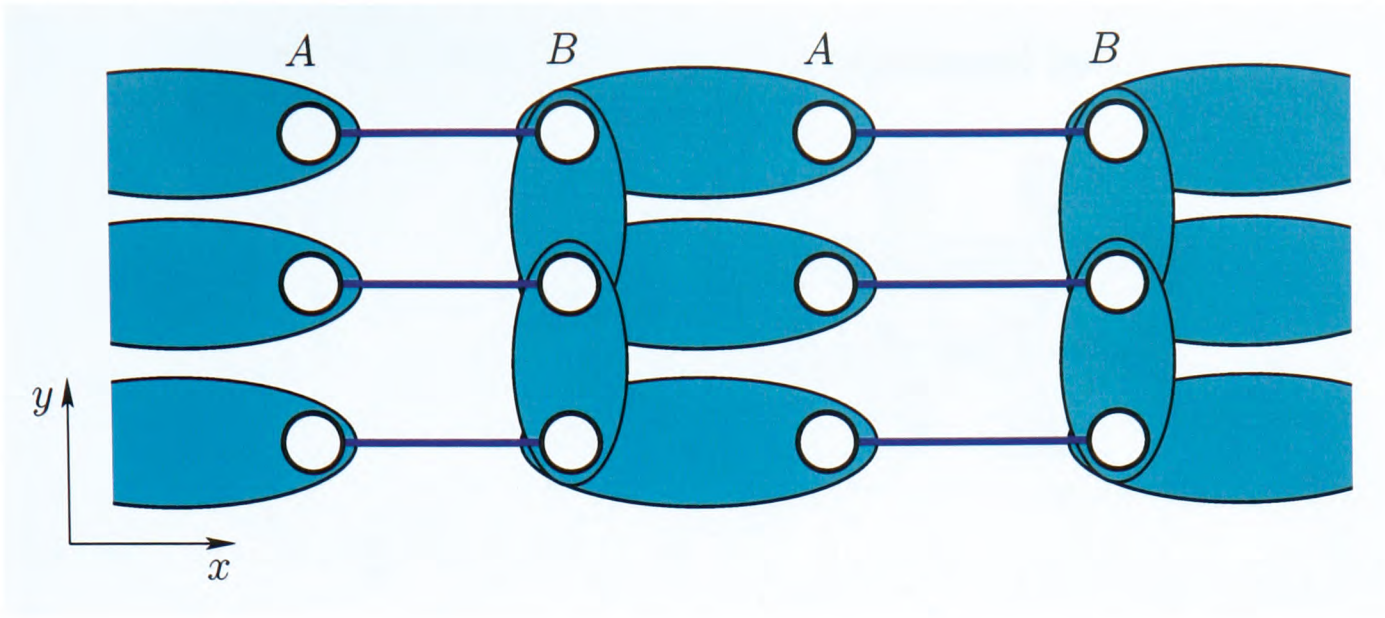


Figure 4.6. Starting with 1D system (x–direction) in the state (4.35), a 2D state useful for MBQC is obtained by applying $\hat{C}_Z$ gates between even subsites (denoted by the letter B) in the y–direction.

the operation $\hat{U}_\Sigma \hat{U}_{\rm rot}(\phi_2, \phi_3, \phi_5)$ with $\hat{U}_\Sigma = \hat{H}\hat{Z}\hat{X}$ on the state of the correlation space. Similarly, the measurement sequence (4.49) with outcomes $\vec{s} = (0, 0, 1, 0)$ implements the operation $\hat{U}_\Sigma \hat{U}_{\rm rot}(\phi_2, \phi_3, \phi_4)$ with $\hat{U}_\Sigma = \hat{Z}\hat{X}\hat{Z}$. Although both measurement sequences (4.48) and (4.49) preserve the system's immunity to collective dephasing, less measurements are required using the sequence (4.48). The state of the correlation space can be read-out using a scheme described in 4.B.

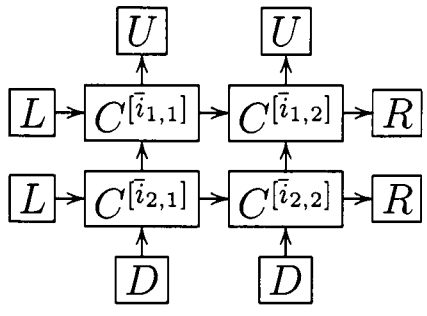
Superlattice manipulations can also be used to engineer 2D systems. In the remainder of this section, we will consider the MPR of the 2D state $|\psi_{2D}\rangle$ resulting from the coupling of 1D systems in the state (4.35) via the application of a $\hat{C}_Z$ gate between *even* subsites[2] in the y–direction (see Fig. 4.6). The MPR of this state is given by

$$\begin{array}{c} u \uparrow \\ r \rightarrow \boxed{C^{[0]}} \rightarrow l \\ d \uparrow \end{array} = |-\rangle_r \langle 0|_l \otimes |+\rangle_u \langle 0|_d \,, \tag{4.50}$$

$$\begin{array}{c} u \uparrow \\ r \rightarrow \boxed{C^{[1]}} \rightarrow l \\ d \uparrow \end{array} = |+\rangle_r \langle 1|_l \otimes |-\rangle_u \langle 1|_d \,. \tag{4.51}$$

[2]See e.g. Refs. [54, 55] for relevant 2D superlattice setups

Also, the expansion coefficients of $|\psi_{2D}\rangle$ are represented by

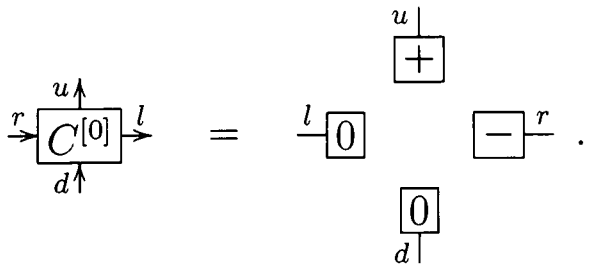
$$\langle \bar{i}_{1,1} \ldots \bar{i}_{2,2} \,|\, \psi_{2D} \rangle \quad = \quad \text{} \tag{4.52}$$

where $|U\rangle = |0\rangle$ and $|D\rangle = |+\rangle$.

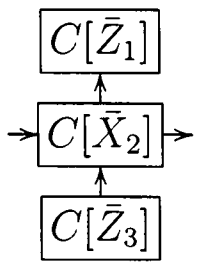
This state is formally similar to a cluster state where qubits are encoded on two atoms and the $|+\rangle$ state corresponds to the Bell state (4.13). Although the application of the $\hat{C}_Z$ gate between *sites* in the y–direction implements the same operation between *encoded qubits*, it corresponds to a *different* operation between encoded qubits in the x–direction. Therefore, it is not possible to execute algorithms designed for cluster states using the state $|\psi_{2D}\rangle$ as a resource by simply interchanging, e.g. X measurements with Bell-pair measurements $\bar{X}$.

In the remainder of this section, we will show that $|\psi_{2D}\rangle$ constitute a universal resource for MBQC by presenting how to control information flows through the lattice, and by providing a measurement network that implements an entangling two-qubit gate.

Since the tensors of Eqs. (4.50) and (4.51) factor, they can be represented graphically by

$$\text{} \tag{4.53}$$

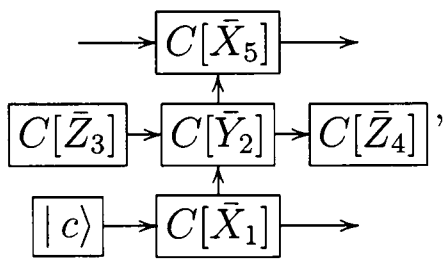
Using this representation and Eqs. (4.50) and (4.51), we find that



$$\propto \hat{X}\hat{Z}^{s_1+s_2+s_3}\hat{H}. \tag{4.54}$$

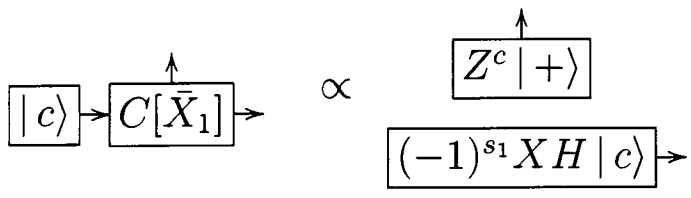
Thus, measurements in the basis $\mathcal{B}_{\bar{X}}$ cause the information to flow from left to right, and measurements of the vertically adjacent sites in the $\mathcal{B}_{\bar{Z}}$ basis shields the information from the rest of the lattice [126]. Since we can isolate horizontal lines, they can be used as logical qubits.

An entangling two-qubit gate between two horizontal lines is realised as follows. Consider the following measurement network [126]



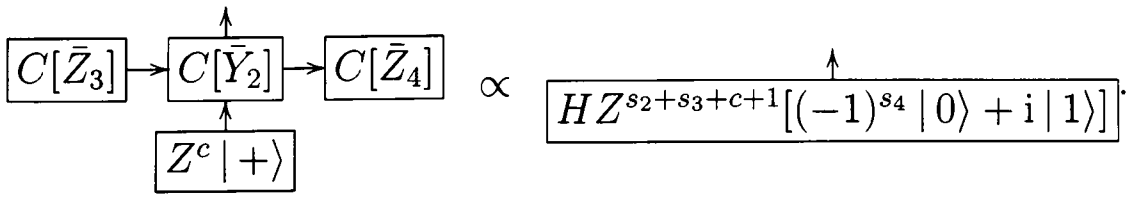
(4.55)

where the middle site is measured in the basis $\mathcal{B}_{\bar{Y}} = \{(|\bar{0}\rangle \pm \mathrm{i}\,|\bar{1}\rangle)/\sqrt{2}\}$ and $c \in \{0, 1\}$. The lower part of the network reduces to



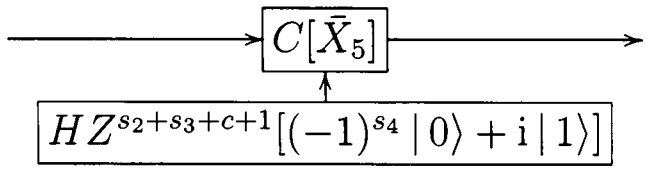
$$\propto \quad . \tag{4.56}$$

Plugging (4.56) into the middle line yields



$$\propto \quad . \tag{4.57}$$

Finally, plugging (4.57) into the upper of the network gives



$$\propto \hat{U}_\Sigma(-\mathrm{i}\hat{Z})^c \tag{4.58}$$

where $\hat{U}_\Sigma = \mathrm{e}^{\mathrm{i}\frac{\pi}{4}}(\mathrm{i}\hat{X})^{s_4}\hat{H}\hat{X}\hat{S}(\frac{\pi}{2})^\dagger\hat{Z}^{s_5}(-\mathrm{i}\hat{Z})^{s_2+s_3+1}$. Thus, the measurement network (4.55) implements an entangling controlled-phase gate between the upper and lower horizontal lines up to a know by-product operator. Since arbitrary single-qubit gates can be applied on each horizontal lines independently, this completes the proof of universality. The way of dealing with by-product operators at the end of the measurement sequences does not differ from the usual MBQC scheme with cluster states (see e.g. [115]). Notice that since single and two-qubit gates are performed via the application of pairwise measurements, the system remains invariant to collective dephasing at any time during the execution of an algorithm.

4.8 Summary

We have analysed the dynamics of a bosonic spinor condensate in a superlattice potential, and shown that a lattice with a Bell pair in every lattice site can be realised via the dynamical splitting of each site. We have proposed a scheme that allows the application of an entangling $\sqrt{\mathrm{SWAP}}$ gate between and inside Bell pairs. The successive application of this gate between and inside lattice sites was shown to create an entangled state with a tunable Schmidt rank that is resilient to collective dephasing noise; and a maximally entangled state which, as numerical evidence suggests, is locally equivalent to a GHZ state. Finally, we have presented a state that is obtained by connecting Bell pairs in two dimensions via an entangling phase gate, and shown that it constitutes a resource for MBQC formally similar to a Bell-encoded cluster state. We have provided measurement networks for implementing

a two-qubit entangling gate as well as arbitrary local unitary operations. Our implementation has the advantage that it allows the execution of quantum algorithms while leaving the system unaffected by collective dephasing noise.

Acknowledgements

This work was supported by the EU through the STREP project OLAQUI. The research was also supported by the EPSRC (UK) through the QIP IRC (GR/S82716/01) and EuroQUAM project EP/E041612/1. A. N. acknowledges a scholarship from the Rhodes Trust.

Appendix

4.A The full Hamiltonian

Using the field operator (4.7), the single-particle terms of the Hamiltonian (4.2) in second quantised form are given by

$$\begin{aligned}\hat{H}_0 &= \hat{H}_K + \hat{H}_Z \\ &= \sum_{\sigma=-1,0,1} \left[V_a + \Delta E_{Z,\sigma}(B)\right] \hat{a}_\sigma^\dagger \hat{a}_\sigma + \sum_{\sigma=-1,0,1} \left[V_b + \Delta E_{Z,\sigma}(B)\right] \hat{b}_\sigma^\dagger \hat{b}_\sigma,\end{aligned} \tag{4.59}$$

where $V_\nu = \int \mathrm{d}\mathbf{r}\, w_\nu^*(\mathbf{r}) \hat{h}_0\, w_\nu(\mathbf{r})$. Assuming that the magnetic field is weak ($B < 200\,\mathrm{G}$), the Zeeman shift $\Delta E_{Z,\sigma}(B)$ is accurately approximated to the second order in B [37]

$$\Delta E_{Z,\sigma}(B) = \begin{cases} \frac{g\mu_B B}{4} - \frac{3(g\mu_B B)^2}{16\Delta E_{\mathrm{hf}}} & \text{if } \sigma = -1, \\ -\frac{(g\mu_B B)^2}{4\Delta E_{\mathrm{hf}}} & \text{if } \sigma = 0, \\ -\frac{g\mu_B B}{4} - \frac{3(g\mu_B B)^2}{16\Delta E_{\mathrm{hf}}} & \text{if } \sigma = 1, \end{cases} \tag{4.60}$$

where g is the gyromagnetic factor, ΔE_{hf} is the hyperfine splitting energy, and μ_B is the Bohr magneton.

In the low-energy limit, atomic interactions are well approximated by s-wave scattering, with the scattering length depending on the spin state of the colliding atoms. At ultracold temperatures, two colliding atoms in the lower hyperfine level f_{low} will remain in the same multiplet, since the interaction process is not energetic enough to promote either atom to a higher hyperfine level f_{high} [110]. Also, since alkalis have only two hyperfine multiplets, the conservation of the total angular momentum by the scattering process implies that inter-atomic interactions conserve the hyperfine spin f_1 and f_2 of the individual atoms. Thus, the interaction between two particles located at positions $\mathbf{r}_1$ and $\mathbf{r}_2$ is given by [110, 117, 128]

$$\hat{V}_{\mathrm{int}}(\mathbf{r}_1 - \mathbf{r}_2) = \frac{4\pi\hbar^2}{M}\delta(\mathbf{r}_1 - \mathbf{r}_2)\sum_{F=0,2} a_F \hat{\mathscr{P}}_F, \tag{4.61}$$

where $F = f_1 + f_2$ is the total angular momentum of the scattered pair, $\hat{\mathscr{P}}_F$ is the projection operator for the total angular momentum F, and a_F is the s-wave scattering length of the channel associated with the total angular momentum F. The operator $\hat{\mathscr{P}}_F$ is given by [128]

$$\hat{\mathscr{P}}_F = \sum_{m_F=-F}^{F} |\, F, m_F\rangle \langle F, m_F \,|\,, \tag{4.62}$$

where $|\, F, m_F\rangle$ is the state formed by two atoms with total angular momentum F and $m_F = m_1 + m_2$ with m_1 and m_2 the projection on the quantisation axis of f_1 and f_2, respectively. The quantisation axis is defined by the direction of the magnetic field present in the system. Boson statistics require the state $|\, F, m_F\rangle$ to be invariant under particle exchange, and hence only the terms corresponding to values of $F = \{0, 2\}$ appear in the sum of Eq. (4.61). Using the relation $\hat{\mathbf{f}}_1 \cdot \hat{\mathbf{f}}_2 = \hat{\mathscr{P}}_2 - 2\hat{\mathscr{P}}_0$,

where $\hat{\mathbf{f}}_i = (\hat{f}_x^i, \hat{f}_y^i, \hat{f}_z^i)$ is the total angular momentum operator of the particle i, the interaction operator can be re-written as [110, 129]

$$\hat{V}_{\text{int}}(\mathbf{r}_1 - \mathbf{r}_2) = \delta(\mathbf{r}_1 - \mathbf{r}_2)\left(c_0 + c_2 \hat{\mathbf{f}}_1 \cdot \hat{\mathbf{f}}_2\right). \tag{4.63}$$

From Eq. (4.63) we see that interactions conserve the quantum number m_F [37, 130].

Using the field operator (4.7), the interaction term in second quantised form reads

$$\begin{aligned}\hat{H}_{\text{int}} = \frac{1}{2}\int\int \mathrm{d}\mathbf{r}_1 \mathrm{d}\mathbf{r}_2\, \delta(\mathbf{r}_1 - \mathbf{r}_2)\times \\ c_0 :\left(\hat{\mathbf{\Psi}}^\dagger(\mathbf{r}_1)\cdot\hat{\mathbf{\Psi}}(\mathbf{r}_1)\right)\left(\hat{\mathbf{\Psi}}^\dagger(\mathbf{r}_2)\cdot\hat{\mathbf{\Psi}}(\mathbf{r}_2)\right): \\ + c_2 \sum_{\ell=x,y,z} :\left(\hat{\mathbf{\Psi}}^\dagger(\mathbf{r}_1)\hat{f}_\ell^1\hat{\mathbf{\Psi}}(\mathbf{r}_1)\right)\left(\hat{\mathbf{\Psi}}^\dagger(\mathbf{r}_2)\hat{f}_\ell^2\hat{\mathbf{\Psi}}(\mathbf{r}_2)\right):,\end{aligned} \tag{4.64}$$

where $:\hat{o}:$ represents the operator $\hat{o}$ in normal ordering, $\hat{\mathbf{\Psi}}(\mathbf{r}) = (\hat{\Psi}_{-1}(\mathbf{r}), \hat{\Psi}_0(\mathbf{r}), \hat{\Psi}_1(\mathbf{r}))$ and the matrices $\hat{f}_\ell$ are given by [118]

$$\hat{f}_x^i = \frac{1}{\sqrt{2}}\begin{pmatrix}0&1&0\\1&0&1\\0&1&0\end{pmatrix}, \hat{f}_y^i = \frac{1}{\sqrt{2}\mathrm{i}}\begin{pmatrix}0&1&0\\-1&0&1\\0&-1&0\end{pmatrix}, \hat{f}_z^i = \begin{pmatrix}1&0&0\\0&0&0\\0&0&-1\end{pmatrix}. \tag{4.65}$$

The Hamiltonian given in (4.5) is a compact form of (4.64). In its expanded form,

Eq. (4.64) reads [129]

$$\begin{aligned}\hat{H}_{\text{int}} =& \frac{1}{2}\int \mathrm{d}\mathbf{r}\times \\ & \Big\{(c_0+c_2)\left[\hat{\Psi}_1^\dagger(\mathbf{r})\hat{\Psi}_1^\dagger(\mathbf{r})\hat{\Psi}_1(\mathbf{r})\hat{\Psi}_1(\mathbf{r})+\hat{\Psi}_{-1}^\dagger(\mathbf{r})\hat{\Psi}_{-1}^\dagger(\mathbf{r})\hat{\Psi}_{-1}(\mathbf{r})\hat{\Psi}_{-1}(\mathbf{r})\right] \\ & +2(c_0+c_2)\left[\hat{\Psi}_1^\dagger(\mathbf{r})\hat{\Psi}_0^\dagger(\mathbf{r})\hat{\Psi}_1(\mathbf{r})\hat{\Psi}_0(\mathbf{r})+\hat{\Psi}_{-1}^\dagger(\mathbf{r})\hat{\Psi}_0^\dagger(\mathbf{r})\hat{\Psi}_{-1}(\mathbf{r})\hat{\Psi}_0(\mathbf{r})\right] \\ & +2c_2\left[\hat{\Psi}_0^\dagger(\mathbf{r})\hat{\Psi}_0^\dagger(\mathbf{r})\hat{\Psi}_1(\mathbf{r})\hat{\Psi}_{-1}(\mathbf{r})+\hat{\Psi}_1^\dagger(\mathbf{r})\hat{\Psi}_{-1}^\dagger(\mathbf{r})\hat{\Psi}_0(\mathbf{r})\hat{\Psi}_0(\mathbf{r})\right] \\ & +c_0\left[\hat{\Psi}_0^\dagger(\mathbf{r})\hat{\Psi}_0^\dagger(\mathbf{r})\hat{\Psi}_0(\mathbf{r})\hat{\Psi}_0(\mathbf{r})\right] \\ & +2(c_0-c_2)\left[\hat{\Psi}_1^\dagger(\mathbf{r})\hat{\Psi}_{-1}^\dagger(\mathbf{r})\hat{\Psi}_1(\mathbf{r})\hat{\Psi}_{-1}(\mathbf{r})\right]\Big\}. \end{aligned} \tag{4.66}$$

The interaction Hamiltonian (4.66) can be expressed in terms of $\hat{a}_\sigma^\dagger$ and $\hat{b}_\sigma^\dagger$ operators using the relation

$$\begin{aligned}\frac{1}{2}\int \mathrm{d}\mathbf{r}\,\hat{\Psi}_\sigma^\dagger(\mathbf{r})\hat{\Psi}_\gamma^\dagger(\mathbf{r})\hat{\Psi}_{\sigma'}(\mathbf{r})\hat{\Psi}_{\gamma'}(\mathbf{r}) &= \frac{U_{aa}}{2}\left(\hat{a}_\sigma^\dagger\hat{a}_\gamma^\dagger\hat{a}_{\sigma'}\hat{a}_{\gamma'}\right)+\frac{U_{bb}}{2}\left(\hat{b}_\sigma^\dagger\hat{b}_\gamma^\dagger\hat{b}_{\sigma'}\hat{b}_{\gamma'}\right)+ \\ \frac{U_{ab}}{2}\left(\hat{a}_\sigma^\dagger\hat{a}_\gamma^\dagger\hat{b}_{\sigma'}\hat{b}_{\gamma'}+\hat{b}_\sigma^\dagger\hat{b}_\gamma^\dagger\hat{a}_{\sigma'}\hat{a}_{\gamma'}\right)&+\frac{U_{ab}}{2}\left(\hat{a}_\sigma^\dagger\hat{b}_\gamma^\dagger+\hat{b}_\sigma^\dagger\hat{a}_\gamma^\dagger\right)\left(\hat{a}_{\sigma'}\hat{b}_{\gamma'}+\hat{b}_{\sigma'}\hat{a}_{\gamma'}\right), \end{aligned} \tag{4.67}$$

where $U_{\nu\nu'}=\int \mathrm{d}\mathbf{r}\,(|w_\nu(\mathbf{r})||w_{\nu'}(\mathbf{r})|)^2$ and $\sigma,\gamma=-1,0,+1$.

4.B Measurement-based quantum computations and MPSs

4.B.1 General idea

In this section, we present the general idea developed in Ref. [127]. From Eq. (4.34), one can see that if the i_k site in the computational basis and the outcome s_k is

obtained, then the state $|\, L\rangle$ of the auxiliary system becomes

$$|\, L\rangle' = \hat{\Lambda}_k^{[s_k]} \,|\, L\rangle\,. \tag{4.68}$$

Thus, measurements change the state $|\, L\rangle$ of the auxiliary system. Similarly, if the measurement of a local observable at site k yields an outcome corresponding to the observable's eigenvector $|\, \phi_k\rangle$, then the matrix $\hat{\Lambda}_k^{[i_k]}$ transforms into

$$\hat{\Lambda}[\phi]_k = \langle\, \phi_k \,|\, 0 \,\rangle\, \hat{\Lambda}_k^{[0]} + \langle\, \phi_k \,|\, 1 \,\rangle\, \hat{\Lambda}_k^{[1]}, \tag{4.69}$$

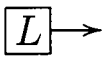
and the vector of the auxiliary system becomes

$$|\, L\rangle' = \hat{\Lambda}[\phi]_k \,|\, L\rangle\,. \tag{4.70}$$

From this point of view, a measurement on some physical site change the correlation properties between this site and the rest of the chain, i.e. it performs an operation on the auxiliary system state $|\, L\rangle$, which we will sometimes refer to as the state of the correlation space.

4.B.2 Graphical notation

In order to deal with the MPS of higher-dimensional states, the graphical notation introduced in Ref. [127] is very helpful. In this notation, tensors are represented by boxes, and their indices by edges. Vectors and matrices are thus symbolised by

$|\, L\rangle$ =  , (4.71)

$\langle R\,|$ =  , (4.72)

$\hat{\Lambda}^{[i]}$ =  . (4.73)

Consequently, vector and matrix operations can be represented graphically by

$$\langle R|L\rangle \;=\; \boxed{L}\!-\!\boxed{R}\;, \tag{4.74}$$

$$\hat{B}\hat{A} \;=\; \rightarrow\boxed{A}\rightarrow\boxed{B}\rightarrow\;, \tag{4.75}$$

$$\hat{B}\hat{A}|L\rangle \;=\; \boxed{L}\rightarrow\boxed{A}\rightarrow\boxed{B}\rightarrow\;. \tag{4.76}$$

4.B.3 Read-out scheme

In order to use the state of the correlation space to process quantum information, we must be able to read it out at the end of the computation. It turns out that in our case a measurement of the $(i-1)$th site in the computational basis corresponds to a measurement of the correlation system just after the ith site. To illustrate this fact, assume that just after the measurement of the ith site, the correlation system is in the state $|0\rangle$, that is

$$\boxed{L}\rightarrow\boxed{B[\phi_1]}\rightarrow\boxed{A[\phi_2]}\rightarrow\cdots\quad\boxed{B[\phi_i]}\rightarrow\quad=|0\rangle\,, \tag{4.77}$$

or

$$\boxed{L}\rightarrow\boxed{B[\phi_1]}\rightarrow\boxed{A[\phi_2]}\rightarrow\cdots\quad\boxed{A[\phi_i]}\rightarrow\quad=|0\rangle\,. \tag{4.78}$$

Thus, using Eqs. (4.36) and (4.37) we have

$$\boxed{|0\rangle}\rightarrow\boxed{A[1]}\rightarrow\;\propto|-\rangle\langle 1|0\rangle\;=\;0, \tag{4.79}$$

$$\boxed{|0\rangle}\rightarrow\boxed{B[1]}\rightarrow\;\propto|0\rangle\langle 1|0\rangle\;=\;0. \tag{4.80}$$

Hence, the probability of obtaining the result 1 for a measurement on the $(i-1)$th site is zero. Consequently, if the state of the correlation system is in state $|0\rangle$ after

the ith site, then the $(i-1)$th physical site must also be in that state. Since

$$\boxed{|\,0\rangle} \longrightarrow \boxed{C[1]} \longrightarrow \quad \propto |\,+\rangle\,\langle\,1\,|\,0\,\rangle = 0, \tag{4.81}$$

the same observation applies if one measures the $(i-2)$th and $(i-1)$th sites (i odd) in the basis $\mathcal{B}_{\bar{Z}} = \{|\,\bar{0}\rangle\,, |\,\bar{1}\rangle\}$. Therefore, as a similar argument applies if the state of the correlation system is in the state $|\,1\rangle$ after the ith site, the description of the read-out scheme is complete.

Chapter 5

Long-range molecular potentials

5.1 Introduction

The manipulation of ultracold molecules is currently a very actively researched topic in atomic physics. Molecules often have very rich energy level structures, and they can be sensitive to very small changes in their environment so that their creation and manipulation find applications in many fields, such as high-precision measurements, high-resolution spectroscopy, or even quantum computation.

Molecules are notably hard to cool to very low temperatures, and so it is often advantageous to create them from already ultracold atoms (see e.g. Refs. [17] and references therein). In this context, optical lattices offer many interesting opportunities to form and study the properties of such molecules. The optical lattice allows molecules to be isolated from each other, and shields them from detrimental collisions that would usually take place in a gas.

So far, the main approach towards creating molecules in optical lattices has consisted of initialising the lattice in a Mott-insulating state with two atoms per site, and then transforming each pair into a dimer via the use of Feshbach resonances (see e.g. Refs. [24, 131–133], or photo-association (see e.g. Ref [134]). These two techniques can also be combined, e.g. to increase the binding energy of Feshbach

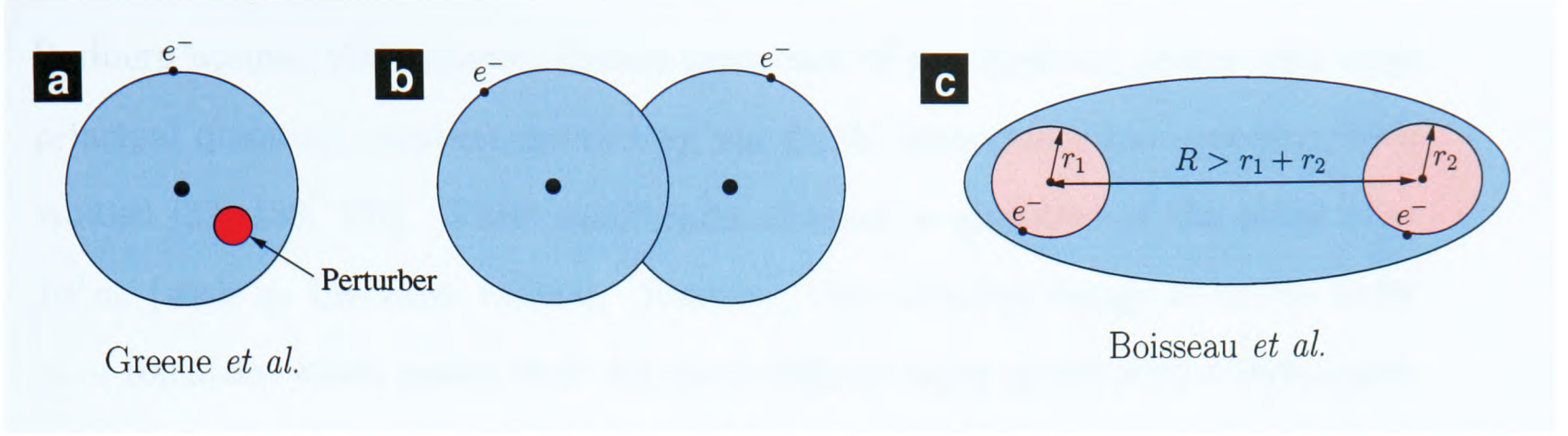


Figure 5.1. Representation of the different types of long-range molecules. (a) A Rydberg atom perturbed by a ground-state atom (see Ref. [25]); (b) Two Rydberg atoms with a little overlap between the two, as will be discussed in the next chapter; (c) Two Rydberg atoms separated by a large distance that interact via dipole forces

molecules [132]. The different types of molecules produced in this fashion have binding energies of the order of a few tens of MHz, and lifetimes up to 700 ms [131, 134]. Also, the spatial extent of the molecules that have so far been produced in optical lattices is usually much smaller than the distance between two lattice sites.

In the next chapter, we investigate the properties of ultracold dimers composed of highly-excited atoms that have very large spatial dimensions. The interest in ultracold molecules of macroscopic dimensions was sparked by an article from Greene *et al.* [25], where the existence of macroscopic dimer molecules was predicted. These molecules are composed by one atom in the ground state, and the other one in a highly-excited Rydberg state (see Fig. 5.1a). They have a size of about 70 nm, which corresponds to the dimension of a bacterium, and have recently been observed in a gas of ultracold atoms [25, 26, 135]. These molecules have the peculiarity that their electronic cloud resembles a trilobite insect; they also possess a large permanent dipole moment, which could potentially facilitate their manipulation. Their binding energies range between 100 MHz–10 GHz, and their estimated lifetime is of the order of a few tens of microseconds.

There exist other types of long-range dimers that can be formed from ultracold

Rydberg atoms. For instance, dimers composed of two Rydberg atoms with large principal quantum numbers interacting via dipole interactions have recently been studied [27, 136, 137]. Their equilibrium distance is gigantic—of the order of $\sim 10^4\, a_0$ (with a_0 the Bohr radius). However, their binding energy is of the order of $\sim 100\,\mathrm{MHz}$, which makes their detection difficult using spectroscopic techniques. The equilibrium distance of these molecules is sufficiently large so that the electronic clouds of the two atoms do not overlap, and hence they interact mainly via dipole-dipole interactions (see Fig. 5.1c).

In the context of the creation and observation of long-range dimers, optical lattices offer very interesting features. They can not only be used to isolate atomic pairs from each other, but also to fix the initial position of the atoms before they are photo-associated. In order to take advantage of these features, we will investigate the existence of diatomic molecular potentials with equilibrium distances of the order of typical lattice spacings in the next chapter. These molecules interact via coulombic interactions, and so they have binding energies greater than those of previously studied long-range molecules, which makes them potentially easier to observe using standard spectroscopic techniques (see Fig.5.1b). Techniques developed in the context of high-resolution spectroscopy for Rydberg atoms excited from Bose-Einstein condensates may provide a basis for the measurement of the energy of such molecules (see e.g. Ref. [138]).

In this chapter, we introduce basic elements of molecular quantum mechanics[1] concerned with the calculation of the potential curves of diatomic molecules. We also discuss the limitations of certain approximations of the coulombic potential for evaluating long-range molecular potentials between Rydberg atoms, and motivate the approach taken in the next chapter.

[1]The aim of this introduction is to make the content of the next chapter accessible to an audience with a background in atomic and laser physics.

5.2 General framework

Most calculations in molecular quantum mechanics are done in the framework of the Born-Oppenheimer approximation, that is assuming that electrons can adjust their position almost instantaneously to that of the nuclei, so that the latter can be considered as fixed. Thus, the energy of a molecule is given by the solutions of the Schrödinger equation for a collection of electrons moving in the field generated by the nuclei.

Apart from the simple case of ion-molecules, where one electron is shared by two nuclei, exact numerical, let alone analytical, solutions of the Schrödinger equation are very hard to obtain. The general approach is to build up a trial molecular wavefunction for the molecule and to optimise its energy using variational methods. For diatomic molecules, the most important quantities to evaluate are the potential depth, which corresponds to the minima of the molecular potential, and the equilibrium distance, which is the distance between the atoms for which the potential is at its minimum [139].

5.3 The ion-molecule

In order to introduce some notation and illustrate the different methods used to approximate molecular orbitals, we start with the simplest possible molecular compound, the ion-molecule. An ion-molecule is formed by an electron and two ions. The Hamiltonian describing the system is given by

$$H(R) = -\frac{\hbar^2}{2M}\nabla_r^2 + j_0[\frac{1}{R} - \frac{1}{r_A} - \frac{1}{r_B}], \tag{5.1}$$

where $\mathbf{r}$ is the position of the electron, $j_0 = e^2/(4\pi\varepsilon_0)$, r_ξ is the distance between the electron and the atomic centre $\xi = A, B$, ε_0 is the permittivity in free space,

and R the distance between the nuclei.

Even for the simplest case of two ions A and B and one electron (e.g. H_2^+ or Rb_2^+), it is not possible to find analytical solutions to the Schrödinger equation. Following the common approach, the energy of this simple molecular compound is evaluated by approximating its wavefunction using a superposition of the electronic orbitals of the parent atoms. This procedure is called linear combination of atomic orbitals (LCAO). For instance, the ground-state wavefunction of the H_2^+ ion-molecule can be approximated by a simple combination of two orbitals

$$\Psi(\mathbf{r}, R)_{\mathbf{q}} = c_a A_{\mathbf{q}}(\mathbf{r}) + c_b B_{\mathbf{q}}(\mathbf{r}), \tag{5.2}$$

where $A_{\mathbf{q}}(\mathbf{r})$ $[B_{\mathbf{q}}(\mathbf{r})]$ is the hydrogenic wavefunction with quantum numbers $\mathbf{q} = (n, \ell, m)$—e.g. $\mathbf{q} = (1, 0, 0)$ for hydrogen—centred on the ion A (B). The coefficients c_a and c_b are determined using variational principles, which leads to an energy

$$E_{\pm} = \frac{\alpha_{\mathbf{q}\mathbf{q}'} \pm \beta_{\mathbf{q}\mathbf{q}'}}{1 \pm S_{\mathbf{q}\mathbf{q}'}}, \tag{5.3}$$

where for hydrogen $\mathbf{q} = \mathbf{q}' = (1, 0, 0)$. The quantity $\alpha_{\mathbf{q}\mathbf{q}'}$ is known as the Coulomb integral, $\beta_{\mathbf{q}\mathbf{q}'}$ as the resonance integral and $S_{\mathbf{q},\mathbf{q}'} = \int d\mathbf{r}\, \mathrm{A}^*_{\mathbf{q}}(\mathbf{r})\mathrm{B}_{\mathbf{q}'}(\mathbf{r})$ is the overlap integral. The Coulomb integral is given by $\alpha_{\mathbf{q},\mathbf{q}'} = E_{\mathbf{q}} + (j_0/R) - J_{\mathbf{q},\mathbf{q}'}$ where $J_{\mathbf{q},\mathbf{q}'} = j_0 \int d\mathbf{r}\, \mathrm{B}^*_{\mathbf{q}}(\mathbf{r})(1/r_A)\mathrm{B}_{\mathbf{q}'}(\mathbf{r})$, and $E_{\mathbf{q}}$ is the energy of the unperturbed atom with quantum $\mathbf{q}$. The resonance integral is given by $\beta_{\mathbf{q},\mathbf{q}'} = [E_{\mathbf{q}} + (j_0/R)]S_{\mathbf{q},\mathbf{q}'} - K_{\mathbf{q},\mathbf{q}'}$ with $K_{q,q'} = j_0 \int d\mathbf{r}\, \mathrm{A}^*_q(\mathbf{r})(1/r_B)\mathrm{B}_{q'}(\mathbf{r})$.

The energy E_+ is associated with a wavefunction Ψ^+ with coefficients $c_a = c_b$ where $c_a = 1/\sqrt{2(1 + S_{\mathbf{q},\mathbf{q}'})}$ and E_- to Ψ^- with coefficients $c_a = -c_b$ where $c_a = 1/\sqrt{2(1 - S_{\mathbf{q},\mathbf{q}'})}$. The trial wavefunction (5.2) has an equilibrium position and depth precise to within 20% of the experimental values. This result can be improved by

adding more orbitals in the definition (5.2) in order to enhance the shape of the molecular wavefunction.

A chemical bond is often interpreted as a decrease of potential energy caused by the accumulation of electronic density in the inter-atomic region, and so the purpose of adding more basis state to the molecular orbital is to increase this density while keeping the overall energy as low as possible.

Under inversion of the electron coordinates, the function Ψ^+ is left unchanged, and so it is said to be *gerade*. On the other hand, Ψ^- changes sign, and so it is said to be *ungerade*. Both of these two functions have rotational symmetry around the internuclear axis, and are called σ-orbitals, by analogy with the letter s of the atomic angular momentum. The two wavefunctions Ψ^+ and Ψ^- are thus denoted by σ_g and σ_u, respectively. Taking the z-direction to be the internuclear axis, single-electron molecular wavefunctions made out of e.g. s, p_z or d_{z^2} atomic orbitals are denoted by the letter σ, which corresponds to a zero angular momentum with respect to the inter-atomic axis.

5.4 Homonuclear diatomic molecules

The Hamiltonian of a dimer molecule composed of two identical atoms sharing two electrons (e.g. H_2 or Rb_2) is given by

$$\begin{aligned} H(R) = &-\frac{\hbar^2}{2M}\left(\nabla^2_{\mathbf{r_1}} + \nabla^2_{\mathbf{r_2}}\right) - j_0\left(\frac{1}{r_{1A}} + \frac{1}{r_{2B}}\right) \\ &+ j_0\left(\frac{1}{R} + \frac{1}{r_{12}} - \frac{1}{r_{1B}} - \frac{1}{r_{2A}}\right), \end{aligned} \tag{5.4}$$

where $r_{\gamma,\xi}$ with $\gamma = 1, 2$ is the distance between the electron γ and the atomic centres ξ, $\mathbf{r}_\gamma$ is the coordinate of the electron γ, and r_{12} is the distance between the two electrons. The terms of the second line correspond to the interactions between the

two atoms.

There are principally two different approaches to the approximation of the molecular wavefunctions of dimer molecules; the molecular-orbital method, and the valence-bond method (see e.g. Refs [139, 140]). The two approaches differ mainly in the way that they treat the ionic nature of the chemical bond.

5.4.1 The molecular-orbital method

The molecular wavefunction of a dimer is obtained using the molecular-orbital method by simply multiplying two single-electron molecular orbitals. This yields e.g. for H_2

$$\sigma_g(\mathbf{r_1})\sigma_g(\mathbf{r_2}) = \frac{1}{2(1+S_{100,100})}[\underbrace{A_{100}(\mathbf{r_1})A_{100}(\mathbf{r_2}) + B_{100}(\mathbf{r_1})B_{100}(\mathbf{r_2})}_{\text{Ionic part}} + \underbrace{A_{100}(\mathbf{r_1})B_{100}(\mathbf{r_2}) + A_{100}(\mathbf{r_2})B_{100}(\mathbf{r_1})}_{\text{Valence part}}]. \quad (5.5)$$

This wavefunction has two parts. The first represents the two electrons being located on the same nucleus; the mechanism at the heart of ionic bond. The second represents the two electrons being equally shared between the two atoms, thus forming a so-called valence bond. Note that the superposition of two ungerade molecular orbitals would produce a similar wavefunction with a negative sign in front of the valence part.

If we consider σ-orbitals, there are four ways to accommodate the two electrons. The two combinations $\sigma_g \times \sigma_g$, and $\sigma_u \times \sigma_u$ generate a molecular wavefunction of gerade symmetry, and $\sigma_u \times \sigma_g$, and $\sigma_g \times \sigma_u$ of ungerade symmetry. Gerade states have singlet spin states, and ungerade states triplet states. Also, the rotational symmetry around the internuclear axis is zero because both electrons occupy a σ-orbital. Consequently, the symmetry of the molecule is denoted by $^1\Sigma_g$ for gerade combi-

nations, and ${}^3\Sigma_u$ for ungerade combinations. The capital Greek letter Σ indicates the total angular momentum of the molecular wavefunction about the internuclear axis; it is associated with the values $\Sigma = 0$, $\Pi = 1$, $\Delta = 2$, etc., in an echo of atomic notation. The Hamiltonian (5.4) has no non-diagonal matrix elements between two functions of different symmetry type. This includes different components of the angular momentum around the internuclear axis, different parity, and different signs under coordinate inversion.

The energy of the dimer is obtained by diagonalising the Hamiltonian (5.4) using basis sets formed by different combinations of single-electron orbitals. It involves the calculation of integrals over the coordinates of the two electrons, which are notably difficult to evaluate. Owing to the computational difficulty of calculating these integrals for arbitrary quantum numbers, the basis set of orbitals used in (5.2) are often Slater-type orbitals, or Gaussian-type orbitals. They are simpler to integrate than hydrogenic wavefunctions, and can be parametrised to further optimise the solutions. Also, for molecules involving electrons in low-lying states, they allow the approximation of the molecular wavefunction with relatively few terms.

5.4.2 Valence bond approach

Another common approach used to approximate the molecular wavefunction of dimers is the valence bond method. This approach neglects entirely the contribution of the ionic part when building the wavefunction of the two electrons.

If we consider two electrons with quantum numbers $\mathbf{q}$ and $\mathbf{q}'$ separated by a large distance, their wavefunction is proportional to $\psi^{(0)}_{\mathbf{q},\mathbf{q}'} = A_{\mathbf{q}}(\mathbf{r_1})B_{\mathbf{q}'}(\mathbf{r_2})$, which corresponds to the wavefunction of the unperturbed system. The calculation of the average of the Hamiltonian using this function corresponds to the calculation of the first-order correction to the energy of the unperturbed system. When the two

electrons come closer, as is the case in the H_2 molecule, for instance, it provides a very poor approximation of the potential depth, and an equilibrium distance within 20% of the experimental value.

However, these results can be greatly enhanced by adding an exchange part to this zeroth order wavefunction. By taking the linear combination

$$\psi^{\pm}_{\mathbf{q},\mathbf{q}'}(\mathbf{r_1},\mathbf{r_2}) = \frac{1}{\sqrt{2}}[A_{\mathbf{q}}(\mathbf{r_1})B_{\mathbf{q}'}(\mathbf{r_2}) \pm A_{\mathbf{q}}(\mathbf{r_2})B_{\mathbf{q}'}(\mathbf{r_1})] \tag{5.6}$$

as a trial molecular wavefunction, the equilibrium value and depth of the molecular potential become more accurate. This wavefunction describes a system where the electrons spend half of their time around one nucleus, and the second half around the other nucleus (the valence term).

The calculation of the molecular potential by taking the average of the Hamiltonian (5.4) is known as the Heitler-London method. Using the wavefunction (5.6) yields a molecular potential of the form

$$E^{VB,\pm}_{\mathbf{q},\mathbf{q}'} = E_{\mathbf{q}} + E_{\mathbf{q}'} + \frac{j_0}{R} + \frac{C_{\mathbf{q},\mathbf{q}'} \pm X_{\mathbf{q},\mathbf{q}'}}{(1 \pm |S_{\mathbf{q},\mathbf{q}'}|^2)}, \tag{5.7}$$

where $C_{\mathbf{q},\mathbf{q}'} = [A_{\mathbf{q}}A_{\mathbf{q}}|B_{\mathbf{q}'}B_{\mathbf{q}'}] - (J_{\mathbf{q},\mathbf{q}} + J_{\mathbf{q}',\mathbf{q}'})$, and $X_{\mathbf{q},\mathbf{q}'} = [A_{\mathbf{q}}B_{\mathbf{q}'}|A_{\mathbf{q}}B_{\mathbf{q}'}] - S_{\mathbf{q},\mathbf{q}'}[K_{\mathbf{q},\mathbf{q}'} + K_{\mathbf{q}',\mathbf{q}}]$ with

$$[\alpha\beta|\gamma\nu] = j_0 \int\int dr_1\, dr_2\, \alpha^*(\mathbf{r}_1)\beta(\mathbf{r}_1)\frac{1}{r_{12}}\gamma^*(\mathbf{r}_2)\nu(\mathbf{r}_2). \tag{5.8}$$

The exchange integrals come as a result of the addition of the valence terms to the definition of the molecular wavefunction. For the hydrogen molecule, the equilibrium distance found with the Heitler-London method is accurate to within $< 1\%$ and the potential depth to within $< 5\%$ compared to experimental values [140]. Compared to the molecular-orbital approach, the valence bond approach produces slightly shallower potentials (of the order of a few percent). However, the potentials

obtained in this way behave better in the long-range than those obtained using the molecular orbital method.

The term $E^{(1)}_{\mathbf{q},\mathbf{q}'} = (j_0/R) + C_{\mathbf{q},\mathbf{q}'}$ corresponds to the first-order correction to the energy of the unperturbed Hamiltonian. Thus, the Heitler-London method reduces to the calculation of the first-order correction to the unperturbed energy of the atoms when exchange interactions become small.

When the two atoms are sufficiently far apart so that their wavefunction is unlikely to have large contributions from the ionic part, the valence bond picture is the most appropriate. The symmetry of the valence wavefunctions can be found by recasting them in terms of molecular orbitals. For instance, the state $\psi^{-}_{100,100} = [\sigma_g(\mathbf{r_1})\sigma_u(\mathbf{r_2}) - \sigma_u(\mathbf{r_1})\sigma_g(\mathbf{r_2})]$, and hence is denoted by the $^3\Sigma^+_u$ symbol, where the $+$ sign indicates the symmetry with respect to reflection in a plane which contains both nuclei. Similarly, the state $\psi^{(0)}_{n10,n10}$ is said to have a $^1\Sigma^+_g - ^3\Sigma^+_u$ symmetry.

5.5 Long-range interactions

Consider a charged particle with coordinates $(r_{1A}, \theta_1, \phi_1)$ with origin located at A and another with coordinates $(r_{2B}, \theta_1, \phi_1)$ with origin located at B, where θ_γ is the angle between the inter-particle axis, and ϕ_γ the azimuthal angle. When the two centres A and B are separated by a distance R such that $r_{1A} + r_{2B} < R$, the coulombic interaction $1/r_{12}$ between these two particles can be written in the form

$$V_{\text{multi}}(R, \mathbf{r}_{1A}, \mathbf{r}_{2B}) = \frac{e_1 e_2}{4\pi\varepsilon_0} \sum_{n_1,n_2=0}^{\infty} \sum_{m=-n_<}^{n_<} \frac{(-1)^{n_1+|m|}(n_1+n_2)!}{(n_1+|m|)!(n_2+|m|)!} r_{1A}^{n_1} r_{2B}^{n_1} R^{-n_1-n_2-1} \times P_{n_1}^{|m|}(\cos\theta_1) P_{n_2}^{|m|}(\cos\theta_2) \mathrm{e}^{\mathrm{i}m(\phi_1-\phi_2)}, \tag{5.9}$$

where e_i is the charge of the particle i, ε_0 is the electrical permittivity of free space, $n_< = \min(n_1, n_2)$, and $P_n^m(\cos\theta)$ is an associated Legendre polynomial [141, 142].

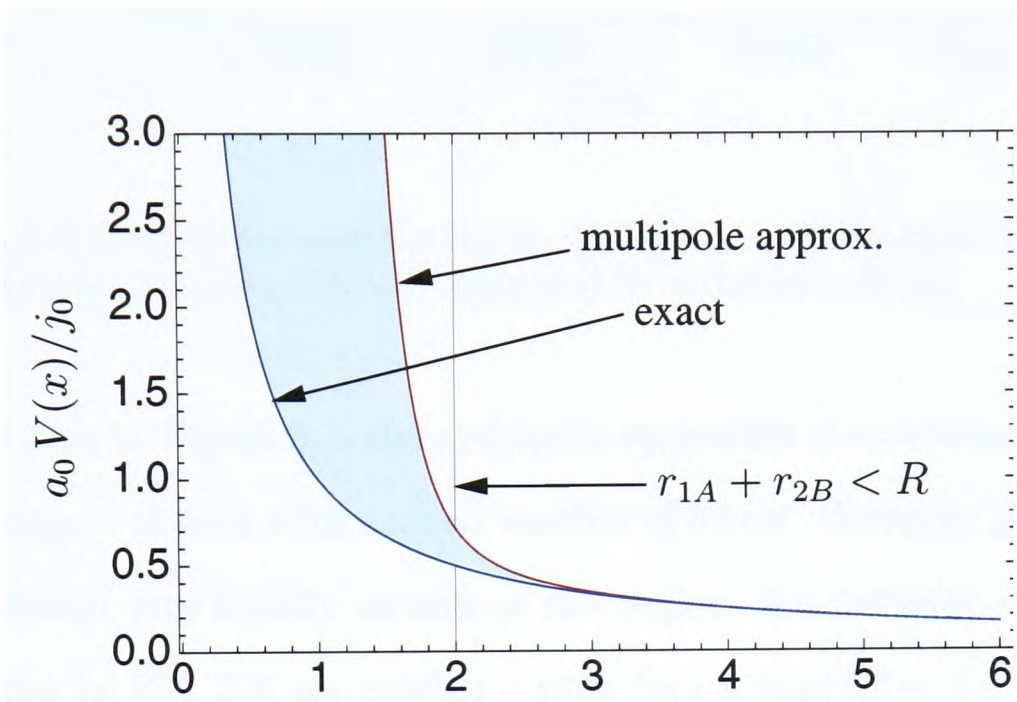


Figure 5.2. Comparison of the multipole expansion of the coulombic potential including terms up to R^{-9} with its exact form $V(x) = j_0/x$ between two electrons. The first and second electrons have coordinates $(r_{1A}, 0)$ and $(r_{2B}, 0)$ (with $r_{2B} = r_{1A} = 1$) from centre A and B, respectively. The centre A is fixed at $(0, 0)$, and the centre B is moved from $(0, 0)$ to $(0, 6)$. The symbol x corresponds to the distance between the two particles (here a_0 is the Bohr radius). The vertical line denotes the beginning of the region of validity of the multipole expansion.

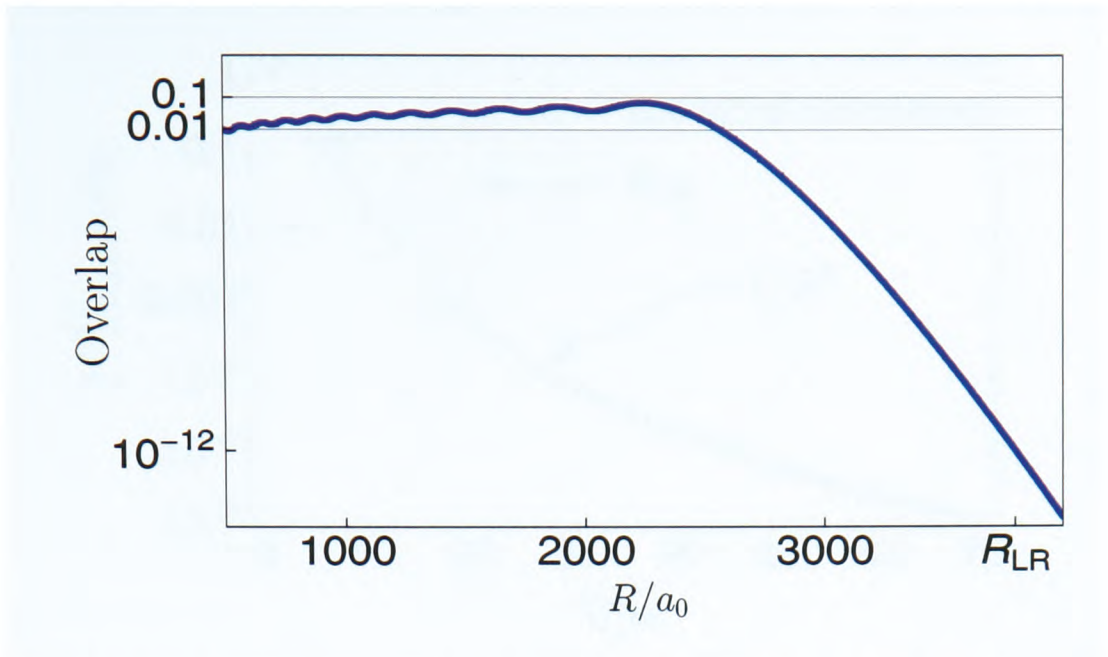


Figure 5.3. Overlap between the charge distributions of two hydrogen atoms with quantum numbers $(25, 1, 0)$ separated by a distance R/a_0.

As can be seen in Figure 5.2, the multipole expansion is accurate in its region of validity $r_{1A}+r_{2B} < R$ even with a small number of terms. However, it diverges from the exact potential very rapidly outside of this region. For instance, considering the potential shown in Fig. 5.2, an overlap ϵ with $(r_{1A} + r_{2B})/R = 1 + \epsilon$ of the order of 10^{-1}–10^{-2} between the position of the two particles causes a relative difference between the multipole expansion and the exact potential of the order of 60-70% !

In the quantum case, the utilisation of the multipole expansion requires that the overlap between the charge distributions of two electrons be zero. The minimum distance between two atoms such that the interactions between their electrons can be described by Eq. (5.9) is given by the so-called LeRoy radius $R_{\rm LR} = 2(\langle r^2\rangle^{1/2}_{\mathbf{q_A}} + \langle r^2\rangle^{1/2}_{\mathbf{q_B}})$ where $\langle r^2\rangle^{1/2}_{\mathbf{q}}$ is the root mean square of the position of an electron with quantum number $\mathbf{q}$, and $\mathbf{q_A}$ and $\mathbf{q_B}$ correspond to the quantum numbers of the electron located on atom A and B, respectively (see e.g. [143]). As a rule of thumb, the LeRoy radius is given by $R_{\rm LR} \sim 2\pi n^2 a_0$, where a_0 is the Bohr radius. For illustration, the overlap between the charge distributions of two highly-excited hydrogen atoms is shown in Fig. 5.3. Close to the LeRoy radius, the overlap drops significantly, whereas it is proportional to 10^{-1}–10^{-2} up to more than half the dis-

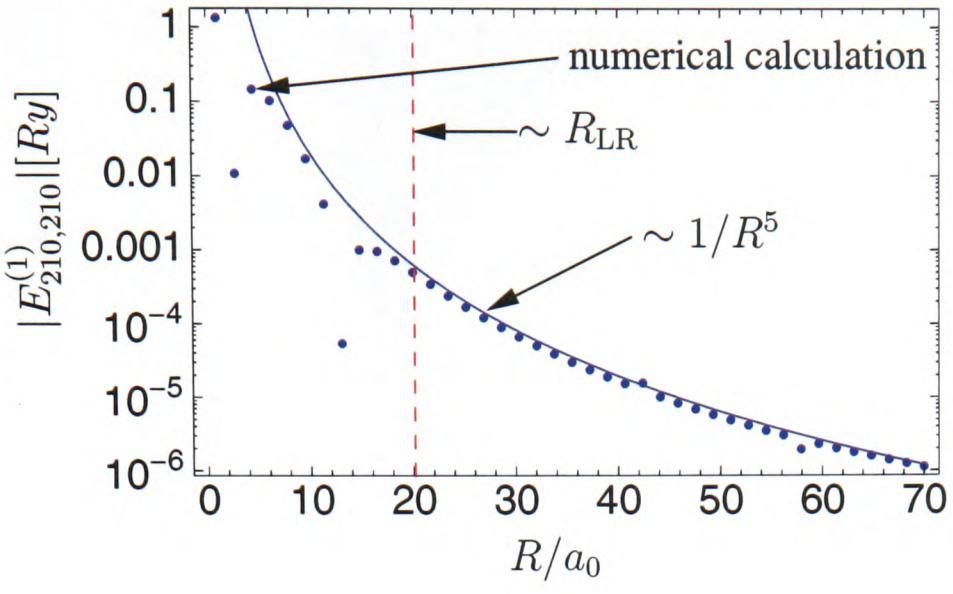


Figure 5.4. First-order correction to the energy of two interacting atoms in the state $(2,1,0)$ separated by a distance R. As expected, the power law decay $\sim 1/R^5$ becomes apparent beyond the LeRoy radius.

tance, even between highly-excited states with shallow charge-density distributions. Therefore, below the LeRoy radius, the description of inter-atomic interactions using the multipole expansion is very uncertain.

5.6 Long-range molecular potentials

When two atoms are separated by distances greater than the LeRoy radius, their electronic interactions are well described by Eq. (5.9), and the energy of the atomic pair is obtained by evaluating the different orders of correction to the unperturbed system. This procedure yields potentials of the form

$$V = \sum_n V_n(R), \tag{5.10}$$

where $V_n(R) = -C_n/R^n$ with C_n a dispersion coefficient depending on the quantum state of the two atoms (see e.g. Ref. [144]).

In the context of alkali dimers, several authors have calculated dispersion coefficients for different molecular symmetries (see e.g. Marinescu *et al.* [145] and

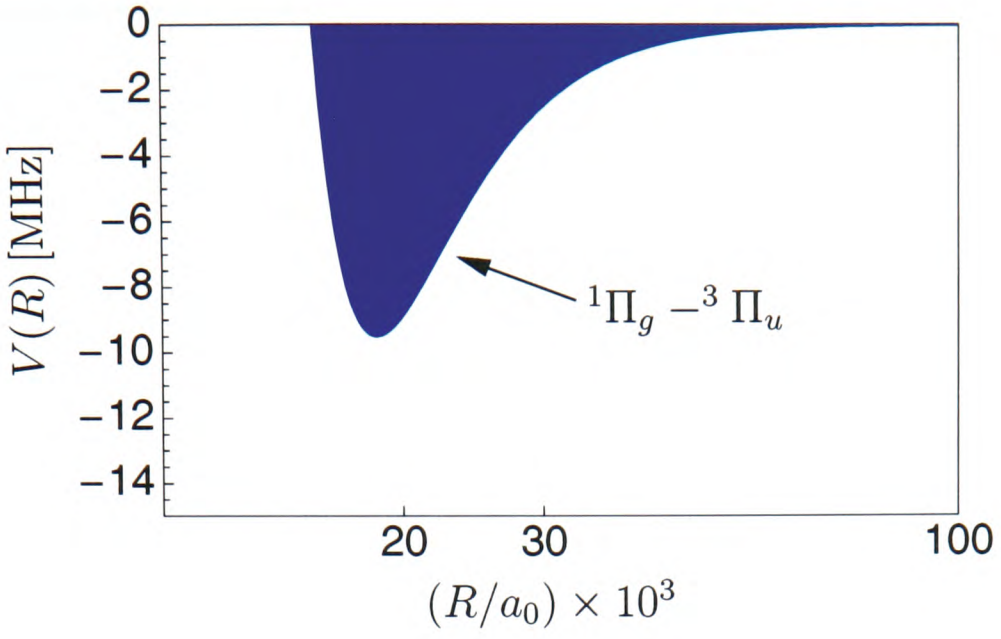


Figure 5.5. Molecular potential associated with the symmetry $^1\Pi_g - ^3\Pi_u$ ($n = 40$).

references therein). For instance, the first-order correction to the energy of two atoms in the unperturbed state $\psi^{(0)}_{n10,n10}$ is proportional to $\sim 1/R^5$ with a dispersion coefficient $C_5 = \langle r^2 \rangle^2_{n10}$ (see e.g. Ref. [145, 146]). For illustration, the first order correction to the energy of two atoms in the $(2, 1, 0)$ state is shown in Fig. 5.4.

Depending on the symmetry of the unperturbed wavefunction of the two atoms, the potential (5.10) can take the form of a molecular potential. For instance, the unperturbed wavefunction $\psi^{+}_{n11,n10}(\mathbf{r_1}, \mathbf{r_2})$ of two atoms with $m+m' = 1$ (denoted by $^1\Pi_g - ^3\Pi_u$) generates dispersion coefficients $C_5 \sim 3n^8$ and $C_6 \sim -0.7n^{11}$ that result in the formation of a minimum in the potential at a distance $R \sim 18 \times 10^3\, a_0$ (see Fig. 5.5). The potentials found in this way are shallow, and very long-range [27, 142]. Consequently, their detection using standard spectroscopic techniques is experimentally very challenging [25, 27, 135].

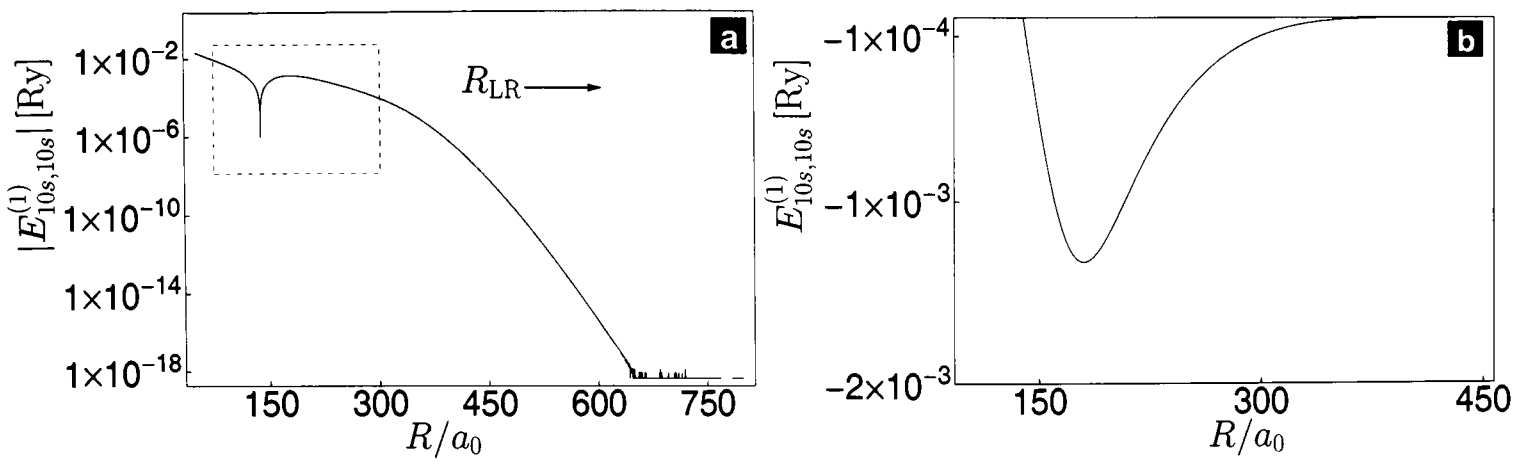


Figure 5.6. First-order correction to the energy of two atoms in the $(10, 0, 0)$ state. (a) As expected, the first-order correction vanishes beyond the LeRoy radius; (b) Below the LeRoy radius, it exhibits a molecular potential curve at distance $R \sim 180\, a_0$.

5.7 Below the LeRoy radius?

For certain states such as ${}^1\Sigma_g^+ - {}^3\Sigma_u^+$ with electrons in the $(n, 1, 0)$ state, the use of Eq. (5.10) indicates the existence of much deeper molecular potentials between highly-excited atoms at distances of less than half the LeRoy radius. Since there exists a small overlap between the charge distributions of the atoms in this range, the characterisation of these potentials using the multipole expansion is inappropriate, and so different methods that better take into account the short-range behaviour of the coulombic interaction must be sought.

Also, it is interesting to note that the first-order correction to the energy of interacting atoms, e.g. in the $(n, 0, 0)$ state, is zero when using the multipole expansion of the potential. However, below the LeRoy radius, such a term is non-zero, and takes the form of a molecular curve (see Fig. 5.6). Thus, some molecular potentials that are rather long-range, yet still below the LeRoy radius simply cannot be studied using Eq. 5.10.

In the context of optical lattices, there is great interest in studying the molecular potentials of dimers formed by highly-excited atoms whose equilibrium distance is located below the LeRoy radius. Indeed, the equilibrium distances of such poten-

tials are expected to correspond to typical lattice spacings achievable with current technology. Hence, the photo-association rate of molecular states from ground-state atoms could be enhanced by using optical lattices to fix the initial position of pairs of ultracold atoms to the equilibrium distance of the targeted molecular potential. Another great advantage of these potentials is that they are expected to be quite deep, which facilitates their observation.

The greatest obstacle to the investigation of such potentials is the evaluation of molecular integrals. For large values of the principal quantum number of the atoms ($n > 8$), their calculation becomes almost intractable using standard integration methods. This difficulty is principally due to the oscillatory nature and large spatial extent of the atomic radial wavefunction. This is particularly true for two-centre integrals, since they involve the integration over the coordinates of the two electrons over a large portion of space. For large principal quantum numbers, the convergence of these integrals is extremely slow, and their results sometimes uncertain [147, 148]. The approximation of these integrals to study molecular potentials below the LeRoy radius is the subject of the next chapter.

Chapter 6

Publication

Ultra-large Rydberg dimers in optical lattices.

Benoit Vaucher, S. J. Thwaite, Dieter Jaksch

Clarendon Laboratory, University of Oxford, Parks Road, Oxford OX1 3PU, United Kingdom

Phys. Rev. A. **78, 043415 (2008)**

We investigate the dynamics of Rydberg electrons excited from the ground state of ultracold atoms trapped in an optical lattice. We first consider a lattice comprising an array of double-well potentials, where each double well is occupied by two ultracold atoms. We demonstrate the existence of molecular states with equilibrium distances of the order of experimentally attainable inter-well spacings and binding energies of the order of 10^3 GHz. We also consider the situation whereby ground-state atoms trapped in an optical lattice are collectively excited to Rydberg levels, such that the charge-density distributions of neighbouring atoms overlap. We compute the hopping rate and interaction matrix elements between highly-excited electrons separated by distances comparable to typical lattice spacings. Such systems have tunable interaction parameters and a temperature $\sim 10^{-4}$ times smaller than the Fermi temperature, making them potentially attractive for the study and simulation of strongly correlated electronic systems.

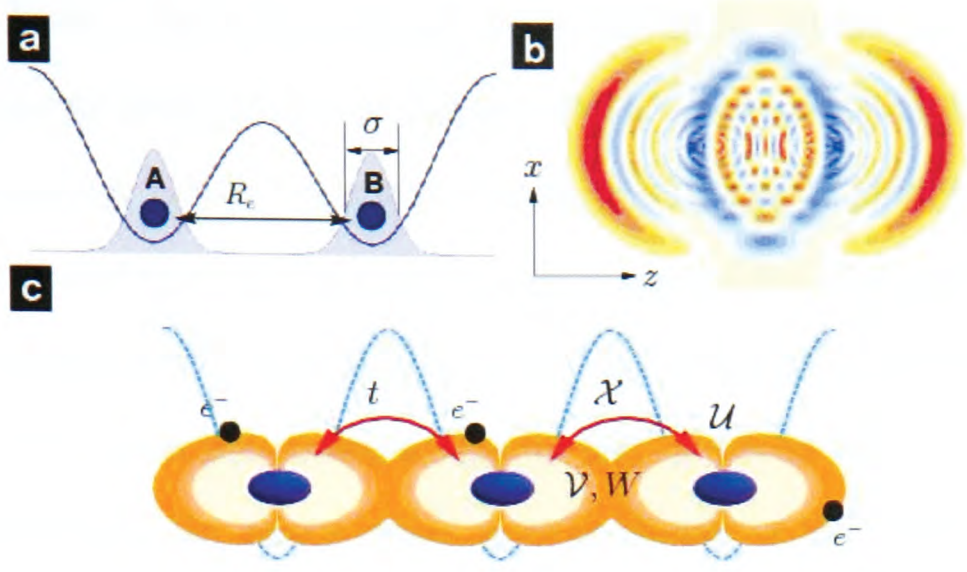


Figure 6.1. (a) An optical lattice with pairs of atoms well separated from each other is initialised. A laser pulse transfers each pair of atoms to a molecular state with a very large internuclear distance. (b) Density plot of a typical diatomic molecular wavefunction on the x-z plane ($y = 0$) in the relative coordinates of two electrons in highly excited np_z states. (c) The outer electron of each ground-state atom trapped in an optical lattice is transferred into a Rydberg state, such that the charge-density distributions between neighbouring atoms overlap. The electron hopping rate t becomes non-zero, and the interactions between electrons can be described by the parameters $\mathcal{U}$ (on-site interaction), $\mathcal{V}$, $\mathcal{W}$ and $\mathcal{X}$ (off-site interactions).

6.1 Introduction

Recent advances in the trapping and manipulation of ultracold atomic gases have provided experimentalists with the ability to coherently control large numbers of atoms. Two areas that have become the focus of experimental efforts of late are the use of ultracold atoms for the formation and manipulation of molecules [17, 131] and the creation and manipulation of Rydberg atoms in optical lattices [149]. In this paper we study whether combining these areas might lead to the production of diatomic molecules whose nuclear position is fixed by an optical lattice (see Figs. 6.1a–b). In particular, we examine the properties of ultralarge dimers with equilibrium distances of the order of typical lattice spacings and binding energies of the order of 10^3 GHz. We also investigate the prospect of using systems of interacting Rydberg atoms to simulate Fermi systems.

Molecules have a far richer energy structure than atoms, and can also have stronger long-range interactions, a feature which offers new possibilities for quantum control (see e.g. [150]). However, cooling molecules is notably difficult, since the absence of closed electronic transitions prevents the use of standard laser cooling procedures. An attractive approach to producing translationally cold molecules is thus to form them from pre-cooled atoms by way of photo-association or magnetic resonance techniques. In recent years several classes of ultracold molecules have been predicted and produced, including Feshbach molecules, Efimov trimers, and the famous 'trilobite' molecules, which are composed of a highly excited Rydberg atom interacting with another atom in its ground state [25, 151]. The existence of long-range molecules composed of two Rydberg atoms stabilised via dipole-dipole interactions has also been predicted [27, 136, 152]. These ultracold long-range Rydberg molecules have binding energies of the order of several hundred MHz (a factor of $\sim 10^6$ greater than the typical temperature of ultracold atoms, but weak by molecular standards), a lifetime expected to be similar to that of Rydberg atoms, and equilibrium distances of the order of $10^4\, a_0$ (with a_0 the Bohr radius) [27]. Recent advances in high-resolution microscopy techniques may offer new possibilities to study the spatial structure of such molecules [153]. Theoretical treatments of Rydberg molecules to date have primarily dealt with the regime in which the internuclear separation is greater than the Le Roy radius. In this regime the overlap between the atomic charge-density distributions is vanishingly small [27, 136]. In contrast to these works we consider the regime where the internuclear distance of the molecular dimer is comparable to typical lattice spacings, but smaller than the Le Roy radius, in which case the overlap of the charge distributions and effects such as the exchange interaction must be taken into account.

The simulation of condensed-matter systems is another area to which optical lattices are uniquely suited. Optical lattices have extremely flexible geometries, and

by a suitable choice of laser configuration, any desired lattice structure can be created [154, 155]. Fermions loaded into an optical lattice can be used as a model of electrons in a solid, with the significant advantage of having a periodic potential that is defect-less and fully customisable [73]. However, the ratio between the currently attainable temperature T of fermionic atoms trapped in an optical lattice and the Fermi temperature T_F of the system is $T/T_F \sim 0.25$, preventing the clean observation of such interesting phenomena as the BCS transition or the emergence of certain types of anti-ferromagnetic order [73, 156, 157]. In the final section of this paper we consider the possibility of collectively transferring a population of ground-state atoms trapped in an optical lattice to a highly excited Rydberg level, such that the charge-density distributions of neighbouring atoms overlap (see Fig. 6.1c). We extend the model developed in the first section to compute the hopping rate and interaction parameters between the highly excited electrons, and determine the dependence of these quantities on the initial lattice spacing. While the implementation of these systems is experimentally challenging and beyond the scope of this paper [158], we note that experimental temperatures far smaller than the Fermi temperature ($T/T_F \sim 10^{-4}$) might be readily attainable, making the realisation of such systems a promising new approach to the quantum simulation of interacting fermions.

The paper is organised as follows. In Sec. 6.2 we present the model that we subsequently use to investigate the existence of attractive molecular potentials with equilibrium distances below the Le Roy radius. We approximate the lifetime of these molecules and calculate their equilibrium internuclear distance for different values of the principal quantum number of the electrons. In Sec. 6.3 we use the model introduced in the first section to compute the hopping rate and interaction parameters of the Rydberg electrons and discuss the possibility of using these setups to simulate condensed-matter systems. We conclude in Sec. 6.4.

6.2 Molecular potentials of ultra-large Rydberg dimers

In this section we present a method of evaluating the energy of highly excited diatomic molecular states whose equilibrium distance R_e is below the Le Roy radius. We develop an efficient method of computing one- and two-centre molecular integrals over electronic orbitals with large principal quantum numbers n and calculate the depth and equilibrium position of molecular potentials accessible from the ground state via photo-association for values of n up to $n = 35$. We estimate the radiative lifetime of the highly excited molecular potentials.

Quantum chemistry methods commonly used within the Le Roy radius typically become computationally expensive when dealing with Rydberg molecules due to the size of the basis set required to describe the spatially diffuse Rydberg orbitals. In order to obtain qualitative results in this computationally challenging regime we take a simple wavefunction *ansatz* inspired by the Heitler-London treatment of the hydrogen molecule. Due to the simplistic form of the molecular wavefunctions used we do not expect the method presented to produce quantitatively accurate results; rather, our aim is to obtain qualitatively correct results and insights within a regime where common methods of calculating molecular potentials fail or become computationally costly.

6.2.1 Model

We consider an optical lattice potential forming an array of double-wells separated from each other by sufficiently high optical barriers that each double well can be considered as an isolated system [54]. We assume that each double well initially contains two ^{87}Rb atoms in their ground state, and that the potential is sufficiently

deep that the Wannier function associated with each atom is well localised in one half of the well. Because alkali atoms have only a single valence electron, their energy levels are described by the same quantum numbers as those of the hydrogen atom. If the ground-state atoms are excited to Rydberg levels with $n > 30$ by applying a laser pulse to the system, the charge distributions of atoms in the same double well will overlap, and under certain conditions a stable molecular state will be formed. We aim to study the basic properties of these molecules and explore whether they may be produced in an optical lattice with experimentally realistic parameters. Since the temperature of the system is very low, the velocity of the electrons – even in highly excited states – is much greater than that of the trapped ions, and the electrons respond almost instantaneously to displacements of the ions [27]. Consequently, we will calculate molecular potentials in the Born-Oppenheimer (BO) approximation [139, 140].

Neglecting interactions between atoms belonging to different double wells, the energy of a homonuclear molecule formed by the atoms in a double well is given within the BO approximation by the eigenvalues of the Hamiltonian

$$H(R) = -\frac{\hbar^2}{2m_e}\left(\nabla^2_{\mathbf{r}_1} + \nabla^2_{\mathbf{r}_2}\right) + j_0\left(\frac{1}{R} + \frac{1}{r_{12}} - \frac{1}{r_{1A}} - \frac{1}{r_{1B}} - \frac{1}{r_{2A}} - \frac{1}{r_{2B}}\right), \tag{6.1}$$

where $\mathbf{r}_i$ $(i = 1, 2)$ is the position of the i^{th} electron; $r_{i\xi}$ $(\xi = A, B)$ is the distance between the i^{th} electron and atomic centre ξ; r_{12} is the distance between the two electrons; $j_0 = e^2/(4\pi\varepsilon_0)$, where ε_0 is the permittivity of free space and e the elementary unit of charge; and R is the distance between the nuclei. In the BO approximation R is treated as a classical variable upon which the eigenvalues and eigenfunctions of the Hamiltonian depend parametrically. Following a similar approach to that of Ref. [137, 152], we approximate the energy of the molecule by diagonalising the

Hamiltonian (6.1) using as a basis the asymptotic electronic states

$$\Psi^{\pm}_{\mathbf{q},\mathbf{q}'} = \mathcal{N}^{\pm}_{\mathbf{q},\mathbf{q}'}[\mathrm{A}_{\mathbf{q}}(\mathbf{r}_1)\mathrm{B}_{\mathbf{q}'}(\mathbf{r}_2) \pm \mathrm{A}_{\mathbf{q}}(\mathbf{r}_2)\mathrm{B}_{\mathbf{q}'}(\mathbf{r}_1)], \tag{6.2}$$

where $\mathrm{A}_{\mathbf{p}}(\mathbf{r}_i)$ ($\mathrm{B}_{\mathbf{p}}(\mathbf{r}_i)$) is a hydrogen-like wavefunction with quantum numbers $\mathbf{q} = (n, \ell, m)$ centred on nucleus $A(B)$, and $\mathcal{N}^{\pm}_{\mathbf{q},\mathbf{q}'} = [2(1 \pm |S_{\mathbf{q},\mathbf{q}'}|^2)]^{-1/2}$ is a normalisation factor, where $S_{\mathbf{q},\mathbf{q}'} = \int d\mathbf{r}\, \mathrm{A}^*_{\mathbf{q}}(\mathbf{r})\mathrm{B}_{\mathbf{q}'}(\mathbf{r})$ is the overlap integral [139]. The basis elements that are symmetric or anti-symmetric in the coordinates have an associated anti-symmetric (singlet) or symmetric (triplet) function of spins respectively. Each basis state (6.2) describes the two electrons being exchanged between the two nuclei, and corresponds to an *ansatz* for a valence-bond wavefunction [140]. The diagonal elements of the Hamiltonian (6.1) using the states (6.2) as a basis correspond to the molecular potentials obtained using the Heitler-London method [139, 159].

The hydrogenic wavefunction of the valence electron centred on atom ξ located at $\mathbf{r}_\xi$ is well approximated by the (unnormalized) function

$$\xi_{\mathbf{q}}(\mathbf{r}) = P_\ell(\cos\theta_\xi)\frac{\mathrm{e}^{\mathrm{i}m\phi}}{a_0^{3/2}}\left(\frac{2\rho_\xi}{n^*}\right)^{n^*}\mathrm{e}^{-\rho_\xi/n^*}\sum_{k=0}^{k_{\max}}\mathrm{b}_k\,\rho_\xi^{-(k+1)}. \tag{6.3}$$

Here $\rho_\xi = r_\xi/a_0$ with $r_\xi = |\mathbf{r} - \mathbf{r}_\xi|$ the radial distance from atomic centre ξ, θ_ξ is the angle between the vector $\mathbf{r}_\xi$ and the internuclear axis, ϕ is the azimuthal angle, $P_\ell(x)$ is a Legendre polynomial, and $n^* = n - \delta_\ell$ is the effective principal quantum number, with δ_ℓ a quantum defect whose value depends on the angular momentum quantum number ℓ and the atomic species [160]. The coefficients $\mathrm{b}_k = \mathrm{b}_{k-1}(n^*/2k)[\ell(\ell+1) - (n^* - k)(n^* - k + 1)]$ are defined recursively with $\mathrm{b}_0 = 1$ and $k_{\max}$ is an integer satisfying $n^* - \ell - 1 \leq k_{\max} < n^* - \ell$ [161, 162]. The orbital defined in Eq. (6.3) is known as the asymptotic form of the quantum defect wavefunction; for $\delta_\ell = 0$, it is identical to the hydrogenic wavefunction, while for $\delta_\ell \neq 0$ it provides an accurate

description of a Rydberg electron in the mid- and long-range. It differs significantly from the exact quantum defect wavefunction only at short distances from the atomic cores, which is of little consequence since the interactions we consider here depend mainly on the outer part of the atomic wavefunctions.

For $n > 20$, the overlap between the charge-density distributions of atoms separated by distances smaller than the Le Roy radius (for $\mathbf{q} = \mathbf{q}'$) is typically of the order of $S_{\mathbf{q},\mathbf{q}'} \sim 10^{-1} - 10^{-2}$. The charge-density overlap is therefore not negligible in this regime, and the approximation of the Coulomb potential using the multipole expansion [145, 146] is not suitable. The multipole expansion diverges quite significantly from the Coulomb potential even in the presence of small charge-density overlap, and so the results obtained using this approximation below the Le Roy radius are very uncertain [27, 141].

We consequently estimate the energy of the dimer by evaluating the expectation value of the Hamiltonian (6.1) in the states (6.2), a task which requires the evaluation of a number of integrals over atomic orbitals. These integrals fall into two classes: the *one-centre* integrals, comprising the overlap integral $S_{\mathbf{q},\mathbf{q}'}$, the Coulomb integral $J_{\mathbf{q},\mathbf{q}'} = j_0 \int d\mathbf{r}\, \mathrm{B}^*_{\mathbf{q}}(\mathbf{r})(1/r_A)\mathrm{B}_{\mathbf{q}'}(\mathbf{r}) = j_0 \int d\mathbf{r}\, \mathrm{A}^*_{\mathbf{q}}(\mathbf{r})(1/r_B)\mathrm{A}_{\mathbf{q}'}(\mathbf{r})$, and the charge overlap integral $K^{\xi}_{\mathbf{q},\mathbf{q}'} = j_0 \int d\mathbf{r}\, \mathrm{A}^*_{\mathbf{q}}(\mathbf{r})(1/r_\xi)\mathrm{B}_{\mathbf{q}'}(\mathbf{r})$; and the *two-center* integrals

$$U^{\mathbf{q},\mathbf{q}'}_{\mathbf{p},\mathbf{p}'} = [\mathrm{A}_{\mathbf{q}}\mathrm{A}_{\mathbf{q}'}|\mathrm{A}_{\mathbf{p}}\mathrm{A}_{\mathbf{p}'}] \qquad W^{\mathbf{q},\mathbf{q}'}_{\mathbf{p},\mathbf{p}'} = [\mathrm{A}_{\mathbf{q}}\mathrm{B}_{\mathbf{q}'}|\mathrm{A}_{\mathbf{p}}\mathrm{B}_{\mathbf{p}'}] \tag{6.4}$$

$$V^{\mathbf{q},\mathbf{q}'}_{\mathbf{p},\mathbf{p}'} = [\mathrm{A}_{\mathbf{q}}\mathrm{A}_{\mathbf{q}'}|\mathrm{B}_{\mathbf{p}}\mathrm{B}_{\mathbf{p}'}] \qquad X^{\mathbf{q},\mathbf{q}'}_{\mathbf{p},\mathbf{p}'} = [\mathrm{A}_{\mathbf{q}}\mathrm{A}_{\mathbf{q}'}|\mathrm{A}_{\mathbf{p}}\mathrm{B}_{\mathbf{p}'}] \tag{6.5}$$

where

$$[\alpha\beta|\gamma\nu] = j_0 \iint \mathrm{d}\mathbf{r}_1\, \mathrm{d}\mathbf{r}_2\, \alpha^*(\mathbf{r}_1)\beta(\mathbf{r}_1)\frac{1}{r_{12}}\gamma^*(\mathbf{r}_2)\nu(\mathbf{r}_2). \tag{6.6}$$

The evaluation of one- and two-centre molecular integrals poses a considerable

Rule	Functional		Replacement
R1	$\int_1^\infty \mathrm{d}x\, \mathrm{e}^{-\alpha x} x^k$	$\rightarrow$	$(1/\alpha^{1+k})\Gamma_{1+k}(\alpha)$
R2	$\int_{-1}^1 \mathrm{d}x\, \mathrm{e}^{\beta x} x^k$	$\rightarrow$	$[(-\beta)^{-k}/\beta][\Gamma_{1+k}(-\beta) - \Gamma_{1+k}(\beta)]$

Table 6.1. Replacement rules used to generate analytical formula for one-centre integrals; $\Gamma_k(x)$ is the incomplete gamma function with $k \in \mathbb{N}_+$.

challenge for large values of the principal quantum numbers. The results of such integrals using direct numerical integration converge extremely slowly, and the answers so produced can suffer from dramatic losses of accuracy (a phenomenon known as numerical erosion; see e.g. [147, 148]). Following an approach suggested by M. P. Barnett, we use a computer algebra-based method to generate analytical formulae for the molecular integrals [147, 163, 164]. We have found this approach advantageous for three reasons: (i) it permits the fast evaluation of molecular integrals with high principal quantum number to arbitrary accuracy; (ii) once the analytical form has been found, the evaluation of an integral for different values of the internuclear distance is instantaneous; (iii) the analytical expressions of the integrals can be stored and re-used at little computational cost.

However, even with the use of symbolic calculations, the evaluation of molecular integrals for large values of n is computationally demanding. In order to make these calculations tractable for large n we restrict the value of the projection of the electronic angular momentum along the internuclear axis to $m = 0$. This limits the range of molecular states that can be investigated to those of symmetry $^1\Sigma_g^+$ and $^3\Sigma_u^+$; these are associated with the $\Psi^+_{\mathbf{q},\mathbf{q}'}$ and $\Psi^-_{\mathbf{q},\mathbf{q}'}$ basis states respectively. In this way we have been able to compute molecular integrals involving wavefunctions with principal quantum numbers up to $n = 35$.

In order to compute the molecular integrals it is convenient to express the electron coordinates in elliptical coordinates (λ, μ, ϕ) through the relations $r_\xi = (R/2)(\lambda \pm \mu)$ and $\cos\theta_\xi = [(1 \pm \lambda\mu)/(\lambda \pm \mu)]$, where plus and minus signs apply to $\xi =$

A and $\xi = B$ respectively. The volume element is given by $\mathrm{d}\mathbf{r} = (R/2)r_A r_B \mathrm{d}\lambda\,\mathrm{d}\mu\,\mathrm{d}\phi$, where $0 \leq \phi \leq 2\pi$, $-1 \leq \mu \leq 1$ and $1 \leq \lambda \leq \infty$. After rounding up the powers of r_ξ in Eq. (6.3) to the next integer value (which only significantly affects the shape of the wavefunction near the core) we find that the integrands of all of the one-centre integrals can be written in the form

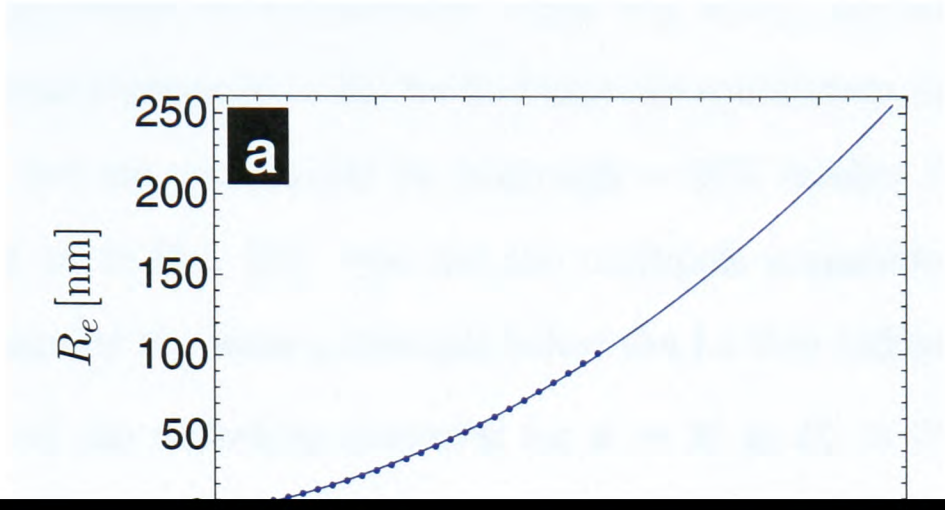
$\mathrm{e}^{-\alpha\lambda}\mathrm{e}^{\beta\mu}\sum_{ij} q_{i,j}\lambda^i\mu^j$, where $q_{i,j}$ are coefficients associated with a given integral. By applying the replacement rules defined in Table 6.1 every one-centre integral can be converted into an analytical expression with parametric dependence on R.

The evaluation of symbolic expressions for two-centre integrals proceeds similarly, although many more replacement rules are required. The general approach for two-centre integrals consists of expressing the Coulomb potential in the form of a sum of polynomials (such as the Legendre or Neumann expansion) before applying replacement rules on the terms resulting from the successive integrations over the coordinates of the first and second valence electron. Using this method, exact formulae are obtained for Eqs. (6.4), but only approximate expressions may be found for Eqs. (6.5) (see Appendix 6.A).

6.2.2 Results

Since we envisage producing the Rydberg dimers by applying a laser pulse to a system of ground-state atoms, we are primarily interested in the molecular states that are most strongly coupled to ground-state atoms by the dipole transition operator; namely, those of $^3\Sigma_u^+$ symmetry with a high p-character ($\ell = 1$). We will therefore restrict our analysis to these states. However, for values of $n \geq 10$ molecular states of $^3\Sigma_u^+$ and $^1\Sigma_g^+$ symmetry become quasi-degenerate [27, 145], and so the results presented here apply to molecular states of either of these symmetries.

We have estimated the equilibrium distances R_e and potential depths D_e =


a
250
200
150
100
50
R_e [nm]

$E_{\mathrm{mol}}(\infty) - E_{\mathrm{mol}}(R_e)$ of $np + np$ molecular potentials of $^3\Sigma_u^+$ symmetry using the Heitler-London approach for values of the principal quantum number up to $n = 35$ (see Fig. 6.2). We find that the equilibrium distance of these potentials follows the relation $R_e \simeq (1.628n^2 - 100.25)\, a_0$, which is about a factor of four smaller than the Le Roy radius for all values of n (see Fig. 6.2a). For larger values of the principal quantum number ($n > 35$) we find that the equilibrium distances predicted by our scaling law are comparable to (although $\sim 20\%$ smaller than) those found by Boisseau *et al.* in Ref. [27], who use the multipole expansion of the Coulomb potential to examine the same potentials below the Le Roy radius.

The depth of the molecular potential for $n = 35$ is $D_e \simeq 2000\,\mathrm{GHz}$, approximately three orders of magnitude larger than the potential depth of ultra-large molecules with symmetry $^1\Pi_g - ^3\Pi_u$ bonded via dipole-dipole interactions studied by Boisseau (see Fig. 6.2b). We find that the molecular binding energy decreases exponentially with the value of the principal quantum number according to the relation $D_e = \exp(\alpha_1 + \alpha_2 n^{\beta_2} + \alpha_3 n^{\beta_3})\,\mathrm{GHz}$ where $\alpha_1 = -6.53$, $\alpha_2 = -24.44$, $\alpha_3 = -20.51$, $\beta_2 = 0.14$ and $\beta_3 = -223.45$. Our predicted potential depths differ by up to an order of magnitude from those calculated using the multipole expansion; as Boisseau *et al.* point out in Ref. [27], this is probably a consequence of the inaccuracy of the multipole expansion below the Le Roy radius. Although the potentials produced using our method do not have the asymptotic R^{-5} behaviour expected from perturbation theory [145], this may be corrected by carrying out a numerical integration of the terms which were neglected during the symbolical calculations of the molecular integrals. This correction is feasible for small values of n, but very time consuming for larger values. However, a comparison with the results of exact numerical calculations of the same potentials up to $n = 8$ shows that our method reproduces the correct values of R_e and D_e within $\sim 3\%$.

Following the approach taken in Ref. [152], we diagonalised the Hamiltonian

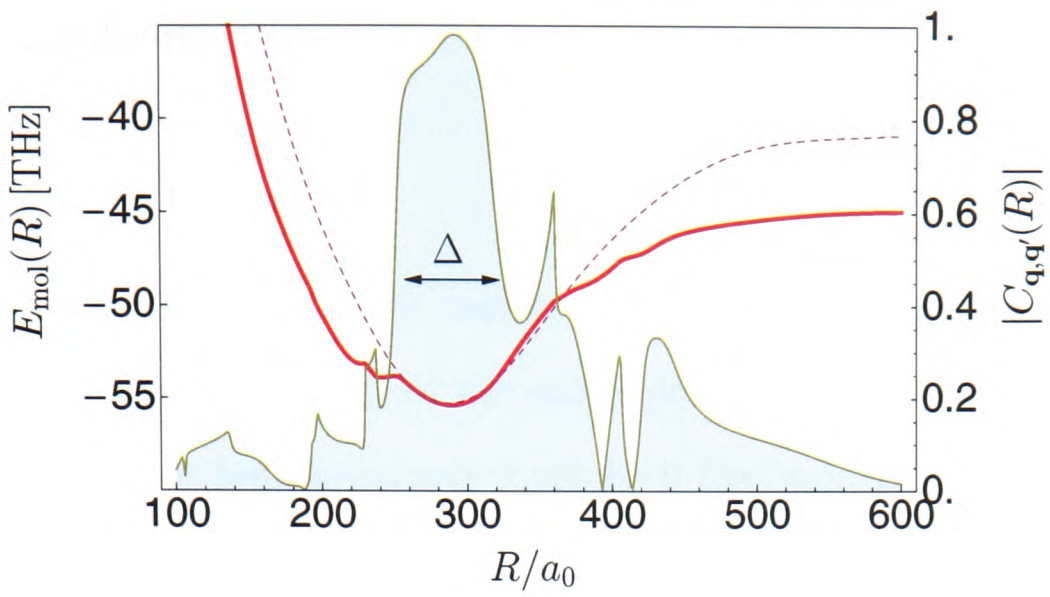


Figure 6.3. (left axis) The $^3\Sigma_u$ molecular potential (solid red line) associated with the wavefunction $\Psi_{\mathrm{mol}}(R)$ resulting from the diagonalisation of the Hamiltonian (see text) for $n = 16$. The dashed line shows the molecular potential for the $np+(n-1)p$ bare state. (right axis) The contribution $C_{\mathbf{q},\mathbf{q}'}(R)$ of the $\mathbf{q} = (16, 1, 0)$, $\mathbf{q}' = (15, 1, 0)$ basis state to the molecular wavefunction $\Psi_{\mathrm{mol}}(R)$; Δ denotes the width of the region over which this contribution is dominant.

using as a basis the molecular states (6.2) with a significant coupling to the $np+n'p$ asymptote. For $n' = n - 1$ and $n = 16$ we used the states $(n-1)s + (n+1)s$, $(n-1)s + ns$, $(n-1)s + (n+2-k)d$, $(n-2)d + (n-k)d$, $(n-3)d + (n-k+1)d$ and $(n-1-k')p + (n+k)p$, with $k, k' = 1, 2$. The diagonalisation procedure yields eigenstates of the form $\Psi_{\mathrm{mol}}(R) = \sum C_{\mathbf{q},\mathbf{q}'}(R)\Psi_{\mathbf{q},\mathbf{q}'}$, allowing the determination of the contribution of a given molecular state $\Psi_{\mathbf{q},\mathbf{q}'}$ to each eigenstate. Figure 6.3 shows the contribution of the asymptotic $np + (n-1)p$ state to an eigenstate Ψ_{mol}, and the potential curve $E_{\mathrm{mol}}(R)$ corresponding to this eigenstate, for the case of $n = 16$. In a region of width Δ about R_e the molecular potential is indistinguishable from that of the bare $np + n'p$ state, and the associated wavefunction has a very dominant $np + n'p$ character ($C_{\mathbf{q},\mathbf{q}'} = 0.98$ with $\mathbf{q} = (16, 1, 0)$ and $\mathbf{q}' = (15, 1, 0)$; see Fig. 6.3). This is due to the fact that the coupling between different states is generally weak (off-diagonal elements of the Hamiltonian are typically $\sim 10^{-1} - 10^{-3}$ smaller than diagonal ones) and the strongest coupling is seen between states with

identical angular momentum.

We find that the size of the region $\Delta \simeq 0.24n^2\,a_0$ is approximately a factor of three smaller than the width of the molecular potential associated with the bare $np+(n-1)p$ states (approximately given by $0.73n^2\,a_0$). This provides an indication of the nature of the wavefunction of the molecular states accessible by the photo-association of ground-state atoms initially trapped in an optical lattice. The distance $a_{\rm dw}$ between the two sides of a double well may be controlled by altering the laser parameters. The uncertainty in the initial position of the ground-state atoms is given by the width of their Wannier functions (see Fig. 6.1), which is proportional to $\sigma = a_{\rm dw}/[\pi(\tilde{V}/E_R)^{1/4}]$, where $\tilde{V}$ is the depth of the double-well and E_R the recoil energy [3]. By setting $a_{\rm dw} = R_e$ and considering the scaling of the width of the $np + (n-1)p$ molecular potentials, we find that $2\sigma \lesssim \Delta$ for lattice potential depths of the order of $\tilde{V} = 30$–$40\,E_R$. This suggests that using an optical lattice to enforce the initial position of the atoms before applying the photo-association pulse might offer advantages in providing access to molecular states with a very dominant $np + n'p$ character.

We have obtained an order-of-magnitude estimate of the lifetime of the photo-associated molecules by assuming for simplicity that the dominant decay mode is radiative dissociation into a pair of ^{87}Rb atoms. We neglect the rotational fine structure of the energy levels and any bound-bound decay channels and consider a transition between a bound state of vibrational quantum number ν' and energy $E_{\nu'}$ and a free continuum state of wavenumber k'' and energy $E_{k''} = \hbar^2 k''^2/(2\mu)$, where $\mu = m_{\rm Rb}/2$ is the reduced mass of the molecule. The Einstein A coefficient is given

by

$$A_{\nu' k''} = \frac{32\pi^3}{3\varepsilon_0 h^5 c^3}\sqrt{\frac{2\mu}{E_{k''}}}(E_{\nu'} - E_{k''})^3 \times \left| \int \left[\psi_{\nu'}^{\mathrm{vib}}(R)\right]^* D(R)\psi_{k''}^{\mathrm{vib}}(R)\, dR \right|^2 \quad \mathrm{J}^{-1}\,\mathrm{s}^{-1} \tag{6.7}$$

while the radiative lifetime of a single bound vibrational level is given by $\tau_{\nu'} = A_{\nu'}^{-1}$, where

$$A_{\nu'} = \int_0^\infty A_{\nu' k''}\, dE_{k''}. \tag{6.8}$$

Here $h = 2\pi\hbar$ is the Planck constant, c is the speed of light, $\psi_{\nu'}^{\mathrm{vib}}$ and $\psi_{k''}^{\mathrm{vib}}$ are vibrational wave functions for the discrete and continuum states respectively, and the dipole moment $D(R)$ is given by

$$D(R) = -e \iint \mathrm{d}\mathbf{r}_1 \mathrm{d}\mathbf{r}_2 \left[\Psi^{\pm}_{\mathbf{q}_i,\mathbf{q}_i}\right]^* (z_1 + z_2) \Psi^{\pm}_{\mathbf{q}_f,\mathbf{q}_f} \tag{6.9}$$

where z_1 and z_2 are the z-coordinates of the electrons and $\mathbf{q}_i$ and $\mathbf{q}_f$ denote the quantum numbers of the initial and final states. For large internuclear distances the continuum wave function $\psi_{k''}^{\mathrm{vib}}$ has the asymptotic form

$$\psi_{k''}^{\mathrm{vib}} \sim \sin(k''R + \eta) \tag{6.10}$$

where η is the scattering phase shift, which at low energies is given by $\eta = -k''a_s$ with a_s the s-wave scattering length. In the initial molecular state we approximate the true bound vibrational wavefunctions $\psi_{\nu'}^{\mathrm{vib}}(R)$ by the eigenstates of a harmonic approximation to the molecular potential centred about $R = R_e$. Due to the asymmetric nature of the molecular potential curves, this approximation becomes progressively worse as ν' increases. However, we expect that the ability to impose an

inter-atomic spacing close to the equilibrium distance of the targeted molecular state before applying the photo-association pulse will provide a measure of control over the range of vibrational levels occupied by the molecules, thus making the lowest vibrational levels the most relevant.

Although there are a huge number of final states to which the molecule could decay, the dependence of the decay rate given by Eq. (6.7) on $(E_{\nu'} - E_{k''})^3$ favours transitions that involve the emission of a high-energy photon. We therefore consider only transitions that finish within the continuum above the $5s$–$5s$ potential curve, neglecting all other decay channels. The radiative lifetimes thus calculated for the ground vibrational state $\nu' = 0$ are shown in Fig. 6.4; the lifetimes of higher vibrational levels (up to $\nu' = 10$) are the same to within $\sim 5\%$. Also plotted for comparison purposes is the radiative lifetime $\tau = \tau_0 n^3$ of a free Rydberg atom, where $\tau_0 = 1.4$ ns for ^{87}Rb [165]. Our calculations indicate that for $n \gtrsim 17$ the Rydberg dimers are more stable than the free atoms. For the highest molecular state considered ($n = 35$) we find lifetimes of the order of a few milliseconds, indicating that even if contributions from neglected decay channels were to reduce this lifetime by several orders of magnitude, the system could still be successfully interrogated and characterised by short (nanosecond to picosecond) laser pulses. To avoid possible stimulated emission contributions to the radiative decay process, the laser fields forming the optical lattice could be switched off as the Rydberg excitation pulse is applied. The subsequent free expansion of the atoms would not limit the window of time within which the system may be characterised, since the atoms are expected to remain localised within a few lattice spacings for a time of the order of 10 μs [60].

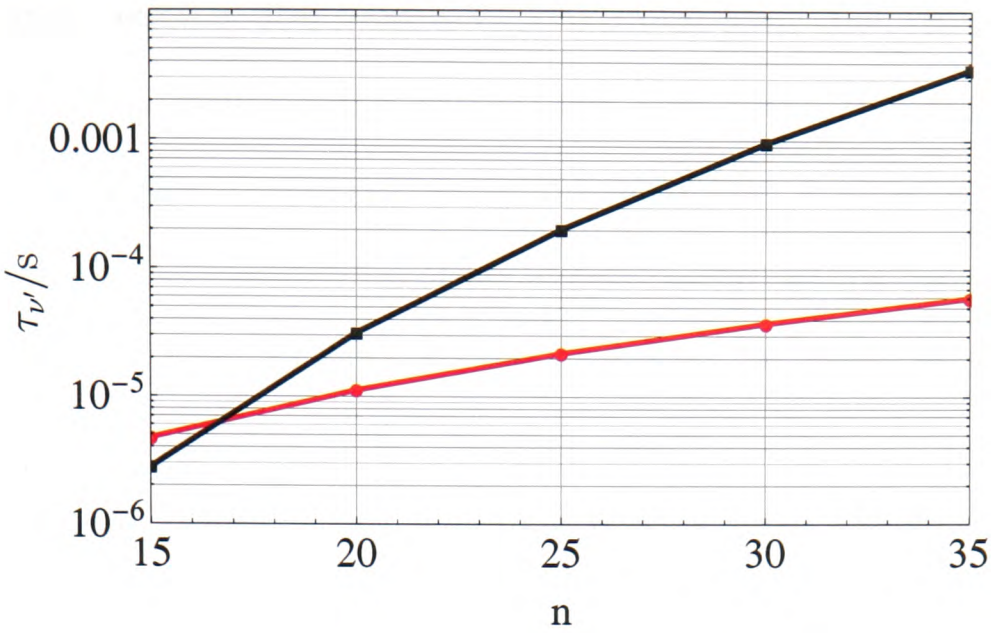


Figure 6.4. Radiative lifetimes for the $\nu' = 0$ vibrational level in molecular excited states with principal quantum numbers $n = 15$–35 (black line). The radiative lifetime $\tau = \tau_0 n^3$ of a free Rydberg atom is plotted for comparison purposes (red line).

6.3 Interactions between highly excited electrons in a lattice

In this section we consider the situation where ground state atoms trapped in a regular optical lattice are collectively excited to a given Rydberg state such that the charge-density distributions of neighbouring atoms overlap. With overlapping charge-density distributions between neighbouring atoms, the valence electrons will tunnel between lattice sites and interact with each other, mimicking the behaviour of electrons in metals. Such a system may have interesting applications for the quantum simulation of electrons in lattice systems. Assuming that the band structure of such a system is well described by a tight-binding model, we will find that using the hopping rate calculated in the next section that the Fermi temperature of a half-filled lattice is $T_F \sim 10^{-3}\,\mathrm{K}$, some 5 orders of magnitude larger than typical temperatures achieved in experiments with ultracold atoms. While the efficient population transfer of atoms to Rydberg states is experimentally very challenging and goes beyond the

scope of this paper (see e.g. Ref. [158]), this figure implies that after the excitation step, the system temperature could still remain well within the Fermi degeneracy regime ($T \ll T_F$). This would enable the observation of interesting many-body phenomena currently inaccessible to other experimental setups involving fermionic atoms where the ratio $T/T_F \approx 0.25$ (see e.g. Ref. [73, 166]). In this section, we use the tools developed previously to evaluate the typical interaction parameters and the hopping rate of such a system, and investigate their dependence on the inter-atomic spacing fixed by the lattice.

6.3.1 Model

In this section we assume that ground-state atoms trapped in an optical lattice can be collectively excited to a given Rydberg state. We assume that the dynamics of the valence electrons in the lattice is restricted to only one spatial mode per site i that corresponds to an orbital $\phi_i(\mathbf{r}) = \langle \mathbf{r} \,|\, \phi_i \rangle$ associated with a given Rydberg state localised at site i with two spin orientation. The Hamiltonian of the system is then given by

$$\hat{H} = -\sum_{i,j,\sigma} t_{ij}\, \hat{c}^{\dagger}_{i\sigma}\hat{c}_{j\sigma} + \frac{1}{2}\sum_{\substack{i,j,k,l \\ \sigma,\sigma'}} V(i,j,k,l)\hat{c}^{\dagger}_{i,\sigma}\hat{c}^{\dagger}_{j,\sigma'}\hat{c}_{k,\sigma'}\hat{c}_{l,\sigma}, \tag{6.11}$$

where $\hat{c}^{\dagger}_{i\sigma}$ is a creation operator associated with the orbital $\phi_i(\mathbf{r})$ and spin σ, t_{ij} describes the hopping of a particles between sites i and j; and the inter-site interactions are given by

$$V(i,j,k,l) = \iint \mathrm{d}r\, \mathrm{d}r' \phi^*_i(r)\phi^*_j(r')V_{\mathrm{ee}}(r-r')\phi_k(r)\phi_l(r'), \tag{6.12}$$

where $V_{\mathrm{ee}}(r-r')$ is the interelectronic potential. We assume here that next-nearest-neighbour hopping can be neglected, and consider only nearest-neighbour interac-

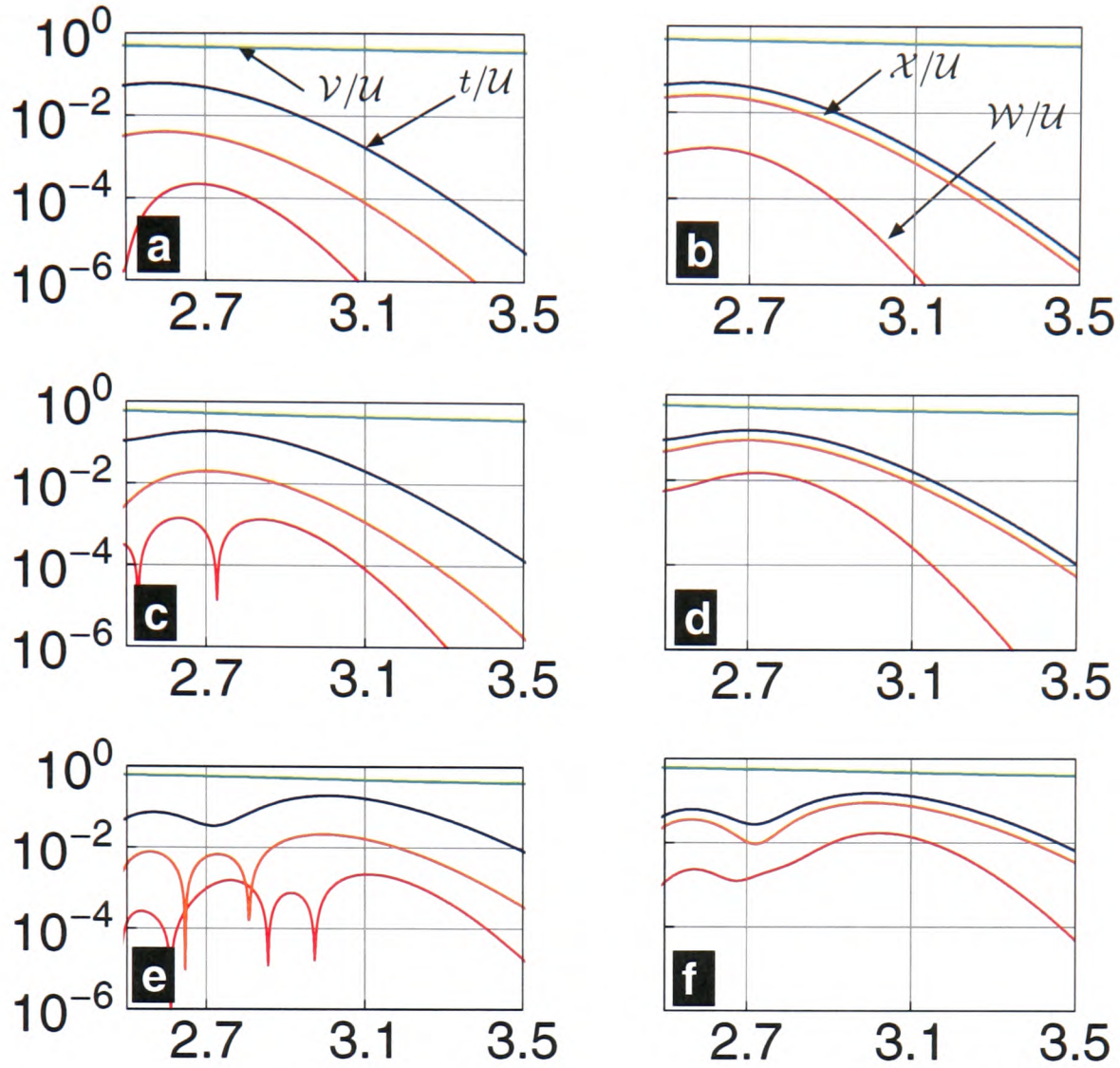


Figure 6.5. Relative values of the interaction parameters of a Hubbard model of Rydberg electrons in a state with quantum numbers $\mathbf{q} = (30, \ell, 0)$. (a) $\ell = 0$ (b) $\ell = 0$, setting $S_{\mathbf{q},\mathbf{q}} = 0$; (c) $\ell = 1$ (d) $\ell = 1$, setting $S_{\mathbf{q},\mathbf{q}} = 0$; (e) $\ell = 2$ (f) $\ell = 2$, setting $S_{\mathbf{q},\mathbf{q}} = 0$. From top to bottom we have $\mathcal{V}/\mathcal{U}$ (green), $t/\mathcal{U}$ (blue), $\mathcal{X}/\mathcal{U}$ (orange), and $\mathcal{W}/\mathcal{U}$ (red).

tions. In this situation the hopping term $t = t_{i,i+1}$ consists of the kinetic energy and Coulomb potential of neighbouring ion cores

$$t = \langle \phi_i \, | \left(-\frac{\hbar^2}{2M}\nabla^2 - \frac{j_0}{|\mathbf{r} - \mathbf{R}_i|} - \frac{j_0}{|\mathbf{r} - \mathbf{R}_{i+1}|} \right) | \, \phi_{i+1} \rangle \, , \tag{6.13}$$

and the only two-electron interaction terms taken into account are $\mathcal{U} = V(i, i, i, i)$, $\mathcal{X} = V(i+1, i, i, i)$, $\mathcal{V} = V(i, i+1, i+1, i)$ and $\mathcal{W} = V(i, i+1, i, i+1)$ [167].

Electronic orbitals centred at different lattice sites are often considered to be

orthogonal and equated to the Wannier functions of the crystal [57]. However, a better definition of the Wannier function centred at site i in terms of electronic orbitals is given by

$$\phi_i = \psi_i - \frac{S_i\psi_{i+1} + S_{i-1}\psi_{i-1}}{2}, \tag{6.14}$$

where ψ_i is a normalised electronic wavefunction with quantum numbers centred at site i, and S_i is the overlap between the orbitals of site i and $i+1$ [168]. In the regime where the terms proportional to S_i^2 can be neglected, the functions ϕ_i form an orthonormal basis set. By inserting the definition (6.14) into Eqs. (6.12) and (6.13) and assuming that the site orbitals $\psi_i = \Psi_{\mathbf{q}}(\mathbf{r} - \mathbf{R}_i)$ correspond to hydrogenic wavefunctions with quantum numbers $\mathbf{q}$, the parameters of the Hamiltonian (6.11) can be expressed in terms of two-centre molecular integrals as

$$\begin{aligned}
\mathcal{U} &= U^{\mathbf{q},\mathbf{q}}_{\mathbf{q},\mathbf{q}} - 4S_{\mathbf{q},\mathbf{q}}X^{\mathbf{q},\mathbf{q}}_{\mathbf{q},\mathbf{q}}\,, \\
t &= (E_{\mathbf{q}} + j_0/R)S_{\mathbf{q},\mathbf{q}} - 2K_{\mathbf{q},\mathbf{q}} \\
\mathcal{V} &= V^{\mathbf{q},\mathbf{q}}_{\mathbf{q},\mathbf{q}} - 2S_{\mathbf{q},\mathbf{q}}X^{\mathbf{q},\mathbf{q}}_{\mathbf{q},\mathbf{q}}\,,\ \mathcal{W} = W^{\mathbf{q},\mathbf{q}}_{\mathbf{q},\mathbf{q}} - 2S_{\mathbf{q},\mathbf{q}}X^{\mathbf{q},\mathbf{q}}_{\mathbf{q},\mathbf{q}}, \\
\mathcal{X} &= X^{\mathbf{q},\mathbf{q}}_{\mathbf{q},\mathbf{q}} - S_{\mathbf{q},\mathbf{q}}[W^{\mathbf{q},\mathbf{q}}_{\mathbf{q},\mathbf{q}} + \frac{1}{2}(U^{\mathbf{q},\mathbf{q}}_{\mathbf{q},\mathbf{q}} + V^{\mathbf{q},\mathbf{q}}_{\mathbf{q},\mathbf{q}})],
\end{aligned} \tag{6.15}$$

where $K_{\mathbf{q},\mathbf{q}} = K^A_{\mathbf{q},\mathbf{q}} = K^B_{\mathbf{q},\mathbf{q}}$, $\mathcal{U}$ is the on-site interaction, $\mathcal{V}$ and $\mathcal{W}$ are off-diagonal repulsion terms, and $\mathcal{X}$ is sometimes called the density-dependent hopping or enhanced hopping rate [169]. The absolute value of the ratios between different interaction parameters for atoms in np_z, ns and nd_{z^2} states ($n = 30$) are shown in Fig. 6.5, where we have plotted the parameters in Eq. (6.15) obtained with $S_i = 0$, that is, with Wannier functions represented by bare atomic orbitals. The orthogonalisation procedure (i.e. replacing ψ_i by ϕ_i) mainly affects the smallest parameters $\mathcal{X}$ and $\mathcal{W}$ in the regions where the value of S_i^2 is not small enough for the Wannier functions to be effectively orthogonal.

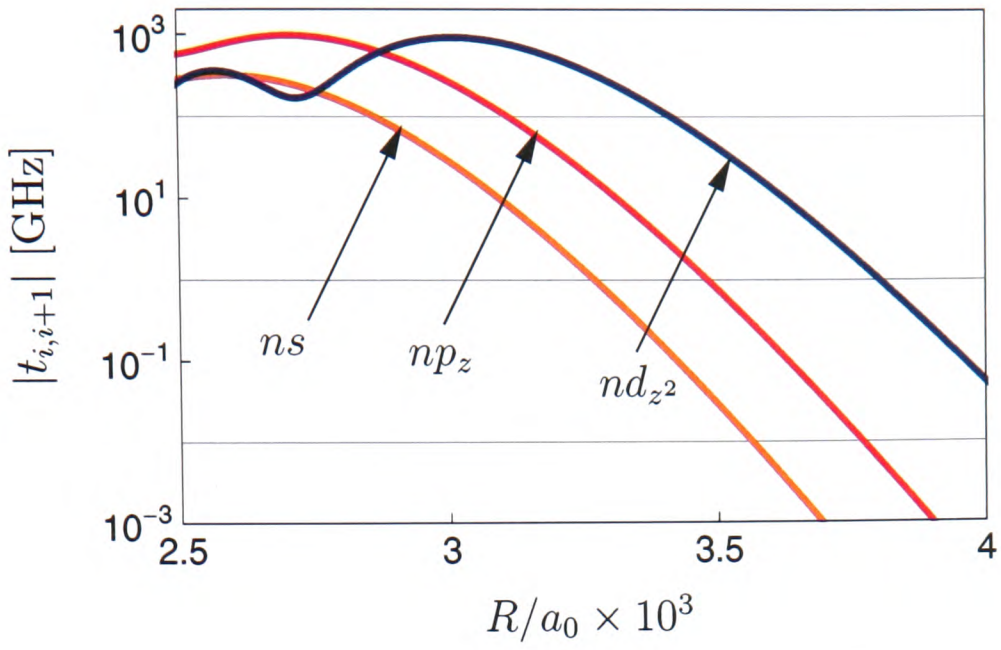


Figure 6.6. Hopping rate in the z-direction between sites separated by a distance R for electrons in ns, np_z, nd_{z^2} states ($n = 30$).

The interaction parameters calculated above correspond to the intermediate screening case, that is $\mathcal{U} > \mathcal{V} \gg \mathcal{W}$ and $\mathcal{X} \simeq \kappa\mathcal{J}$, where κ is a constant [170, 171]. The ratios between the parameters are similar to those found in realistic systems, e.g. between p-electrons in conjugated polymers [170]. For different values of the angular momentum, these ratios differ mainly in the way they behave at large distances. The hopping rates t are shown in Fig. 6.6, and, for the quantum numbers considered, vary between 10^2 and 10^{-4} GHz for intersite distances between 150 and 250 nm respectively.

6.4 Conclusion

We showed that optical lattices forming arrays of double-well potentials may be exploited to selectively photo-associate pairs of atoms to molecular states with binding energies of the order of 10^3 GHz, far larger than those of long-range molecules stabilised by dipole-dipole forces. These molecular states are expected to have equilibrium distances of the order of the typical lattice spacings and lifetimes several

orders of magnitude larger than the timescales required to interrogate and characterise them by way of short laser pulses.

We considered the possibility of collectively exciting ground-state atoms trapped in a regular lattice to a given Rydberg level such that the charge-density distributions of atoms located in neighbouring sites overlap. Assuming that such a system could be realised, we calculated the typical interaction parameters between the Rydberg electrons and the hopping rate between sites. With a temperature well below the Fermi temperature and tunable interaction parameters, such systems might offer an interesting alternative approach to the simulation of Fermi systems. For instance, the ability to change the lattice spacing such that $v = \mathcal{U}/\mathcal{V} > \frac{1}{2}$ or $v < \frac{1}{2}$ would offer the possibility of engineering a charge-density wave (CDW) or a spin-density wave (SDW), respectively. The preparation of a SDW state could even be facilitated by using spin-changing collisions between ultracold ^{87}Rb ground-state atoms to produce a Néel-like state $|\uparrow\downarrow\uparrow\downarrow\ldots\rangle$ that has a spin arrangement identical to that of the SDW ground state along one spatial direction [52]. If realised, such a system would allow the observation of a phase transition between the SDW and CDW phases, by, for example, the measurement of the zero-frequency SDW susceptibility [1] or the CDW structure factor, both of which diverge linearly in their respective phase [172]. Further, the versatility of optical lattice setups may allow the excitation of Rydberg atoms with a given angular momentum, which potentially enables exotic quantum phase transitions to be engineered: indeed, the value of the electronic angular momentum not only influences the relative values of the system interaction parameters, but also in some cases their signs (see e.g. Refs. [173–175]). This feature is particularly interesting, as it is the mechanism behind e.g. the emergence of non-trivial and rich phase diagrams in doped cuprates (see e.g. Ref. [176, 177]). Finally, if

[1] The SDW susceptibility and the structure factor are defined respectively by $\chi(q) = (1/N)\int_0^{1/T} \mathrm{d}\tau \sum_{i,j} \kappa_i(\tau)\kappa_j(0)$ and $S(q) = (1/N)\sum_{i,j} \mathrm{e}^{\mathrm{i}q(R_i - R_j)}\langle n_i n_j\rangle$, where $\kappa_i(t) = n_{i\uparrow}(t) - n_{i\downarrow}$ and $n_{i,\sigma} = \hat{c}^\dagger_{i,\sigma}\hat{c}_{i,\sigma}$.

in addition the electron density could be controlled when producing one of these states, it would provide the exciting possibility of turning the state of the electrons into a superconductor, as happens in the case of doping-induced superconductivity in cuprates [178]. The parameters calculated in this work apply to models where the dynamics of the electrons is restricted to one mode per site. In future works, it would be interesting to determine the conditions for this assumption to be valid, and whether these conditions can be engineered with current technology. Results in this direction would allow excitation schemes to be devised, and also the determination of the control available to tune the density of electrons in the lattice.

Acknowledgements

B.V. would like to thank A. Nunnenkamp and Prof. M. Child for helpful discussions at the beginning of this project. This work was supported by the EU through the STREP project OLAQUI, and by the University of Oxford through the Clarendon Fund (S.T.). B.V. acknowledges partial financial support from Merton College (Oxford, UK) through the Simms Bursary.

Appendix

6.A Replacement rules for the evaluation of two-centre molecular integrals with $m = 0$.

Here we outline the methods we have used to solve molecular integrals using symbolic replacements. We also provide all the necessary relations to implement the method for $m = 0$.

The first step towards the evaluation of these integrals is to express the Coulomb

potential in terms of a series of Legendre functions as

$$\frac{1}{r_{12}} = \sum_{k=0}^{\infty} \sum_{m=-k}^{k} \frac{(k-|m|)!}{(k+|m|)!} \frac{r(a)^k}{r(b)^{k+1}} \times P_k^{|m|}(\cos\theta_1) P_k^{|m|}(\cos\theta_2) \mathrm{e}^{\mathrm{i}m(\phi_1-\phi_2)}, \tag{6.16}$$

where r_{12} is the distance between two points with spherical coordinates (r_i, θ_i, ϕ_i), $P_k^{|m|}(x)$ are the associated Legendre functions [we use the notation $P_k^0(x) = P_k(x)$], and $r(a)$, $r(b)$ are the smaller and larger of the quantities r_1 and r_2; or using the von Neumann expansion

$$\frac{1}{r_{12}} = \frac{2}{R} \sum_{k=0}^{\infty} \sum_{m=-k}^{k} (-1)^m (2k+1) \left[\frac{(k-|m|)!}{(k+|m|)!}\right]^2 \times P_k^{|m|}[\lambda(a)] Q_k^{|m|}[\lambda(b)] P_k^{|m|}(\mu_1) P_k^{|m|}(\mu_2) \mathrm{e}^{\mathrm{i}m(\phi_1-\phi_2)}, \tag{6.17}$$

where in this case the two points are expressed in elliptical coordinates $(\lambda_i, \mu_i, \phi_i)$, $Q_k^{|m|}(x)$ are associated Legendre functions of the second kind, and $\lambda(a)$ is the lesser and $\lambda(b)$ the greater of λ_1 and λ_2 (see e.g. Ref. [140]).

Since the integral $\int_0^{2\pi} \mathrm{e}^{\mathrm{i}\nu\phi} \mathrm{d}\phi$ vanishes if ν is an integer different from zero, setting the quantum number $m = 0$ considerably simplifies the evaluation of the integrals (6.4) and (6.5) using the relations (6.16) and (6.17).

Every two-centre molecular integral apart from $W_{\mathbf{p},\mathbf{p}'}^{\mathbf{q},\mathbf{q}'}$ can be evaluated using Eq. (6.16). The angular part of these integrals will be non-zero for only a few terms; for instance, for $\mathbf{q} = \mathbf{q}' = (n, 0, 0)$, the angular part is non-zero for $k = 0$, and for $\mathbf{q} = \mathbf{q}' = (n, 1, 0)$ for $k = 0, 2$. It may be simplified by using the formula for the product of surface harmonics:

$$P_{\ell_1}(\cos\theta) P_{\ell_2}(\cos\theta) = \sum_{j=|\ell_1-\ell_2|}^{\ell_1+\ell_2} [C_j^{\ell_1,\ell_2}]^2 \, P_j(\cos\theta), \tag{6.18}$$

where $C_j^{\ell_1,\ell_2} = C(\ell_1, \ell_2, j; 0, 0, 0)$ are Clebsch-Gordan coefficients [164]. The integration of the radial part over the coordinates of the first electron necessitates the evaluation of integrals of the form

$$\int_0^\infty \mathrm{d}r_1\, r_1^2 \frac{r(a)^k}{r(b)^{k+1}} a_{\mathbf{q}}(r_1) a_{\mathbf{q}'}(r_1) = I^+_{\mathbf{q}\mathbf{q}',k}(r_2) + I^-_{\mathbf{q}\mathbf{q}',k}(r_2), \tag{6.19}$$

where $a_{\mathbf{q}}(r)$ is the radial part of the wavefunction (6.3), and r_i is the coordinate of the i^{th} electron. The functionals $I^{\pm}_{\mathbf{q}\mathbf{q}',k}(r_2)$ are defined as

$$I^-_{\mathbf{q}\mathbf{q}',k}(r_2) = (1/r_2^{k+1}) \int_0^{r_2} \mathrm{d}r_1\, r_1^2 r_1^k a_{\mathbf{q}}(r_1) a_{\mathbf{q}'}(r_1) \tag{6.20}$$

and

$$I^+_{\mathbf{q}\mathbf{q}',k}(r_2) = r_2^k \int_{r_2}^\infty \mathrm{d}r_1\, r_1^2 r_1^{-k-1} a_{\mathbf{q}}(r_1) a_{\mathbf{q}'}(r_1). \tag{6.21}$$

For $k = 0$ both (6.20) and (6.21) can be solved using the rules

$$\begin{aligned} \mathrm{R3}: \int_0^r \mathrm{d}r\, \mathrm{e}^{-ar} r^k &\rightarrow [k! - \Gamma_{k+1}(ar)]/a^{k+1} \\ \mathrm{R4}: \int_r^\infty \mathrm{d}r\, \mathrm{e}^{-ar} r^k &\rightarrow \Gamma_{k+1}(ar)/a^{k+1} \end{aligned} \tag{6.22}$$

If the sum of Eq. (6.16) contains only $k = 0$ terms, the symbolic form of the integral is obtained by replacing the spherical coordinates of the remaining electron by elliptical coordinates and using the replacement rules of Eqs. (6.22) and Table 6.1. In integrals requiring terms associated with $k > 0$ in the sum (6.16), the functionals associated with $k = 0$ dominate [167]. For higher values of k, the functional (6.21) can always be solved, and as an approximation we have dropped the terms in (6.20) that could not be solved analytically using the integration rules mentioned above.

Because it involves associated Legendre functions of the second kind, the evaluation of $W^{\mathbf{q},\mathbf{q}'}_{\mathbf{p},\mathbf{p}'}$ is more problematic. We used the Rodrigues formula to expand

these functions in terms of sums of Legendre polynomials and logarithms, and then solved the polynomial part by applying the replacement rules mentioned above. Solving the logarithmic part requires the integration over $\log(1 \pm x)$ for the first set of coordinates, and then exponential integral functions for the second set.

Chapter 7

Conclusion

In this thesis, we proposed three different ways of using superlattice setups to end the possibilities of manipulation and control of cold atoms trapped in optical ;ices. Here, we summarise the main results of this work, and discuss possible ensions that could be the subject of future research.

- In Chap. 3, we developed a model describing the dynamics of ultracold atoms in optical superlattices. We showed that starting from a half-filled lattice, dynamically halving the number of lattice sites using superlattice manipulations improves the initialisation time of a Mott-insulating state in which each site is occupied by a single atom. The work presented in this chapter could be extended in many directions, e.g. by considering the effects of the external trapping potential, two-dimensional setups, or developing more efficient ramping strategies. Starting with a different initial filling factor, superlattice manipulations could also be used to initialise a Mott-insulating state with two or three atoms per site, a useful configuration in the context of the creation of diatomic molecules. While increasing the initial filling factor would be computationally more challenging, we would not need to modify the theoretical framework. Also, starting with a system with e.g. a fractional filling factor, the same setup would allow the study of density-driven phase transitions, a

process that has been the subject of very little theoretical or experimental work.

- In Chap. 4, we presented a scheme aimed at manipulating quantum information encoded on the spin-states of ultracold atoms trapped in a superlattice potential. We showed that the utilisation of these setups allows the creation of arrays of double-well potentials each containing a Bell pair. This configuration can be used as an initial state to create either one-dimensional states with a tunable amount of entanglement, or as a resilient resource for one-way quantum computation. In this work, we assumed that it is possible to apply single-qubit unitary gates in parallel on every second site of the lattice, an operation that is not realisable with current technology. However, the current experimental effort towards its implementation makes us believe that it should become available shortly. The creation of a lattice with a Bell-pair in every double-well has been realised in an experiment [55], and so it is possible that simpler variants of the resource state presented in this chapter will be realised in the near future, as suggested in Ref. [32]. The most obvious extensions of the work presented in Chap. 4 should involve looking into different encodings of the qubits used in the resource state which would extend its resilience to other sources of external noise. We believe that the graphical notation devised by Gross and Eisert in Ref. [126] constitutes a powerful tool to explore the possibility of creating and exploiting a resource state for one-way quantum computation encoded in a fully decoherence-free subspace.

- In Chap. 6, we proposed a superlattice setup aimed at enhancing the formation of spatially large diatomic molecules. We developed a method making use of symbolical calculations to evaluate molecular integrals, and approximated the equilibrium distance and binding energy of diatomic molecules composed

of Rydberg atoms with overlapping charge-density distributions. The same methods were used to evaluate the interaction parameters between the electrons of highly-excited Rydberg atoms separated by distances comparable to typical optical lattice spacings. The formation of ultra-cold molecules with such large spatial dimensions has not yet been extensively studied, and thus the possible extensions of the work presented in this chapter are numerous. First of all, a better understanding of the energy structure of these molecules would be beneficial for the purpose of defining more precisely the experimental requirements necessary for their realisation. For this purpose, additional theoretical work aimed at simplifying the expression of the coulombic potential in the presence of a small overlap between the electronic charge distributions would be beneficial, as it should facilitate the evaluation of molecular integrals. Also, numerical simulations could be developed in order to devise strategies aiming to improve the formation rate of these molecules. Similar simulations would also be useful for investigating ways of realising a state of interacting Rydberg atoms, starting from ground-state atoms trapped in an optical lattice. To create artificial metals with tunable interaction parameters is an experimentally challenging proposal, but its implementation could potentially constitute a new approach to the quantum simulation of Fermi systems.

BIBLIOGRAPHY

[1] A. Hemmerich, M. Weidemüller, T. Esslinger, C. Zimmermann, and T. Hänsch. Trapping Atoms in a Dark Optical Lattice. *Phys. Rev. Lett.*, 75(1):37, July 1995.

[2] G. Grynberg, B. Lounis, P. Verkerk, J.-Y. Courtois, and C. Salomon. Quantized motion of cold cesium atoms in two- and three-dimensional optical potentials. *Phys. Rev. Lett.*, 70(15):2249, April 1993.

[3] Dieter Jaksch, C. Bruder, J.I. Cirac, C.W. Gardiner, and P. Zoller. Cold Bosonic Atoms in Optical Lattices. *Phys. Rev. Lett.*, 81:3108, 1998.

[4] Matthew P. A. Fisher, Peter B. Weichman, G. Grinstein, and Daniel S. Fisher. Boson localization and the superfluid-insulator transition. *Phys. Rev. B*, 40:546, 1989.

[5] M. Greiner, O. Mandel, T. Esslinger, T. W. Hänsch, and I. Bloch. Quantum phase transition from a superfluid to a Mott insulator in a gas of ultracold atoms. *Nature*, 415:39, 2002.

[6] Markus Greiner, Olaf Mandel, Theodor W. Hänsch, and Immanuel Bloch. Collapse and revival of the matter wave field of a Bose-Einstein condensate. *Nature*, 419:51, 2002.

[7] P. Rabl, A. J. Daley, P. O. Fedichev, J. I. Cirac, and P. Zoller. Defect-Suppressed Atomic Crystals in an Optical Lattice. *Phys. Rev. Lett.*, 91(11):110403, September 2003.

[8] T. Calarco, U. Dorner, P. S. Julienne, C. J. Williams, and Peter Zoller. Quantum computations with atoms in optical lattices: Marker qubits and molecular interactions. *Phys. Rev. A*, 70:012306, 2004.

[9] Chuanwei Zhang, S. L. Rolston, and S. Das Sarma. Manipulation of single neutral atoms in optical lattices. *Phys. Rev. A*, 74(4):042316, October 2006.

[10] Alastair Kay and Jiannis K. Pachos. Quantum computation in optical lattices via global laser addressing. *New J. Phys.*, 6:126, 2004.

[11] D. Jaksch, H.-J. Briegel, J. I. Cirac, C. W. Gardiner, and P. Zoller. Entanglement of Atoms via Cold Controlled Collisions. *Phys. Rev. Lett.*, 82:1975, 1999.

[12] Hans J. Briegel and Robert Raussendorf. Persistent Entanglement in Arrays of Interacting Particles. *Phys. Rev. Lett.*, 86:910, 2001.

[13] R. Raussendorf and H.-J. Briegel. A One-Way Quantum Computer. *Phys. Rev. Lett.*, 86:5188, 2001.

[14] Andrew M. Childs, Debbie W. Leung, and Michael A. Nielsen. Unified derivations of measurement-based schemes for quantum computation. *Phys. Rev. A*, 71(3):032318, March 2005.

[15] Olaf Mandel, Markus Greiner, Artur Widera, Tim Rom, Theodor W. Hänsch, and Immanuel Bloch. Controlled collisions for multi-particle entanglement of optically trapped atoms. *Nature*, 425(6961):937, October 2003.

[16] Olaf Mandel, Markus Greiner, Artur Widera, Tim Rom, Theodor W. Hänsch, and Immanuel Bloch. Coherent Transport of Neutral Atoms in Spin-Dependent Optical Lattice Potentials. *Phys. Rev. Lett.*, 91:010407, 2003.

[17] Jeremy M. Hutson and Pavel Soldan. Molecule formation in ultracold gases. *International Reviews in Physical Chemistry*, 25(4):497, 2006.

[18] Roman V. Krems. Molecules near absolute zero and external field control of atomic and molecular dynamics. *International Reviews in Physical Chemistry*, 24:99, 2005.

[19] Francoise Masnou-Seeuws and Pierre Pillet. Ultracold molecule. *Europhysics News*, 33(6):23, 2002.

[20] A. Micheli, G. Brennen, and P. Zoller. A toolbox for lattice-spin models with polar molecules. *Nature Phys.*, 2:341, 2006.

[21] Cindy A. Regal, Christopher Ticknor, John L. Bohn, and Deborah S. Jin. Creation of ultracold molecules from a Fermi gas of atoms. *Nature*, 424(6944):47, July 2003.

[22] C. Ryu, X. Du, Emek Yesilada, Artem M. Dudarev, Shoupu Wan, Qian Niu, and D. J. Heinzen. Raman-induced oscillation between an atomic and a molecular quantum gas. 2005. (Preprint:cond-mat/0508201).

[23] C. Ospelkaus, S. Ospelkaus, L. Humbert, P. Ernst, K. Sengstock, and K. Bongs. Ultracold Heteronuclear Molecules in a 3D Optical Lattice. *Phys. Rev. Lett.*, 97(12):120402, September 2006.

[24] Thilo Stöferle, Henning Moritz, Kenneth Gunter, Michael Köhl, and Tilman Esslinger. Molecules of Fermionic Atoms in an Optical Lattice. *Phys. Rev. Lett.*, 96(3):030401, January 2006.

[25] Chris H. Greene, A. S. Dickinson, and H. R. Sadeghpour. Creation of Polar and Nonpolar Ultra-Long-Range Rydberg Molecules. *Phys. Rev. Lett.*, 85(12):2458, September 2000.

[26] Chris H. Greene, Edward L. Hamilton, Heather Crowell, Cedomil Vadla, and Kay Niemax. Experimental Verification of Minima in Excited Long-Range Rydberg States of Rb_2. *Phys. Rev. Lett.*, 97(23):233002, December 2006.

[27] Christophe Boisseau, Ionel Simbotin, and Robin Côté. Macrodimers: Ultralong Range Rydberg Molecules. *Phys. Rev. Lett.*, 88(13):133004, March 2002.

[28] Alexander Klein and Dieter Jaksch. Simulating high-temperature superconductivity model Hamiltonians with atoms in optical lattices. *Phys. Rev. A*, 73(5):053613, May 2006.

[29] L.-M. Duan, E. Demler, and M. D. Lukin. Controlling Spin Exchange Interactions of Ultracold Atoms in Optical Lattices. *Phys. Rev. Lett.*, 91(9):090402, August 2003.

[30] Anders S. Sorensen, Eugene Demler, and Mikhail D. Lukin. Fractional Quantum Hall States of Atoms in Optical Lattices. *Phys. Rev. Lett.*, 94(8):086803, March 2005.

[31] R. N. Palmer and D. Jaksch. High-field fractional quantum Hall effect in optical lattices. *Phys Rev Lett*, 96(18):180407, May 2006.

[32] Immanuel Bloch. Quantum coherence and entanglement with ultracold atoms in optical lattices. *Nature*, 453(7198):1016, June 2008.

[33] Christopher J. Foot. *Atomic Physics.* Oxford University Press, Oxford, 2005.

[34] Isaac F. Silvera and J. T. M. Walraven. Stabilization of Atomic Hydrogen at Low Temperature. *Phys. Rev. Lett.*, 44(3):164, January 1980.

[35] M. H. Anderson, J. R. Ensher, M. R. Matthews, C. E. Wieman, and E. A. Cornell. Observation of Bose-Einstein Condensation in a Dilute Atomic Vapor. *Science*, 269(5221):198, July 1995.

[36] K. B. Davis, M. O. Mewes, M. R. Andrews, N. J. van Druten, D. S. Durfee, D. M. Kurn, and W. Ketterle. Bose-Einstein Condensation in a Gas of Sodium Atoms. *Phys. Rev. Lett.*, 75(22):3969, November 1995.

[37] C. J. Pethick and H. Smith. *Bose-Einstein Condensation in Dilute Gases.* Cambridge University Press, 2002.

[38] Claude Cohen-Tannoudji, Bernard Diu, and Franck Laloë. *Mécanique Quantique I + II.* Hermann, 1998.

[39] John R. Taylor. *Scattering theory.* Dover, 1972.

[40] Herman Feshbach. Unified theory of nuclear reactions. *Ann. Phys. (N.Y.)*, 5:357, 1958.

[41] P. A. Fraser and S. K. Burley. A simple model of a Feshbach resonance. *European Journal of Physics*, 3(4):230, 1982.

[42] Thorsten Kohler, Krzysztof Goral, and Paul S. Julienne. Production of cold molecules via magnetically tunable Feshbach resonances. *Reviews of Modern Physics*, 78(4):1311, 2006.

[43] S. Inouye, M. R. Andrews, J. Stenger, H.-J. Miesner, D. M. Stamper-Kurn, and W. Ketterle. Observation of Feshbach resonances in a Bose-Einstein condensate. *Nature*, 392(6672):151, March 1998.

[44] Stephen M. Barnett and Paul M. Radmore. *Methods in Theoretical Quantum Optics.* Oxford University Press, 1997.

[45] Christopher C. Gerry and Peter L. Knight. *Introductory quantum optics.* Cambridge University Press, 2005.

[46] Claude Cohen-Tannoudji, Jacques Dupont-Roc, and Gilbert Grynberg. *Atom-Photon Interactions: Basic Processes and Applications.* Wiley, 1998.

[47] Ana Maria Rey. *Ultra-cold bosonic atoms in optical lattices.* PhD thesis, Univ. of Maryland at College Park, 2004.

[48] D. Jaksch and P. Zoller. The cold atom Hubbard toolbox. *Annals of Physics*, 315:52, 2005.

[49] S. R. Clark. *Strongly correlated one-dimensional systems of cold atoms in optical lattices.* PhD thesis, University of Oxford, 2007.

[50] M. Roger, C. Bäuerle, and Yu M. Bunkov. Multiple-Spin Exchange on a Triangular Lattice: A Quantitative Interpretation of Thermodynamic Properties of Two-Dimensional Solid 3He. *Phys. Rev. Lett.*, 80:1308, 1997.

[51] Pulickel M. Ajayan and Boris I. Yakobson. Material science: Oxygen breaks into carbon world. *Nature*, 441(7095):818, June 2006.

[52] S. Trotzky, P. Cheinet, S. Folling, M. Feld, U. Schnorrberger, A. M. Rey, A. Polkovnikov, E. A. Demler, M. D. Lukin, and I. Bloch. Time-Resolved Observation and Control of Superexchange Interactions with Ultracold Atoms in Optical Lattices. *Science*, 319(5861):295, January 2008.

[53] S. Fölling, S. Trotzky, P. Cheinet, M. Feld, R. Saers, A. Widera, T. Muller, and I. Bloch. Direct observation of second-order atom tunnelling. *Nature*, 448(7157):1029, August 2007.

[54] J. Sebby-Strabley, M. Anderlini, P. S. Jessen, and J. V. Porto. Lattice of double wells for manipulating pairs of cold atoms. *Phys. Rev. A*, 73:033605, 2006.

[55] Marco Anderlini, Patricia J. Lee, Benjamin L. Brown, Jennifer Sebby-Strabley, William D. Phillips, and J. V. Porto. Controlled exchange interaction between pairs of neutral atoms in an optical lattice. *Nature*, 448(7152):452, July 2007.

[56] P. J. Lee, M. Anderlini, B. L. Brown, J. Sebby-Strabley, W. D. Phillips, and J. V. Porto. Sublattice Addressing and Spin-Dependent Motion of Atoms in a Double-Well Lattice. *Physical Review Letters*, 99(2):020402, 2007.

[57] N. W. Ashcroft and N. D. Mermin. *Solid State Physics.* Brooks/Cole Thomson Learning, Philadelphia, 1976.

[58] Gerald Burns. *Solid state physics.* Academic Press, 1985.

[59] I. Schnell, G. Czycholl, and R. C. Albers. Hubbard-U calculations for Cu from first-principle Wannier functions. *Phys. Rev. B*, 65:075103, 2002.

[60] E. Toth, A. M. Rey, and P. B. Blakie. Theory of correlations between ultracold bosons released from an optical lattice. 2008. (Preprint: arXiv:08032922).

[61] W. Zwerger. Mott-Hubbard transition of cold atoms in optical lattices. *Journal of Optics B: Quantum and Semiclassical Optics*, 5:S9, 2003.

[62] V. A. Kashurnikov, N. V. Prokofev, and B. V. Svistunov. Revealing the superfluid to Mott-insulator transition in an optical lattice. *Phys. Rev. A*, 66(3):031601, September 2002.

[63] W. Kohn. Analytic Properties of Bloch Waves and Wannier Functions. *Phys. Rev.*, 115(4):809, 1959.

[64] Jacques Des Cloizeaux. Analytical Properties of n-Dimensional Energy Bands and Wannier Functions. *Phys. Rev.*, 135:A698, 1964.

[65] E. I. Blount. *Solid state physics: advances in research and applications*, chapter Formalisms of Band Theory, page 305. Academic Press, 1962.

[66] Nicola Marzari and David Vanderbilt. Maximally Localised generalised Wannier functions for composite energy bands. *Phys. Rev. B*, 56(20):12847, November 1997.

[67] Stephan Goedecker. Linear scaling electronic structure methods. *Rev. Mod. Phys.*, 71(4):1085, 1999.

[68] G. Nenciu. Existence of the exponentially localised Wannier functions. *Communications in Mathematical Physics*, 91(1):81, March 1983.

[69] Lixin He and David Vanderbilt. Exponential Decay of Wannier Functions and Related Quantities. *Phys. Rev. Lett.*, 86:5341, 2001.

[70] Christian Brouder, Gianluca Panati, Matteo Calandra, Christophe Mourougane, and Nicola Marzari. Exponential Localization of Wannier Functions in Insulators. *Phys. Rev. Lett.*, 98(4):046402, January 2007.

[71] Helmut Bross. A General Interpolation Scheme for the One-Electron Energies of a Solid. *Z. Physik*, 243:311, 1971.

[72] D. M. Whittaker and M. P. Croucher. Maximally localised Wannier functions for photonic lattices. *Phys. Rev. B*, 67:085204, 2003.

[73] Maciej Lewenstein, Anna Sanpera, Veronica Ahufinger, Bogdan Damski, Aditi Sen De, and Ujjwal Sen. Ultracold atomic gases in optical lattices: Mimicking condensed matter physics and beyond. *(Preprint cond-mat/0606771)*, 2006.

[74] J. I. Cirac and P. Zoller. New frontiers in quantum information with atoms and ions. *Physics Today*, 57(3):38, March 2004.

[75] K. G. H. Vollbrecht, E. Solano, and J. I. Cirac. Ensemble Quantum Computation with Atoms in Periodic Potentials. *Phys. Rev. Lett.*, 93(22):220502, November 2004.

[76] Zheng-Wei Zhou, Yong-Jian Han, and Guang-Can Guo. Local operations in qubit arrays via global periodic manipulation. *Phys. Rev. A*, 74(5):052334, November 2006.

[77] H. Haffner, W. Hansel, C. F. Roos, J. Benhelm, D. Chek-al kar, M. Chwalla, T. Korber, U. D. Rapol, M. Riebe, P. O. Schmidt, C. Becher, O. Guhne, W. Dur, and R. Blatt. Scalable multiparticle entanglement of trapped ions. *Nature*, 438(7068):643, December 2005.

[78] P. S. Julienne, C. J. Williams, Y. B. Band, and Marek Trippenbach. Loading Bose-Einstein-condensed atoms into the ground state of an optical lattice. *Phys. Rev. A*, 72(5):053615, November 2005.

[79] Shlomo E. Sklarz, Inbal Friedler, David J. Tannor, Yehuda B. Band, and Carl J. Williams. Flat-phase loading of a Bose-Einstein condensate into an optical lattice. *Phys. Rev. A*, 66(5):053620, November 2002.

[80] S. R. Clark and Dieter Jaksch. Dynamics of the superfluid to Mott-insulator transition in one dimension. *Phys. Rev. A*, 70:43612, 2004.

[81] P. B. Blakie and J. V. Porto. Adiabatic loading into optical lattices. *Phys. Rev. A*, 69:013603, 2004.

[82] S. Peil, J. V. Porto, B. Laburthe Tolra, J. M. Obrecht, B. E. King, M. Sub-

botin, S. L. Rolston, and W. D. Phillips. Patterned loading of a Bose-Einstein condensate into an optical lattice. *Phys. Rev. A*, 67(5):051603, May 2003.

[83] Olivier Gygi, Helmut G. Katzgraber, Matthias Troyer, Stefan Wessel, and G. George Batrouni. Simulations of ultracold bosonic atoms in optical lattices with anharmonic traps. *Phys. Rev. A*, 73(6):063606, 2006.

[84] T. P. Meyrath, F. Schreck, J. L. Hanssen, C.-S. Chuu, and M. G. Raizen. Bose-Einstein condensate in a box. *Phys. Rev. A*, 71(4):041604, 2005.

[85] Till D. Kühner, Steven R. White, and H. Monien. One-dimensional Bose-Hubbard model with nearest-neighbor interaction. *Phys. Rev. B*, 61:12474, 2000.

[86] Robert Roth and Keith Burnett. Phase diagram of bosonic atoms in two-color superlattices. *Phys. Rev. A*, 68:023604, 2003.

[87] Belen Paredes, Artur Widera, Valentin Murg, Olaf Mandel, Simon Fölling, Ignacio Cirac, Gora V. Shlyapnikov, Theodor W. Hansch, and Immanuel Bloch. Tonks-Girardeau gas of ultracold atoms in an optical lattice. *Nature*, 429(6989):277, May 2004.

[88] L. I. Schiff. *Quantum Mechanics.* Mc-Graw-Hill, 3nd edition, 1968.

[89] S. R. Clark and D. Jaksch. Signature of the superfluid to MI-insulator transition in the excitation spectrum of cold atoms. *New J. Phys.*, 8:160, 2006.

[90] J. Hecker Denschlag, J. E. Simsarian, H. Haeffner, C. McKenzie, A. Browaeys, D. Cho, K. Helmerson, S. L. Rolston, and W. D. Phillips. A Bose-Einstein condensate in an optical lattice. *J. Phys. B: At. Mol. Opt. Phys.*, 35:3095, 2002.

[91] A. Griessner, A. J. Daley, S. R. Clark, D. Jaksch, and P. Zoller. Dissipative dynamics of atomic Hubbard models coupled to a phonon bath: dark state cooling of atoms within a Bloch band of an optical lattice. *New Journal of Physics*, 9(2):44, 2007.

[92] Tino Weber, Jens Herbig, Michael Mark, Hanns-Christoph Nagerl, and Rudolf Grimm. Bose-Einstein Condensation of Cesium. *Science*, 299(5604):232, 2003.

[93] Bogdan Damski. The Simplest Quantum Model Supporting the Kibble-Zurek Mechanism of Topological Defect Production: Landau-Zener Transitions from a New Perspective. *Phys. Rev. Lett.*, 95:035701, 2005.

[94] Bogdan Damski and Wojciech H. Zurek. Adiabatic-Impulse approximation for avoided level crossings: from phase transition dynamics to Landau-Zener evolutions and back again. *Phys. Rev. A*, 73:063405, 2006.

[95] Fernando M. Cucchietti, Bogdan Damski, Jacek Dziarmaga, and Wojciech H. Zurek. Dynamics of the Bose-Hubbard model: transition from Mott insulator to superfluid. *Phys. Rev. A*, 75:023603, 2007.

[96] W. H. Zurek. Cosmological experiments in superfluid helium. *Nature*, 317:505, 1985.

[97] C. Zener. Non-Adiabatic Crossing of Energy Levels. *Proc. Roy. Soc. London Ser. A*, 137:696, 1932.

[98] Nikolai Sinitsyn. *Generalisation of the Landau-Zener theory in the physics of nanoscale systems.* PhD thesis, Texas A&M University, 2004.

[99] Jan R. Rubbmark, Michael M. Kash, Michael G. Littman, and Daniel Kleppner. Dynamical effects at avoided level crossings: A study of the Landau-Zener effect using Rydberg atoms. *Phys. Rev. A*, 23:3107, 1981.

[100] B. Sporkmann and H. Bross. Calculation of Wannier functions for fcc transition metals by Fourier transformation of Bloch functions. *Phys. Rev. B*, 49:10869, 1994.

[101] Guifré Vidal. Efficient Classical Simulation of Slightly Entangled Quantum Computations. *Phys. Rev. Lett.*, 91:147902, October 2003.

[102] Guifré Vidal. Efficient Simulation of One-Dimensional Quantum Many-Body Systems. *Phys. Rev. Lett.*, 93:40502, July 2004.

[103] G. Vidal. Classical Simulation of Infinite-Size Quantum Lattice Systems in One Spatial Dimension. *Physical Review Letters*, 98(7):070201, 2007.

[104] A. J. Daley, C. Kollath, U. Schollwöck, and G. Vidal. Time-dependent density-matrix renormalization-group using adaptive effective Hilbert spaces. *Journal of Statistical Mechanics: Theory and Experiment*, 2004(04):P04005, 2004.

[105] Fabrice Gerbier, Artur Widera, Simon Fölling, Olaf Mandel, and Immanuel Bloch. Resonant control of spin dynamics in ultracold quantum gases by microwave dressing. *Phys. Rev. A*, 73(4):041602, April 2006.

[106] Artur Widera, Fabrice Gerbier, Simon Fölling, Tatjana Gericke, Olaf Mandel, and Immanuel Bloch. Precision measurement of spin-dependent interaction strengths for spin-1 and spin-2 Rb atoms. *New Journal of Physics*, 8(8):152, 2006.

[107] H. Pu and P. Meystre. Creating Macroscopic Atomic Einstein-Podolsky-Rosen States from Bose-Einstein Condensates. *Phys. Rev. Lett.*, 85(19):3987, November 2000.

[108] L.-M. Duan, A. Sørensen, J. I. Cirac, and P. Zoller. Squeezing and Entanglement of Atomic Beams. *Phys. Rev. Lett.*, 85(19):3991, November 2000.

[109] A. M. Rey, V. Gritsev, I. Bloch, E. Demler, and M. D. Lukin. Preparation and Detection of Magnetic Quantum Phases in Optical Superlattices. *Phys. Rev. Lett.*, 99(14):140601, October 2007.

[110] Tin-Lun Ho. Spinor Bose Condensates in Optical Traps. *Phys. Rev. Lett.*, 81(4):742, July 1998.

[111] Artur Widera, Fabrice Gerbier, Simon Fölling, Tatjana Gericke, Olaf Mandel, and Immanuel Bloch. Coherent Collisional Spin Dynamics in Optical Lattices. *Phys. Rev. Lett.*, 95(19):190405, November 2005.

[112] G. J. Milburn, J. Corney, E. M. Wright, and D. F. Walls. Quantum dynamics of an atomic Bose-Einstein condensate in a double-well potential. *Phys. Rev. A*, 55(6):4318, June 1997.

[113] C. Menotti, J. R. Anglin, J. I. Cirac, and P. Zoller. Dynamic splitting of a Bose-Einstein condensate. *Phys. Rev. A*, 63(2):023601, January 2001.

[114] D. Jaksch, S. A. Gardiner, K. Schulze, J. I. Cirac, and P. Zoller. Uniting Bose-Einstein Condensates in Optical Resonators. *Phys. Rev. Lett.*, 86(21):4733, May 2001.

[115] R. Raussendorf and H. Briegel. Computational model underlying the one-way quantum computer. *Quant. Inf. Comp.*, 6:433, 2002.

[116] M. S. Tame, M. Paternostro, and M. S. Kim. One-way quantum computing in a decoherence-free subspace. *New Journal of Physics*, 9(6):201, 2007.

[117] Masahito Ueda and Masato Koashi. Theory of spin-2 Bose-Einstein condensates: Spin correlations, magnetic response, and excitation spectra. *Phys. Rev. A*, 65(6):063602, May 2002.

[118] Wenxian Zhang, Su Yi, and L. You. Bose-Einstein condensation of trapped interacting spin-1 atoms. *Phys. Rev. A*, 70(4):043611, October 2004.

[119] B. Vaucher, S. R. Clark, U. Dorner, and D. Jaksch. Fast initialization of a high-fidelity quantum register using optical superlattices. *New Journal of Physics*, 9(7):221, 2007.

[120] N. Teichmann and C. Weiss. Coherently controlled entanglement generation in a binary Bose-Einstein condensate. *Europhysics Letters (EPL)*, 78(1):10009, 2007.

[121] Michael A. Nielsen and Isaac L. Chuang. *Quantum Computation and Quantum Information.* Cambridge University Press, 2000.

[122] David Hayes, Paul S. Julienne, and Ivan H. Deutsch. Quantum Logic via the Exchange Blockade in Ultracold Collisions. *Physical Review Letters*, 98(7):070501, 2007.

[123] Jiannis K. Pachos and Peter L. Knight. Quantum Computation with a One-Dimensional Optical Lattice. *Phys. Rev. Lett.*, 91(10):107902, September 2003.

[124] Jens Eisert and Hans J. Briegel. Schmidt measure as a tool for quantifying multiparticle entanglement. *Phys. Rev. A*, 64(2):022306, July 2001.

[125] S. F. Huelga, C. Macchiavello, T. Pellizzari, A. K. Ekert, M. B. Plenio, and J. I. Cirac. Improvement of Frequency Standards with Quantum Entanglement. *Phys. Rev. Lett.*, 79:3865, 1997.

[126] D. Gross and J. Eisert. Novel Schemes for Measurement-Based Quantum Computation. *Phys. Rev. Lett.*, 98(22):220503–4, June 2007.

[127] D. Gross, J. Eisert, N. Schuch, and D. Perez-Garcia. Measurement-based quantum computation beyond the one-way model. *(pre-print: quant-ph/0706.3401)*, 2007.

[128] H. Pu, C. K. Law, S. Raghavan, J. H. Eberly, and N. P. Bigelow. Spin-mixing dynamics of a spinor Bose-Einstein condensate. *Phys. Rev. A*, 60(2):1463, August 1999.

[129] D.M. Stamper-Kurn and W. Ketterle. *Course 2: Spinor Condensates and Light Scattering from Bose-Einstein Condensates*, volume 72/2001 of *Les Houches*. Springer Berlin / Heidelberg, 2001.

[130] Nicholas Bigelow. Bose-Einstein condensates: Spins mixed up. *Nat Phys*, 1(2):89, November 2005.

[131] G. Thalhammer and K. Winkler. Long-lived Feshbach molecules in a three-dimensional optical lattice. *Phys Rev Lett*, 96:050402, 2006.

[132] K. Winkler, F. Lang, G. Thalhammer, P. v. d. Straten, R. Grimm, and J. Hecker Denschlag. Coherent Optical Transfer of Feshbach Molecules to a Lower Vibrational State. *Phys. Rev. Lett.*, 98(4):043201, January 2007.

[133] T. Volz, N. Syassen, D. M. Bauer, E. Hansis, S. Durr, and G. Rempe. Preparation of a quantum state with one molecule at each site of an optical lattice. *Nat Phys*, 2(10):692, October 2006.

[134] Tim Rom, Thorsten Best, Olaf Mandel, Artur Widera, Markus Greiner, Theodor W. Hänsch, and Immanuel Bloch. State Selective Production of Molecules in Optical Lattices. *Phys. Rev. Lett.*, 93(7):073002, August 2004.

[135] E. L. Hamilton, C. H. Greene, and H. R. Sadeghpour. Shape-resonance in-

duced long-range molecular Rydberg states. *J. Phys. B: At. Mol. Opt. Phys.*, 35:L199, 2002.

[136] S. M. Farooqi, D. Tong, S. Krishnan, J. Stanojevic, Y. P. Zhang, J. R. Ensher, A. S. Estrin, C. Boisseau, R. Ct, E. E. Eyler, and P. L. Gould. Long-Range Molecular Resonances in a Cold Rydberg Gas. *Phys. Rev. Lett.*, 91(18):183002, October 2003.

[137] J. Stanojevic, R. Ct, D. Tong, S.M. Farooqi, E.E. Eyler, and P.L. Gould. Long-range Rydberg-Rydberg interactions and molecular resonances. *Eur. Phys. J. D*, 40(3):3, 2006.

[138] Axel Grabowski, Rolf Heidemann, Robert Löw, Jrgen Stuhler, , and Tilman Pfau. High Resolution Rydberg Spectroscopy of ultracold Rubidium Atoms. *Fortschr. Phys.*, 54:765, 2006.

[139] Peter W. Atkins and Ronald S. Friedman. *Molecular quantum mechanics.* Oxford University Press, Oxford, 2005.

[140] John C. Slater. *Quantum theory of Molecules and Solids*, volume 1. Mc-Graw-Hill, New-York, 1974.

[141] Robert J. Buehler and Joseph O. Hirschfelder. Bipolar Expansion of Coulombic Potentials. *Phys. Rev.*, 83(3):628, August 1951.

[142] M. R. Flannery, D. Vinceanu, and V. N. Ostrovsky. Long-range interactions between polar Rydberg atoms. *J. Phys. B: At. Mol. Opt. Phys.*, 38:s279, 2005.

[143] Bing Ji, Chin-Chun Tsai, and W. C. Stwalley. Proposed modification of the criterion for the region of validity of the inverse-power expansion in diatomic long-range potentials. *Chem. Phys. Lett.*, 236:242, 1995.

[144] Peter R. Fontana. Theory of Long-Range Interatomic Forces. II. First-Order Interaction Energies in the Uncoupled Representation. *Phys. Rev.*, 123(5):1871, September 1961.

[145] M. Marinescu. Dispersion coefficients for the nP-nP asymptote of homonuclear alkali-metal dimers. *Phys. Rev. A*, 56(6):4764, December 1997.

[146] M. Marinescu and A. Dalgarno. Dispersion forces and long-range electronic transition dipole moments of alkali-metal dimer excited states. *Phys. Rev. A*, 52(1):311, July 1995.

[147] Michael P. Barnett. Molecular integrals and information processing. *International Journal of Quantum Chemistry*, 95(6):791, 2003.

[148] J. Fernández Rico, R. López, G. Ramírez, and C. Tablero. Exchange integrals: Comparison of numerical and analytical procedures. *Phys. Rev. A*, 49(5):3381, May 1994.

[149] B. Knuffman and G. Raithel. Multipole transitions of Rydberg atoms in modulated ponderomotive potentials. *Phys. Rev. A*, 75(5):053401, May 2007.

[150] D. DeMille. Quantum Computation with Trapped Polar Molecules. *Phys. Rev. Lett.*, 88(6):067901, January 2002.

[151] A. A. Khuskivadze, M. I. Chibisov, and I. I. Fabrikant. Adiabatic energy levels and electric dipole moments of Rydberg states of Rb2 and Cs2 dimers. *Phys. Rev. A*, 66(4):042709, October 2002.

[152] J. Stanojevic, R. Côté, D. Tong, E.E. Eyler, and P.L. Gould. Long-range potentials and (n-1)d+ns molecular resonances in an ultracold rydberg gas.

[153] Tatjana Gericke, Peter Wurtz, Daniel Reitz, Tim Langen, and Herwig Ott. High Resolution Imaging of Single Atoms in a Quantum Gas. 2008. (Preprint: arXiv:0804.4788).

[154] K. I. Petsas, A. B. Coates, and G. Grynberg. Crystallography of optical lattices. *Phys. Rev. A*, 50(6):5173, Dec 1994.

[155] Saers, R. , Rehn, M. , Scheler, T. , Zelán, M. , and Kastberg, A. . A set-up for flexible geometry optical lattices. *The European Physical Journal Applied Physics*, 42(3):269, jun 2008.

[156] Michael Köhl and Tilman Esslinger. Fermionic atoms in optical lattices: a new synthetic material. *Europhysics News*, 37(2):18, 2006.

[157] Z. Idziaszek, L. Santos, and M. Lewenstein. Laser cooling of trapped Fermi gases far below the Fermi temperature. *Phys. Rev. A*, 64(5):051402, October 2001.

[158] T. Cubel, B. K. Teo, V. S. Malinovsky, J. R. Guest, A. Reinhard, B. Knuffman, P. R. Berman, and G. Raithel. Coherent population transfer of ground-state atoms into Rydberg states. *Phys. Rev. A*, 72(2):023405, August 2005.

[159] C. A. Coulson. *Valence.* Oxford University Press, Oxford, 1952.

[160] Wenhui Li, I. Mourachko, M. W. Noel, and T. F. Gallagher. Millimeter-wave spectroscopy of cold Rb Rydberg atoms in a magneto-optical trap: Quantum defects of the ns, np, and nd series. *Phys. Rev. A*, 67(5):052502, May 2003.

[161] A. V. Stolyarov and M. S. Child. Radiative properties of diatomic Rydberg states in quantum defect theory. Application to the hydrogen molecule. *Journal of Physics B: Atomic, Molecular and Optical Physics*, 32(2):527, 1999.

[162] B. G. Wilson, C. Iglesias, and F. Rogers. Near-threshold photoabsorption cross sections for nonhydrogenic ions. *Phys. Rev. A*, 38(9):4633, November 1988.

[163] Michael P. Barnett. Mathscape and molecular integrals. *Journal of Symbolic Computation*, 42(3):265, March 2007.

[164] Michael P. Barnett. Two-center nonexchange integrals over Slater orbitals. *J. Chem. Phys.*, 113(21):9419, December 2000.

[165] Thomas F. Gallagher. *Rydberg atoms.* Cambridge University Press, Cambridge, 1994.

[166] Michael Köhn and Tilman Esslinger. Fermionic atoms in an optical lattice: a new synthetic material. *Europhysics News*, 37:18, 2005.

[167] J. Appel, M. Grodzicki, and F. Paulsen. Bond-charge repulsion and hole superconductivity in the atomic representation of the CuO_2 plane. *Phys. Rev. B*, 47(5):2812, February 1993.

[168] Anna Painelli and Alberto Girlando. Electron correlations in one dimension: The Hubbard model. *Phys. Rev. B*, 39(4):2830, February 1989.

[169] F. Marsiglio and J. E. Hirsch. Hole superconductivity and the high-T_c oxides. *Phys. Rev. B*, 41(10):6435, April 1990.

[170] J. Tinka Gammel and David K. Campbell. Comment on the Missing Bond-Charge Repulsion in the Extended Hubbard Model. *Phys. Rev. Lett.*, 60(1):71, January 1988.

[171] Dionys Baeriswyl, Peter Horsch, and Kazumi Maki. Missing Bond-Charge Repulsion. *Phys. Rev. Lett.*, 60(1):70, January 1988.

[172] Ana Maria Rey, P. Blair Blakie, Guido Pupillo, Carl J. Williams, and Charles W. Clark. Bragg spectroscopy of ultracold atoms loaded in an optical lattice. *Phys. Rev. A*, 72:023407, 2005.

[173] Efthimios Kaxiras. *Atomic and electronic structure of solids.* Cambridge University Press, 2002.

[174] I. S. Elfimov, S. Yunoki, and G. A. Sawatzky. Possible Path to a New Class of Ferromagnetic and Half-Metallic Ferromagnetic Materials. *Phys. Rev. Lett.*, 89(21):216403, November 2002.

[175] J. E. Hirsch. Electron- and hole-hopping amplitudes in a diatomic molecule. III. p orbitals. *Phys. Rev. B*, 48(13):9815, October 1993.

[176] Daniel Duffy and Adriana Moreo. Influence of next-nearest-neighbor electron hopping on the static and dynamical properties of the two-dimensional Hubbard model. *Phys. Rev. B*, 52(21):15607, December 1995.

[177] M. Raczkowski, R. Frésard, and A. M. Oles. Interplay between incommensurate phases in the cuprates. *Europhysics Letters*, 76(1):128, 2006.

[178] Subir Sachdev and Shou-Cheng Zhang. Tuning Order in Cuprate Superconductors. *Science*, 295:452, 2002.